Spinning tops

A search for new physics in t-channel single top quark production with the ATLAS detector at the LHC

Degens, J.J.H.S.

Publication date
2024

Document Version
Final published version

Spinning Tops

A search for new physics in t-channel single top quark production with the ATLAS detector at the LHC

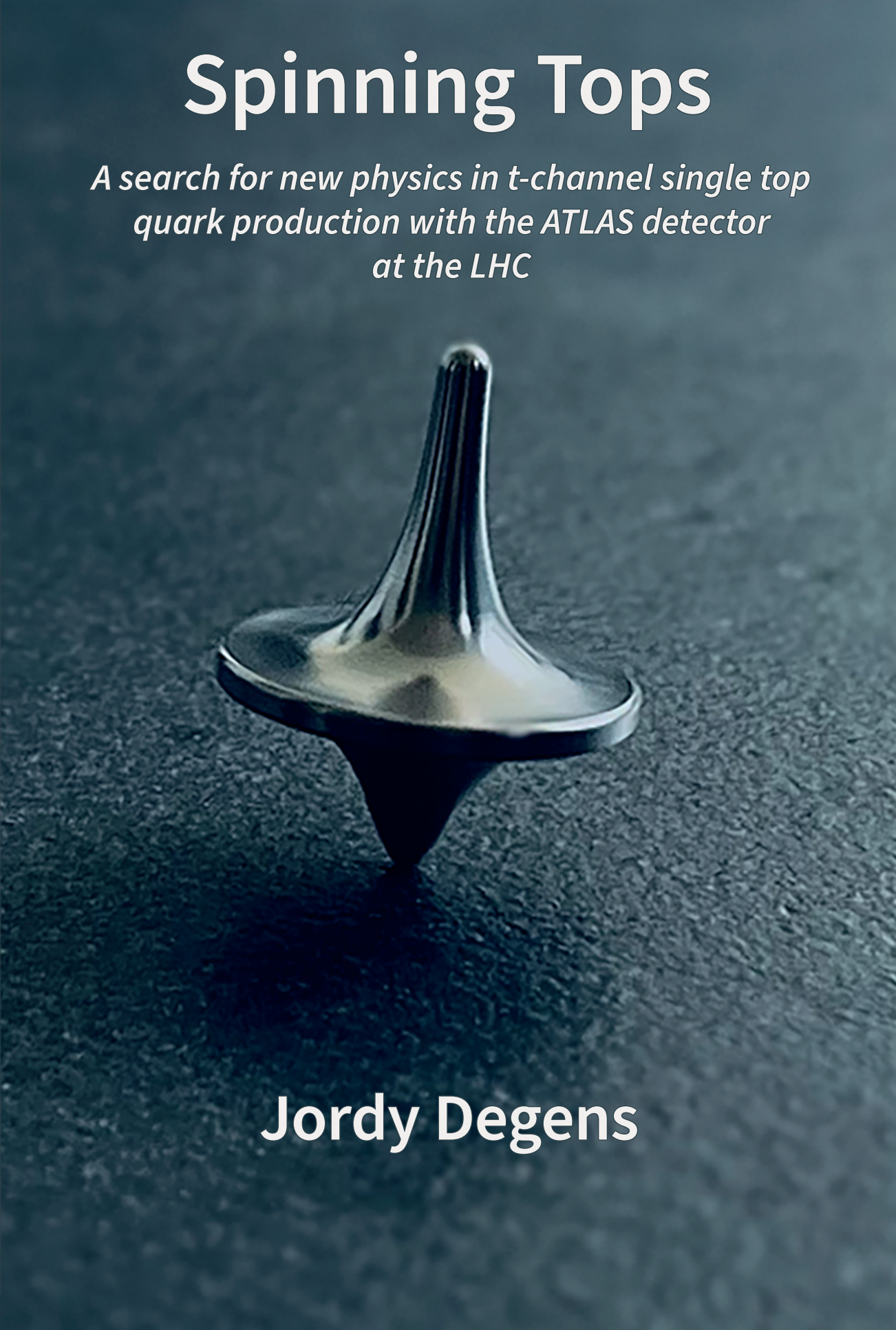

Jordy Degens

Spinning tops

A search for new physics in t-channel single top quark production
with the ATLAS detector at the LHC

Jordy Degens

ISBN: 978-94-6496-184-3

Thesis, Universiteit van Amsterdam (UvA), Amsterdam

Printed in the Netherlands by Gildeprint

This work originates as part of the research programme of the Foundation for Fundamental Research on Matter (FOM), and falls as of April 1, 2017 under the responsibility of Foundation for Nederlandse Wetenschappelijk Onderzoek Instituten (NWO-I), which is part of the Dutch Research Council (NWO). The work has been performed at the National Institute for Subatomic Physics (Nikhef).

Spinning tops

A search for new physics in t-channel single top quark production with the ATLAS detector at the LHC

ACADEMISCH PROEFSCHRIFT

ter verkrijging van de graad van doctor

aan de Universiteit van Amsterdam

op gezag van de Rector Magnificus

prof. dr. ir. P.P.C.C. Verbeek

ten overstaan van een door het College voor Promoties ingestelde commissie,

in het openbaar te verdedigen in de Agnietenkapel

op woensdag 18 september 2024, te 13.00 uur

door Jordy Jozef Hubert Simon Degens

geboren te Heerlen

Promotiecommissie

Promotores:	prof. dr. M. Vreeswijk	Universiteit van Amsterdam
	prof. dr. E.L.M.P. Laenen	Universiteit van Amsterdam
Overige leden:	dr. C.J.M. Nellist	Universiteit van Amsterdam
	prof. dr. P. Ferrari	Radboud Universiteit Nijmegen
	prof. dr. J. Boudreau	University of Pittsburgh
	prof. dr. W. Verkerke	Universiteit van Amsterdam
	prof. dr. ir. P.J. de Jong	Universiteit van Amsterdam
	dr. J. de Vries	Universiteit van Amsterdam

Faculteit der Natuurwetenschappen, Wiskunde en Informatica

Contents

Chapter 1

Introduction

To understand the smallest building blocks of our universe and how they interact with one another is the field of study of particle physics. So-far this has led to the Standard Model (SM), which provides a common framework to describe all known fundamental particles. In the SM, fermions constitute all the visible matter in the universe. Interactions are governed through four fundamental bosons. Electromagnetic interactions are described by the exchange of photons, strong interactions by the exchange of gluons and weak interactions are mediated via the Z and W-boson. The masses of fundamental particles are explained by the Higgs mechanism. The gravitational interactions do not play a significant role at the microscopic scale in reach of present experiments and are not included in the SM.

The SM is mathematically based on a gauge theory that makes accurate predictions of the behaviour of fundamental particles and their interactions. These have been confirmed by numerous experiments, with one of the prominent recent highlights the observation of the Higgs boson. However, it can not describe all experimental observations. The existence of dark matter and the observed matter-antimatter asymmetry are for example unexplained. This suggests that the SM is an approximation of a more fundamental theory of nature. Finding a theory that is able to explain all observations is the ultimate goal of fundamental particle physics.

The search for evidence of this theory is conducted in two complimentary approaches. Firstly by searching for new unobserved particles in experiments. These searches are commonly performed at high-energies and is called the direct approach. The alternative is the so-called indirect approach, which is followed in this thesis. By very precisely measuring the nature of already observed interactions, new phenomena can be indirectly measured. This is due to the quantum nature of the universe, where unknown high mass force-particles can lead to subtle deviations to processes at a lower energy scale in reach of current experiments. The possible deviations are described by an effective field theory (EFT), where the SM is systematically expanded by higher order interaction terms. This framework, referred to as SMEFT, allows to make quantitative predictions for observable interactions, without knowing the exact nature of the new physics.

The LHC collider is the most powerful collider to search for these potential new physics interactions at the writing of this thesis. The high centre-of-mass energy of $\sqrt{s} = 13\,\text{TeV}$ opens a gateway to the hunt for new physics. This thesis searches for new interactions in interactions of top quarks using the data collected by the ATLAS experiment at Run 2, corresponding to $140\,\text{fb}^{-1}$.

The top quark, observed at the Tevatron collider in 1995, is now abundantly produced at the LHC allowing for a precise measurement of the top quarks properties. The high mass of the top quark enhances the sensitivity to physics at higher energy scales. It also endows the top quark with an unique feature: the top quark decays before it hadronises, allowing to study the spin properties of a naked quark. The spin structure of the SM processes may be modified by new physics interactions, which could explain the observed matter- antimatter asymmetry in the universe. In this thesis, the spin structure is measured by analysing the angular correlations between the top decay products and tested against the predictions of SMEFT.

Thesis structure and personal contributions

The research presented in this thesis is conducted within the ATLAS collaboration using the Run 2 data set. The thesis follows the following structure.

Chapter 2 introduces the SM, the basics of top quark physics and the production of t-channel single top production. EFTs are introduced to parameterise deviations to the SM, followed by the phenomenology of proton-proton collisions.

Chapter 3 describes the LHC and the ATLAS detector during the Run 2 data taking period. It also briefly touches upon future upgrades to the ATLAS detector, where I worked on the ATLAS alignment studies of the Muon Spectrometer for Run 3. I did the first checks on the quality of the alignment using data during special runs of the ATLAS detector where the ATLAS toroidal field is off. Furthermore, I tested the in-plane alignment of the sBIS chambers which will be installed for the HL-LHC.

Chapter 4 describes the algorithms used in ATLAS for the identification of different particles. It also introduces a kinematic likelihood method, which I adapted to identify and reconstruct t-channel single top events.

Chapter 5 discusses the design of the analysis to measure EFT coefficients in the t-channel single top production. It covers the signal selection and categorisation. The definition of the final observable is explained, and the parameterisation in terms of EFT coefficients is presented. A novelty here is that the t-channel single top production process as well as one of the main backgrounds, the $t\bar{t}$ production process, is parameterised as a function of EFT coefficients. I was the main contributor to all these steps.

Chapter 6 presents my analysis of the data, which results in a measurement of the relevant EFT coefficients. It introduces the statistical methods to measure the EFT coefficients. It explains the treatment of systematic uncertainties and how this affects the final measurement.

Chapter 7 discusses potential improvements and future studies on the measurement of EFT coefficients. It introduces an alternative method using a decomposition of the angular decay spectrum in so-called M-Functions. Here I was involved in the development of the statistical framework and the optimisation of the signal selection.

Chapter 8 concludes this thesis.

Chapter 2

Theoretical foundations

This chapter introduces the theoretical foundations for this work. In sector 2.1 a brief introduction to the Standard Model (SM) of particle physics is given, with a focus on top quark physics in section 2.2. After that, in section 2.3, effective field theories are discussed as a model independent way to search for extensions of the Standard Model. Finally, we discuss how predictions of particle collisions are made, in section 2.4.

2.1 The Standard Model

2.1.1 Matter and forces

The SM of particle physics is the most precise theory that describes all known elementary particles and the interactions among them. The predictions of the SM have been verified with great precision by many experiments, conducted at facilities such as KEK (Japan), DESY (Germany), Fermilab (US), SLAC (US) and CERN (Switzerland). The SM is briefly described in this section, with a focus on electroweak interactions. It is described in much more detail in various books [1–4].

The SM consists of two types of particles: fermions which are half-integer spin particles and bosons, having integer spin. The particles of the SM are summarised in fig. 2.1.

The SM fermions make up all the visible matter in the universe. They can be split into leptons and quarks. Both leptons and quarks are involved in electroweak interactions. In addition, quarks carry colour charge and thus interact strongly, while leptons do not. Both leptons and quarks come in 3 generations, where the particles between the generations differ only by their mass. The three charged leptons of the SM are the electron, muon and tau-lepton, each having a corresponding electrically neutral neutrino. The up and down quark constitute the first generation of quarks. The charm and strange quarks make up the second generation and the top and bottom quark the third generation of quarks. This results in a total of 12 fundamental fermions. All the particles have a corresponding antiparticle with the same mass but opposite charge. Fermions have half-integer spin values. This means they possess chirality, i.e. ”handed-ness”, which plays an important role in this thesis. The chirality will be discussed in detail in section 2.1.2

Interactions between the particles are governed by exchange of bosons, particles with integer spin. In total 5 types of bosons exist in the SM. The photon is the carrier of the electromagnetic force. The Z-boson mediates the weak neutral force. The $W^{\pm}$-bosons are the carriers of charged weak interactions. Gluons carry a combination of

colour charges and are the interacting bosons of the strong force. The Higgs boson, discovered in 2012 [5, 6], plays a special role in the SM. It has neither (colour-)charge nor spin. The underlying Higgs mechanism endows the fundamental particles with mass[7–9].

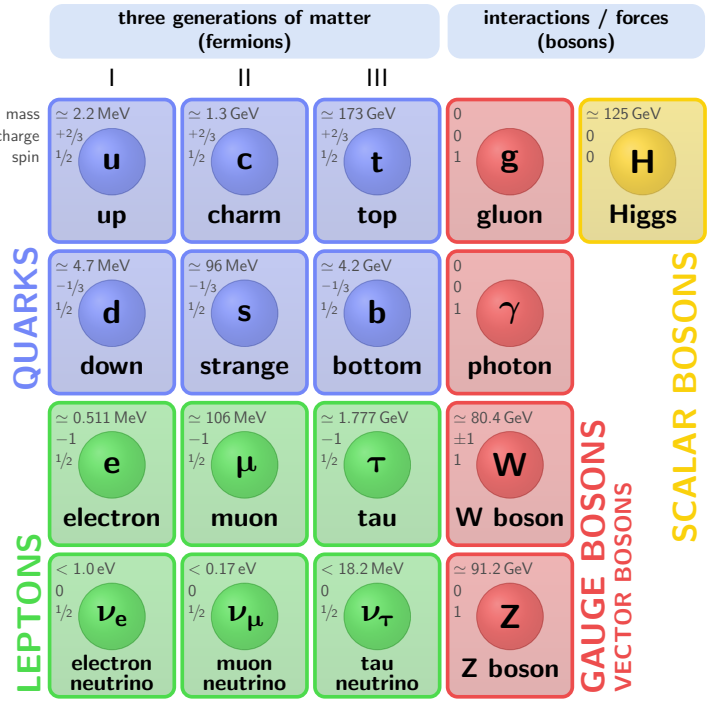

Figure 2.1: Summary of the particles in the SM. Taken from [10].

2.1.2 Quantum field theories

The SM is a Quantum field theory (QFT), mathematically represented by a Lagrange density, where particles are described by fields. The Lagrangian for free fermions is described by the kinematic term:

$$\mathcal{L}_{fermion} = \bar{\psi}\left(i\gamma^{\mu}\partial_{\mu} - m\right)\psi. \tag{2.1}$$

Here ψ corresponds to a fermion field with mass m. Each component of γ^{μ} is a 4×4 matrix. The Lorentz index μ runs from 0 to 3. Using the Euler-Lagrange equation the Dirac equation can be obtained. The solutions of the Dirac equation for ψ are four component spinors. Four different spinor solutions exists, two of which are associated to positive energy solutions and two to negative energy solutions. The positive energy solutions are the fermions of the Standard Model while the negative energy solutions can be interpreted as the antifermions. The particular representation of the

spinors and the γ matrices depends on which basis is chosen, but leads to the same physical results.

A common representation of the γ matrices is the Dirac-Pauli representation:

$$\gamma^0 = \begin{pmatrix} I_2 & 0 \\ 0 & -I_2 \end{pmatrix}, \quad \gamma^i = \begin{pmatrix} 0 & \sigma^i \\ -\sigma^i & 0 \end{pmatrix}, \quad (i = 1, 2, 3). \tag{2.2}$$

Helicity and chirality

Due to the SM fermions being spin one-half particles their component along any axis is quantised to be $\pm\frac{1}{2}$. A useful concept is helicity, defined as the spin $\vec{S}$ of the particle projected onto the movement direction of the particle:

$$\hat{h} = \frac{\vec{S} \cdot \vec{p}}{|\vec{p}|}. \tag{2.3}$$

A positive helicity is defined as a particle with its spin in the movement direction while negative helicity is when the spin points opposite to the particles movement direction. For a fermion, helicity can only be positive or negative, hence one can define two spinors with either positive helicity ($\psi_\uparrow$) or with negative helicity ($\psi_\downarrow$). This is done for both particles and antiparticles, resulting in a total of four spinors. Since the helicity operator commutes with the Hamiltonian for a free massless particle, the helicity states are a basis of four solution of the Dirac equation.

Helicity is a "conserved" quantity in the free SM Lagrangian, meaning that if no external forces act on the particle, it is time-invariant. It is however not Lorentz invariant, since one can always boost a massive particle to a frame where the spin points in the opposite movement direction. For massless particles such a boost does not exist, and helicity is conserved under Lorentz transformations. Chirality is a related Lorentz invariant quantity and is introduced in the following.

Chirality is an important mechanism in weak interactions, which are described in more detail in section 2.1.3. To explain the concept of chirality, an operator γ^5 is introduced as:

$$\gamma^5 = i\gamma^0\gamma^1\gamma^2\gamma^3 = \begin{pmatrix} 0 & I_2 \\ I_2 & 0 \end{pmatrix}. \tag{2.4}$$

One can define two spinors, $\psi_{L/R}$, which are eigenstates of the γ^5 operator:

$$\gamma^5\psi_R = +\psi_R, \quad \gamma^5\psi_L = -\psi_L. \tag{2.5}$$

These two eigenstates are referred to as the chirality of a fermion. Two useful opera-

tors are the two chiral projection operators defined as:

$$P_R = \frac{1}{2}\left(1+\gamma^5\right), \quad P_L = \frac{1}{2}\left(1-\gamma^5\right) \tag{2.6}$$

which are used to project fermions onto a particular chirality:

$$P_{R/L}\psi_{R/L} = \psi_{R/L}, \quad P_{L/R}\psi_{R/L} = 0. \tag{2.7}$$

This means that any spinor can be projected on a left-handed and a right-handed chiral state using these projection operators.

Chirality is not a conserved quantity in time for massive particles, since chirality does not commute with the Dirac Hamiltonian: $[\gamma^5, H_D] = -2m\gamma^0\gamma^5$. A massive left-handed chiral state will evolve into a right-handed chiral state over time and vice versa. For massless particles the commutator is zero and chirality is conserved. For particles, helicity and chirality are related via:

$$\begin{aligned}\psi_\uparrow &\propto \frac{1}{2}\left(1+\frac{p}{E+m}\right)\psi_R + \frac{1}{2}\left(1-\frac{p}{E+m}\right)\psi_L,\\ \psi_\downarrow &\propto \frac{1}{2}\left(1+\frac{p}{E+m}\right)\psi_L + \frac{1}{2}\left(1-\frac{p}{E+m}\right)\psi_R.\end{aligned} \tag{2.8}$$

Here p is the momentum of the particle, E its energy and m the particle mass. It is clear that in the ultrarelativistic limit, $E \gg m$, the second term vanishes and helicity and chirality are equivalent. In the ultrarelativistic limit, the helicity of antiparticles is opposite to their chirality.

2.1.3 Particle interactions

The interaction between fermions are based on the principle of local gauge symmetry, with a non-Abelian gauge group:

$$SU(3)_C \times SU(2)_L \times U(1)_Y, \tag{2.9}$$

where the $SU(3)_C$ symmetry group corresponds to the strong interaction, coupling to the colour charge of particles (hence the label C). Its interacting particles are 8 gluons. The $SU(2)_L \times U(1)_Y$ part is responsible for electroweak interactions, leading to the 3 weak bosons and the photon. In the following electroweak interactions are described in more detail.

Electroweak interactions

The weak interactions and electromagnetic interactions are described jointly in the theoretical framework of electroweak interactions, originally by Glashow, Salam and Weinberg [11–13].

The charge associated with $SU(2)$ is the weak isospin which gives rise to three gauge bosons $W_\mu^{(1)}$, $W_\mu^{(2)}$, $W_\mu^{(3)}$, with coupling strength g and three associated generators T^k. A common representation of T^k is via the 3 pauli-matrices: $T^k = \frac{\tau^k}{2}$. This symmetry mixes with the $U(1)_Y$ group. The generator of this group is the hypercharge Y, resulting in one gauge boson B_μ^0 with associated coupling strength g'.

The four massless gauge bosons of $SU(2)_L \times U(1)_Y$: $W_\mu^{(1)}$, $W_\mu^{(2)}$, $W_\mu^{(3)}$ and B_μ^0 cannot be directly associated to the physically observed photon, $W^\pm$ and Z-boson. During spontaneous symmetry breaking the fields mix, resulting in the physically observed $W_\mu^\pm$ as combinations of $W_\mu^{(1)}$ and $W_\mu^{(2)}$:

$$W_\mu^\pm = \frac{1}{\sqrt{2}}\left(W_\mu^{(1)} \mp i W_\mu^{(2)}\right). \tag{2.10}$$

Gauge boson $W_\mu^{(3)}$ mixes with gauge boson B_μ^0 resulting in the Z-boson and the massless photon. The extent of mixing is given by the weak mixing angle θ_W, also called the Weinberg angle:

$$\begin{pmatrix}\gamma_\mu \\ Z_\mu\end{pmatrix} = \begin{pmatrix}\cos\theta_W & \sin\theta_W \\ -\sin\theta_W & \cos\theta_W\end{pmatrix}\begin{pmatrix}B_\mu^0 \\ W_\mu^0\end{pmatrix}. \tag{2.11}$$

Experimentally it was observed that charged weak interactions only couple to left-handed fermions ψ_L [14]. This is achieved by putting right-handed particles in a weak isospin singlet with $I_W = 0$. Due to the zero mass of neutrinos in the SM, no right-handed singlet is constructed for neutrinos. For quarks each generation has its corresponding right-handed up- and down-type singlet.

The weak interaction couples together the two different left-handed charged fermions within a generation via a $W^\pm$ boson. Therefore, a weak isospin doublet is constructed within each generation. For leptons this doublet is:

$$\phi = \begin{pmatrix}\nu_L \\ l_L^-\end{pmatrix}. \tag{2.12}$$

The corresponding term of charged weak interactions in the Lagrangian is:

$$\mathcal{L}_{weak-interactions} = -\frac{g_w}{\sqrt{2}}\bar{\psi}\left[\frac{1}{2}\gamma^\mu\left(1-\gamma^5\right)\right]\psi W_\mu + h.c. \tag{2.13}$$

In this weak isospin state, both ν and l^- have a total isospin of $\frac{1}{2}$. The third component of the isospin is $I_W^{(3)}(\nu_L) = +\frac{1}{2}$ and $I_W^{(3)}(l_L^-) = -\frac{1}{2}$. The result is that interaction vertices exist between the charged lepton, neutrino and the W-boson. Similarly, one

can construct doublets for each quark generation in a left-handed doublet of an up- and down-type quark:

$$\phi = \begin{pmatrix} u_L \\ d_L \end{pmatrix}. \tag{2.14}$$

The physically observed leptons and quarks are not the same as the interacting states of the weak interaction. This means that the physically observed mass eigenstates are linear compositions of the weak eigenstates. For quarks this is described by the Cabibbo-Kobayashi-Maskawa (CKM)-matrix [15, 16]. Therefore, there are interactions between the up- and down-type quark of different generations. The strength of each coupling is proportional to the corresponding matrix entry. For the connection between top quarks and bottom quarks this is approximately 1. For neutrinos the same mechanism is described by the Pontecorvo-Maki-Nakagawa-Sakata (PMNS) matrix [17, 18]. Both matrices are unitary 3×3 matrices which can be described by 3 rotational angles and a complex phase. The three rotational angles incorporate the mixing between different generations, while the complex phase includes CP-violating terms.

2.2 The top quark

The top quark is the third generation up-type quark, discovered at the Tevatron collider by the D0 [19] and CDF [20] experiments. It is the heaviest observed particle, with a (pole) mass of 172.5 ± 0.7 GeV [21]. As a result of this high mass, the top quark decays predominantly via an electroweak interaction into an on-shell b-quark and W-boson. This makes the top quark unique. Where the lighter quarks hadronise with their spin information washed out by non-perturbative QCD effects, the top quark decays before hadronisation takes place. Therefore the spin properties are transmitted to its decaying particles, enabling to study the spin structure of the tWb vertex. Due to this rapid decay time no bound states involving top quarks can form.

Top quarks are produced through various production mechanisms, as is shown in fig. 2.2. At the LHC top quarks are predominantly produced as $t\bar{t}$ pairs. Fig. 2.3 shows the Feynman diagrams for this production process. The initial state consists of either two gluons (~90 %) or a quark-antiquark pair (~10 %). The production of top quark pairs occurs via strong interactions, making this the ideal probe for studying top-gluon interactions. The second most important top quark production mechanism occurs via an electroweak interaction involving an exchange of a W-boson between a light quark and a b-quark. The interaction mainly takes place through a t-channel interaction, hence the name t-channel production of top quarks. Two other production mechanisms exists where a single top quark is produced. These are the tW and the s-channel production mechanisms. The Feynman diagrams for these three processes are shown in fig. 2.4 with the t-channel interaction in the upper left, the tW interaction in the top right and the s-channel interaction in the bottom. This analysis studies top quark events produced via a t-channel exchange, which is

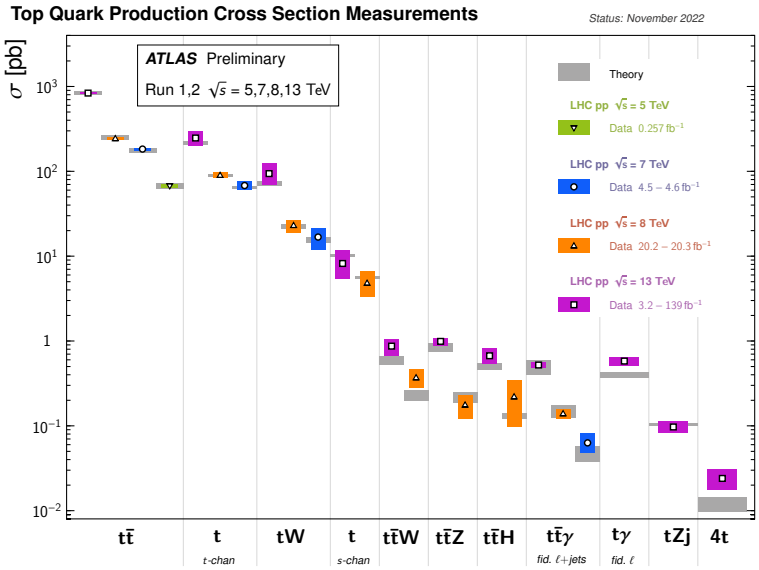

Figure 2.2: Summary of different cross-sections of top quark production mechanism measured by the ATLAS experiment[22].

explained in more detail below.

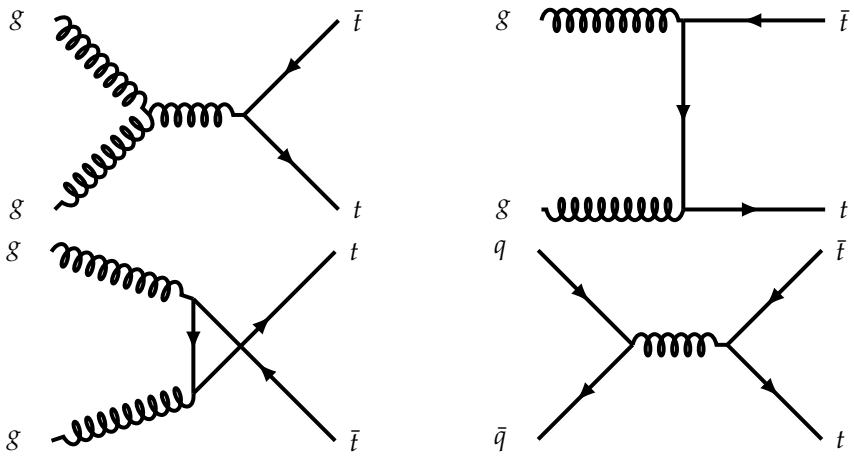

Figure 2.3: Lowest order Feynman diagrams of top pair production.

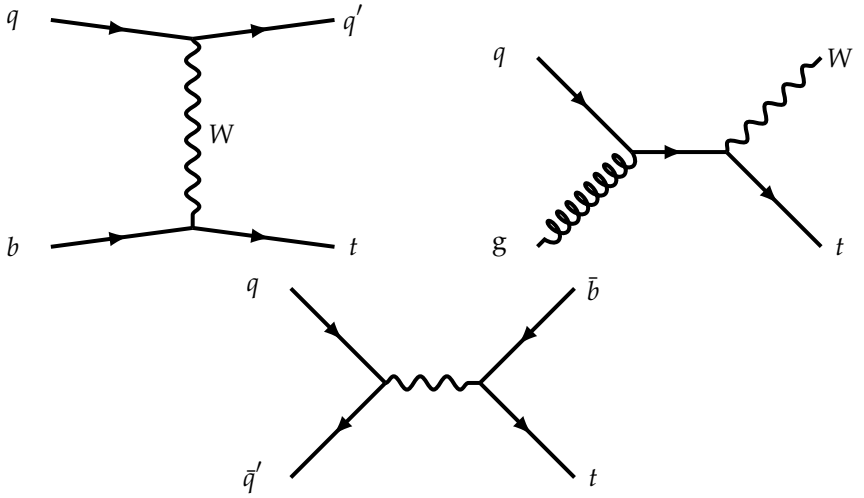

Figure 2.4: Feynman diagrams for the single top production modes at lowest order. On the upper left the t-channel diagram is displayed, the upper right diagram shows the tW process and the bottom diagram shows the s-channel process.

2.2.1 The t-channel single top production mechanism

Since t-channel single top production has the highest cross-section of the electroweak production mechanisms it is an ideal probe to study the interactions between top quarks and W-bosons. The production of a top (antiquark) quark in this channel occurs via the exchange of a W-boson between a (anti) b-quark and a light quark. The dominant diagram, ~80 %, of top quark production has an up-type quark in the initial state and a down-type quark in the final state. The subdominant diagram has an initial state with a down-type antiquark and produces an up-type antiquark. A sketch of the dominant production process in the zero-momentum frame is shown in fig. 2.5. In weak interactions the incoming up and b-quark must have left-handed chirality. This translates to a left-handed helicity due to them being (effectively) massless, resulting in a total spin of zero. The outgoing down quark is also massless, therefore the left-handed chirality is again translated to a left-handed helicity. This means that, due to conservation of angular momentum, the top quark needs to have a left-handed helicity in the zero-momentum frame. This implies that in the restframe of the top quark, its spin points in the direction of the spectator quark. This direction is therefore considered as the optimal spin quantisation axis [23]. The top antiquark production occurs dominantly, ~70 %, via a down-type quark in the initial state producing an up-type antiquark. The subdominant diagram has an initial state of an up-type antiquark, and a final state with a down-type antiquark. For top antiquarks the spin is aligned to the opposite movement direction of the initial down quark in its dominant production mode. The number of left-handed versus right-handed top quarks, with respect to a certain spin quantisation axis, is referred to as the polarisation.

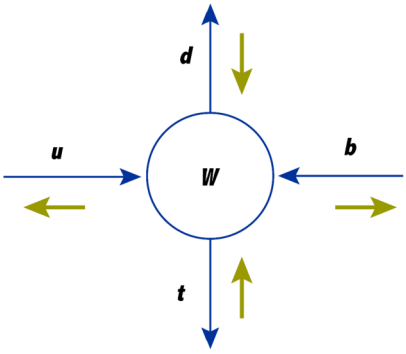

Figure 2.5: Sketch of the spin orientations (yellow arrows) in the zero-momentum frame of the involved particles. The momentum of each particle is indicated by the blue arrow. The left-handed helicities of the incoming (practically massless) b-quark and up quark cancel. The outgoing particles need to conserve spin, i.c. a total helicity of zero. In this frame the outgoing (massless) down quark must have a left-handed helicity as well. Hence, in this frame the top quark helicity must be left-handed, resulting in spin polarised production of the top quark.

2.2.2 Top quark decay

The produced top quark subsequently decays via an electroweak interaction into a W-boson and predominantly a b-quark, due to the CKM element V_{tb} having a value very close to unity. The W-boson can further decay either leptonically or hadronically. If it decays leptonically a charged lepton is produced together with its corresponding neutrino. When the W-boson decays into two quarks it is referred to as a hadronically decaying top quark. The Feynman diagram for the decay is shown in fig. 2.6. This thesis studies top quarks through leptonic decays to either an electron or a muon. These final states are chosen since they are more precisely measured and leave a more distinct signal in the detector.

The top quark decay is also maximaly parity violating and occurs in the SM via a left-handed interaction. Due to the much larger mass of the top quark with respect to the b-quark, the b-quark can be considered as massless. Hence, the left-handed chiral state of the b-quark corresponds to the left-handed helicity state, as can be seen in eq. (2.8). The result of this is that the helicity of the b-quark is always $-\frac{1}{2}$. The W-boson, which has total spin 1, is produced with longitudinal spin component of 0 or -1. The decay into the +1 spin state is forbidden since this would violate spin conservation as the bottom quark is always left-handed. The fraction of produced W-bosons with a certain spin state is referred to as the helicity fractions with components F_R, F_0 and F_L for the +1, 0 or -1 spin states respectively. The decay into a longitudinal W-boson helicity state and a right-handed b-quark is supressed for the same reason. These spin configurations are sketched in fig. 2.7 in the top quark rest frame.

The corresponding helicity fractions at NNLO accuracy are $F_R = 0.0017 \pm 0.0001$, $F_0 = 0.687 \pm 0.005$ and $F_L = 0.311 \pm 0.005$ [24].

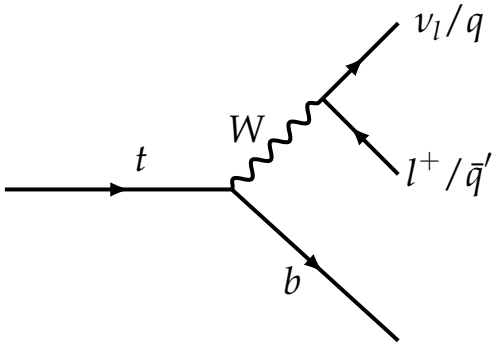

Figure 2.6: The feynman diagram of top quark decay.

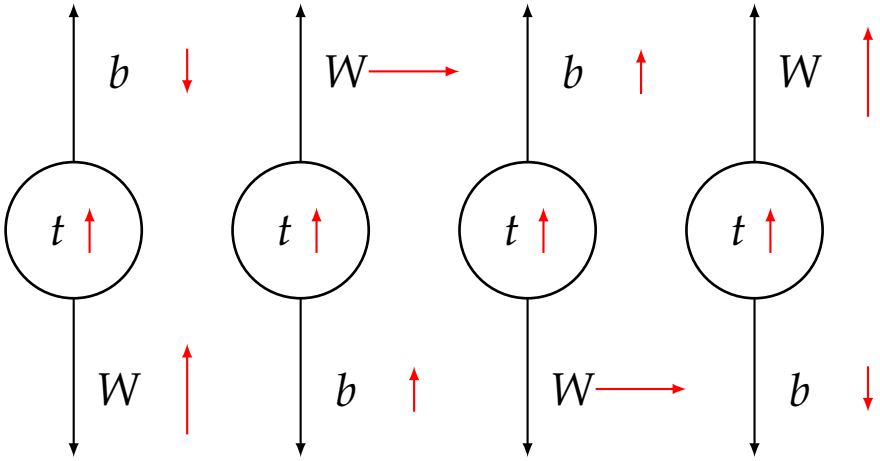

Figure 2.7: Sketch of the possible helicity configurations. The black (red) arrow indicates the movement (spin) direction respectively. The two right configurations are suppressed in the SM since the bottom is produced with right-handed chirality.

2.2.3 Spin sensitive observables.

Analysing the angular spectrum of the top decay products allows for studying the spin structure of tW-interactions. As motivated above, the top spin quantisation axis is chosen as the direction of the spectator quark. The angle between this axis and the decaying particle in the top rest frame, θ_i^z, is an excellent probe of the top production vertex [23, 25, 26]. The definition of the angle is shown in fig. 2.8.

This distribution is predicted to be linear in the cosine of this decay angle:

$$\frac{1}{\sigma}\frac{d\sigma}{d\cos\theta_i^z} = \frac{1}{2}\left(1 + a_i P \cos\theta_i^z\right). \tag{2.15}$$

The slope of this distribution depends on the polarisation of the top quark (P) and the so-called spin analysing power a_i of the decaying particle. In table 2.1 the spin analysing power of different top decay products is shown. The spin analysing power of the lepton is 1, which makes it the perfect candidate to study the polarisation of the top quark since the full spin information is transmitted to it. The reason of this remarkable spin analysing power is the interference between the decay chain via the longitudinal and the left-handed helicity state of the W-boson. This leads to a maximum destructive interference at $\cos\theta^z = -1$.

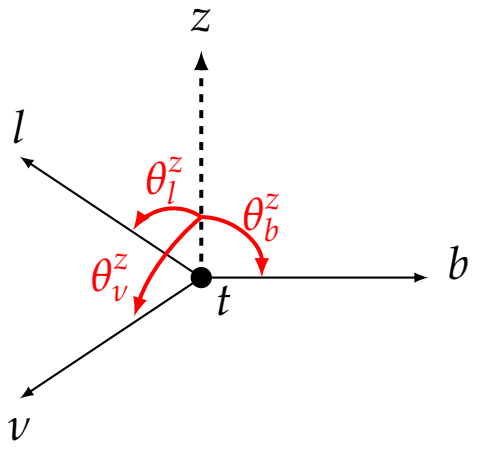

Figure 2.8: Polarisation angles in the top quark rest frame. The top quark spin direction is indicated by the unit vector z. The angles with the different decay products are the polarisation angles θ_i^z.

Table 2.1.: Spin analysing power for different top decay products [26].

top decay product	**spin analysing power α_i**
W	0.403
b	-0.403
ν, u, c	-0.324
$\bar{l}, \bar{d}, \bar{s}$	1.

Using the spin axis and the initial state light quark, a three-dimensional coordinate system can be defined as follows [27]:

$$\hat{z} = \frac{\vec{p}_j}{|\vec{p}_j|}, \qquad \hat{y} = \frac{\vec{p}_j \times \vec{p}_q}{|\vec{p}_j \times \vec{p}_q|}, \qquad \hat{x} = \hat{y} \times \hat{z}. \tag{2.16}$$

Here $\vec{p}_j$ and $\vec{p}_q$ are defined as the direction of the spectator quark and the initial state light quark, both in the rest frame of the top quark. Since the initial quark is not known, the direction of the spectator quark along the beam direction is used as a probe for the initial quark direction of movement. The angles between these three directions and the charged lepton in the top quark's rest frame are defined as the three polarisation angles. These angles are very sensitive to new physics effects, as will be discussed in section 2.3.3.

The helicity states of the W-boson can be measured via the helicity decay angle of the lepton in the rest frame of the W-boson and the movement direction of the W-boson in the top quark rest frame. Using the spin axis of the top quark one can define a second three-dimensional basis [28]:

$$\hat{q} = \frac{\vec{p}_W}{|\vec{p}_W|}, \qquad \hat{N} = \frac{\vec{p}_j \times \hat{q}}{|\vec{p}_j \times \hat{q}|}, \qquad \hat{T} = \hat{q} \times \hat{N}. \tag{2.17}$$

Here $\hat{q}$ corresponds to the movement direction of the W-boson and $\vec{p}_j$ is the momentum of the spectator quark in the top quark rest frame, which corresponds to the top spin axis. The angles between the lepton in the W-boson rest frame and these three unit vectors are referred to as the three helicity angles.

The distribution of the angle between $\hat{q}$ and the lepton has the form:

$$\frac{1}{\Gamma}\frac{d\sigma}{d\cos\theta_l^q} = \frac{3}{8}\left(1+\cos\theta_l^q\right)F_R + \frac{3}{8}\left(1-\cos\theta_l^q\right)F_L + \frac{3}{4}\left(\sin^2\theta_l^q\right)F_0. \tag{2.18}$$

The helicity fractions can be extracted by measuring this angular distribution. Measurements in $t\bar{t}$ events resulted to be $F_R = -0.002 \pm 0.002(\text{stat.}) \pm 0.014(\text{syst})$, $F_0 = 0.684 \pm 0.005(\text{stat.}) \pm 0.014(\text{syst.})$ and $F_L = 0.318 \pm 0.003(\text{stat.}) \pm 0.008(\text{syst.})$ [29]. This is compatible with the predictions of the SM.

2.3 Extensions of the Standard Model

Although the SM describes interactions between elementary particles with great precision, it is not the ultimate description of nature. As will be discussed below it is unable to explain all observations, which suggests that it has to be completed with additional beyond the Standard Model (BSM) physics. This chapter first discusses some shortcomings of the SM. Afterwards commonly used extensions to the SM based on effective field theories (EFT) are introduced.

2.3.1 Phenomena unexplained by the Standard Model

Matter-antimatter asymmetry: The matter in the observable universe consists only of particles and no large amount of antimatter is observed. They were however presumably created in similar amounts during the Big Bang. To create a universe consisting of only matter, the processes in nature have to fulfil 3 requirements, known as the Sakharov conditions [30]. These three conditions are, firstly, that the process is baryon number violating, secondly that the process is charge (C) symmetry and ChargeParity (CP) symmetry violating and thirdly the process occurs out of thermal equilibrium. The SM does include processes that are CP-violating, however measurements at current energy scales have shown that these are about a factor 10^{-7} below the required strength. New sources of CP violation are searched for in many different experiments. Finding new sources of CP violation could explain the matter-antimatter asymmetry.

Strong *CP* problem: In the strong interaction, described by QCD, it is possible to add a CP-violating term. This term gives rise to an electric dipole moment of the neutron. Experiments give an upper limit of this dipole moment resulting in an upper limit on the QCD CP-mixing angle of 10^{-10}. The tiny value of this CP-mixing angle is a theoretical fine-tuning problem, meaning that the parameter has to be precisely adjusted to match with the observations. This is regarded as a problem as there is no a priori reason to explain why the value has to be this small.

Dark matter: From observations of rotating galaxies a deficit of matter was observed. To compensate this deficit a new type of matter is postulated. This matter does not interact electromagnetically, hence the name dark matter. Only their gravitational effects on visible matter can be observed. The SM cannot explain the origin of this matter. Different theories introduce new particles which could be interpreted as dark matter. These new particles can be searched for in either astrophysical observations or collider experiments.

Dark energy: Cosmological observations of the universe show that the expansion of the universe takes place with increasing speed. A new form of energy, called dark energy, driving this accelerated expansion is needed to explain this phenomenon. The SM has no explanation for this.

Particle mass hierarchy and the Higgs boson: The coupling of an elementary particle to the Higgs boson is proportional to the mass of the particle. There is however no fundamental reason why there are three different generations of particles and why their masses differ by many orders of magnitude.

2.3.2 Effective field theory

To extend the SM, several strategies can be adopted. The so-called ultraviolet (UV) complete models describe all new interactions at high energy scales, including new (force-) particles. The new model could predict new particles, which can be searched for in high-energy particle collisions. Additionally, it can change the kinematics of other processes in the SM and by measuring these processes very precisely new

physics can be found. Supersymmetry (SUSY) is an example of such a model, but conclusive experimental evidence for it is lacking.

The approach followed in this analysis is to see the SM as a theory that effectively describes interactions at energies currently in range, but far below the energy scale of a new interaction, e.g. the mass of a new particle. The SM can then be extended by describing the interactions at the currently accessible energy scale in an effective way, while the complete model is not (yet) known. This approach is referred to as the effective field theory (EFT) approach.

Two approaches can be followed when constructing an EFT. The first is the top-down approach, where one starts with a UV complete theory and "integrates out" heavy fields to arrive at an EFT parameterisation. The second approach is a bottom-up approach, where one considers all possible higher dimensional operators up to a certain order and tries to measure the coupling strength of these operators using data. The benefit of this latter approach is that one a priori does not need to assume a particular UV complete model. Since no additional higher mass particles are found at the LHC, the bottom up approach is used in this analysis.

In this approach the symmetries of the SM are conserved and new Lorentz structures are added to the SM to effectively parameterise new physics effects in range of the LHC. It is commonly referred to as the Standard Model Effective Field Theory (SMEFT) approach. A great benefit of the SMEFT approach is that it coherently predicts new effects across different measurement domains such as Higgs boson, top and W/Z-boson production. By measuring all these channels and interpreting them via SMEFT, a coherent way of searching for new physics can be performed. The measurement of EFT parameters related to the tWb interaction is the main topic of this thesis.

The energy (E) dimensionality of the SM Lagrangian is 4, since the action, defined as the integral of the Lagrangian over the 4 spacetime dimensions, has to be dimensionless. In an EFT the dimension four Lagrangian of the SM is extended by higher order operators, which effectively describe the effect of newly produced particles or new interactions at a higher energy scale Λ. Because the operators have a larger energy dimension (d) than E^4, these higher order terms are suppressed by this energy scale with $\Lambda^{(d-4)}$, where d is the dimension of the operator. The resulting Lagrangian has the following form:

$$\mathcal{L} = \mathcal{L}_{SM} + \sum_x \frac{c_x \mathcal{O}_x^5}{\Lambda} + \sum_x \frac{c_x \mathcal{O}_x^6}{\Lambda^2} + ... \tag{2.19}$$

In this expression each higher dimension operator ($\mathcal{O}_x^d$) is multiplied by a coupling strength parameter c_x, which can be a complex number. The strength of the imaginary part of this coupling is denoted as c_{ix}. For operators with $\mathcal{O} = \mathcal{O}^\dagger$ this imaginary part disappears, since the imaginary contribution is zero in the full Lagrangian. Because in this calculation only ratios of c_x and Λ enter the calculations, it is impor-

tant that the condition $\frac{c_x \mathcal{O}_x}{\Lambda} \ll 1$ is fulfilled. This ensures that contributions from higher dimension operators are more and more suppressed. The energy scale Λ is thus set to 1 TeV. The Wilson coefficients c_x are measured by comparing to experiment.

The lowest dimension operator, $\mathcal{O}^5$, has dimension five and are lepton number violating. This is the case for each odd-dimension operator. The operator leads to majorana mass terms for the neutrinos. The effects on collider physics is extremely small and therefore this term is neglected. The second-lowest set of EFT operators are the dimension-6 operators, with a total of 2499 different operators contributing. A few assumptions can be made to reduce the number of contributing operators. Firstly, operators that violate lepton or baryon number are neglected. Secondly an assumption is made that the two lightest quark generations are affected in the same way and only the third quark generation, consisting of the top and bottom quark, is treated separately. This reduces the number of operators to $\mathcal{O}(100)$. Dimension-7 terms are again neglected since they are violating lepton number violation. Terms of dimension 8 are in general much smaller with respect to dimension-6 terms, due to being suppressed by Λ^{-4}. This however does not necessarily mean they are negligible. At present the dimension-8 operators are ignored as no simulations are available.

2.3.3 EFT in single top quark interactions

The t-channel single top quark process is affected by 6 dimension-6 operators[31]. They are:

- $\mathcal{O}^3_{\phi Q} = \left(\phi^\dagger i\overleftrightarrow{D_\mu}\phi\right)\left(\bar{Q}\gamma^\mu\tau^I Q\right)$
- $\mathcal{O}_{tW} = \left(\bar{Q}\sigma^{\mu\nu}t\right)\tau^I\tilde{\phi}W^I_{\mu\nu}$
- $\mathcal{O}^{3,1}_{Q,q} = \left(\bar{Q}\gamma_\mu\tau^I Q\right)\left(\bar{q}\gamma^\mu\tau^I q\right)$
- $\mathcal{O}^{3,8}_{Q,q} = \left(\bar{Q}\gamma_\mu T^A\tau^I Q\right)\left(\bar{q}\gamma^\mu T^A\tau^I Q\right)$
- $\mathcal{O}_{bW} = \left(\bar{Q}\sigma^{\mu\nu}b\right)\phi\tau^I W^I_{\mu\nu}$
- $\mathcal{O}_{\phi tb} = \left(\tilde{\phi}^\dagger i\overleftrightarrow{D_\mu}\phi\right)\left(\bar{t}\gamma^\mu b\right)$

All of these operators have an associated Wilson coefficient, labelled by the same index. Since operators $\mathcal{O}^{3,1}_{Q,q}$, $\mathcal{O}^{3,8}_{Q,q}$ and $\mathcal{O}^3_{\phi Q}$ are hermitian they only have a real coupling strength.

From these 6 operators only the first 3 interfere with the SM and thus have a contribution of order $\frac{c}{\Lambda^2}$, so we henceforth focus on these three. Operator $\mathcal{O}^3_{\phi Q}$ has the same structure as the SM. It involves interactions between a left-handed b-quark producing a left-handed top quark. Therefore, only the total cross-section of the t-channel is affected by $\mathcal{O}^3_{\phi Q}$. Operator $\mathcal{O}_{tW}$ is an interaction between a chiral left-handed b-quark, a W-boson and a chiral right-handed top quark. This results in

a different chirality of the top quark and has a large impact on the distribution of the polarisation angles. It has both a real coupling strength, c_{tW}, and an imaginary coupling strength, c_{itW}. A non-zero value of c_{itW} would flag a new CP-violating interaction. The third operator $\mathcal{O}^{3,1}_{Q,q}$ is a four-fermion interaction. It does not change the spin-structure of the SM and thus has no large impact on the polarisation angles. It has however a large impact on the top quark momentum spectrum.

The analysis prescribed in this thesis uses only the shape of the top momentum spectrum and the polarisation angles and therefore only the EFT coefficients c_{tW}, c_{itW} and c_{qQ} are measured in this work.

2.4 Predictions for proton-proton collisions

This thesis studies highly energetic proton-proton collisions. To test the predictions of the SM, precise estimates of these collisions are needed. This requires very precise understanding of the proton itself, the hard scattering event between the partons inside the proton and the decay and hadronisation of the produced particles in the collision.

The modelling of the collisions is done by factorising the calculation into multiple parts. A sketch of the full process is shown in fig. 2.9. Two partons of the proton undergo a hard scattering process. These initial state partons can radiate additional particles referred to as initial state radiation (ISR). The hard scattering event takes place, where final state particles are produced. These final state particles can again radiate additional particles, which is referred to as final state radiation (FSR). Lastly the hadronisation and fragmentation of the outgoing partons are modelled using dedicated algorithms.

The factorisation theorem [32] states that the cross-section of the proton collisions can be calculated via:

$$d\sigma = \sum_{a,b} \int dx_1\, dx_2\, f_a(x_1, \mu_F)\, f_b(x_2, \mu_F)\, \hat{\sigma}_{ab}(x_1, x_2, \mu_F, \mu_R). \tag{2.20}$$

This equation consists of three functions which are discussed in the following.

2.4.1 Parton Distribution Functions

Functions f_a and f_b are parameterisations of the low energy part of the collision for the two protons. They describe the momentum distribution of the constituents of the two protons and are called parton distribution functions (PDF). Protons consist of three valence quarks (u, u, d) and a sea of gluons and other (anti-)quarks. The PDF $f_a(x_1, \mu_F)$ describes the probability to find a proton constituent a with a certain fraction x_1 of the proton total momentum and μ_F is the factorisation scale, an arbitrary energy scale which marks the boundary between the hard-scattering process and the soft physics descibed by the PDF. The PDF can not be calculated using perturbation

theory. Several groups determine PDFs, using different methods. They are extracted from data of deep inelastic scattering collisions between protons and electrons and proton-proton collisions, typically at lower energy scales. The evolution of the PDFs to higher energy scales is described by the DGLAP equation [33–35]. Examples of PDF sets are the NNPDF set [36–38] and the MSTW PDF set [39].

2.4.2 Hard scattering calculations

The second part of the equation, $\hat{\sigma}_{ab}(x_1, x_2, \mu_F, \mu_R)$, describes the cross-section of the hard scattering process. The cross-section depends on the squared matrix element (ME) which is perturbatively calculated using the Feynman rules, which depend on the underlying theory. The hard scattering cross-section depends on the factorisation scale μ_F and the renormalisation scale μ_R [40], the scale at which the coupling constants are computed.

The set of Feynman diagram with the lowest power of a coupling constant is referred to as the leading order (LO) approximation. Higher order diagrams have additional vertices, which reduces their contribution by powers of the coupling constant α. Thus, the approximation with one more vertex is called next-to-leading-order (NLO) approximation. These include virtual corrections which occur via additional loops in the Feynman diagram and real emissions which happen via radiation of an additional parton. Having two additional vertices leads to the next-to-next-to-leading-order (NNLO) approximation and so forth. Including higher order calculations makes the prediction more accurate and more precise. Higher order corrections also reduce the dependency on μ_F and μ_R.

Changing the Lagrangian by adding for example new operators changes the matrix element and consequently the (differential) cross-section. Additional dimension-6 operators in an effective field theory alter the matrix element as follows:

$$\mathcal{M} = \mathcal{M}_{SM} + \sum_x \frac{c_x}{\Lambda^2} \mathcal{M}^6_x. \tag{2.21}$$

The differential cross-sections can thus be parameterised by:

$$d\sigma \propto |\mathcal{M}|^2 = |\mathcal{M}_{SM}|^2 + 2\sum_x \frac{c_x}{\Lambda^2} \mathrm{Re}(\mathcal{M}^*_{SM}\mathcal{M}^6_x) + \sum_{x,y} \frac{c_x c_y}{\Lambda^4} |\mathcal{M}^6_{x,y}|. \tag{2.22}$$

This means that the (differential) cross-section has both a linear and a quadratic dependency on the dimension-6 Wilson coefficients. The contribution of the quadratic terms in an EFT model are usually smaller than the linear terms due to an additional factor of $\frac{c}{\Lambda^2}$.

If the width of a produced intermediate particle is small in comparison to its decay width, the narrow width approximation can be used. This allows to factorise the cross-section of the process into a production cross-section multiplied by the branching fraction of the decay. In the case of single top production this means:

$$d\sigma(pp \to Wbj) = d\sigma(pp \to tj)BR(t \to Wb) = d\sigma(pp \to tj)\frac{\Gamma(t \to Wb)}{\Gamma(t)}. \quad (2.23)$$

Here, the branching ratio is expressed as the ratio of the partial width divided by the total decay width of the top quark. Since the top quark almost always decays into a W-boson and a b-quark, the branching ratio of this decay is approximately 1.

2.4.3 Fragmentation and hadronisation

The fragmentation and hadronisation of the produced quarks in a hard scattering event is performed using dedicated parton shower (PS) models. These models shower the produced quarks by creating emissions of the partons using dedicated algorithms. This showering is performed in an ordered way. A common method to perform the showering is in a so-called transverse-momentum-ordered way. In this method the first emission is the most energetic and in each subsequent emission the energy is reduced. This ensures that the strong coupling constant α_s grows with every splitting step. An alternative approach is to perform the showering in an angular-ordered way, where the opening angle between the emitted parton is largest for the first emission and decreases in every step. After the energy of the particles reaches the hadronisation scale (~ 1 GeV) they are converted into colour neutral states of hadrons. This results in collimated sprays of particles, which are referred to as jets. An important caveat when interfacing the NLO matrix element calculation to the parton shower algorithm is to correctly take care of real emissions and additional radiations performed in the showering. Dedicated merging algorithms ensure that no double-counting takes place of additional radiations. The showering depends on certain input parameters which are estimated in data. An example of this is the value of the strong coupling constant at the mass of the Z-boson. The process of estimating these input variables to best match data is called "tuning".

2.4.4 Monte Carlo simulators

To model all these steps Monte Carlo (MC) event generators are used. Several generators exist which differ in how each step is implemented and how the different steps are combined. MC generators used in this work are described briefly below.

MADGRAPH/aMC@NLO [42, 43] is a general purpose MC generator, able to simulate the ME up to NLO in QCD for many SM processes at the LHC. It is widely used to model BSM scenario's and to obtain EFT predictions. It can be interfaced to PS algorithms. To solve the problem of double counting NLO ME calculation with PS emissions a negative counterterm is added in the calculation. This results in negative

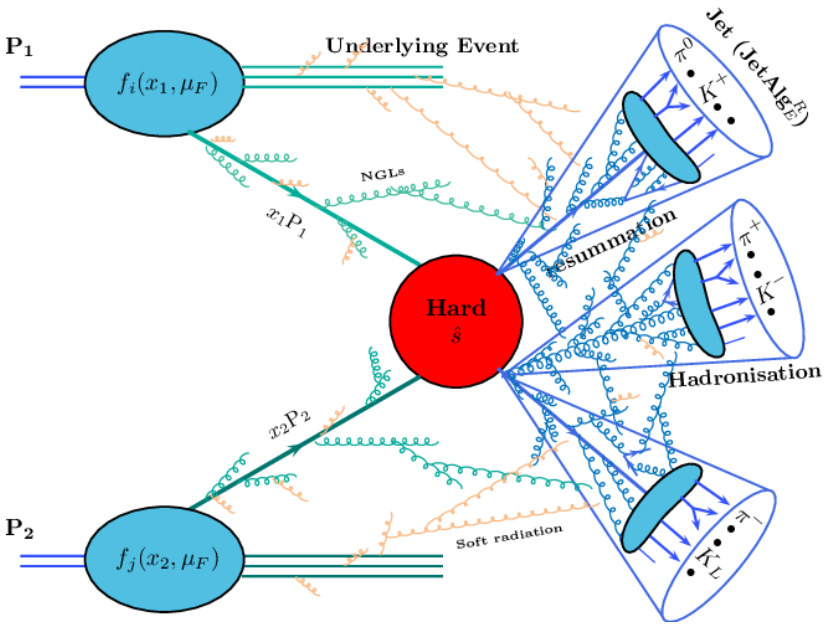

Figure 2.9: Sketch of a typical proton-proton collision [41].

weights for a fraction of the events.

POWHEG [44–46] is an alternative MC generator for simulating NLO accurate processes at the LHC for a wide range of LHC processes. As aMC@NLO it can be easily interfaced to PS algorithms but has a different approach with respect to double counting of real emissions. Instead of adding a negative counterterm it vetoes the highest energetic parton of the PS algorithm if the emission is above a certain scale defined by POWHEG. This ensures that almost no negative weights are created[1]. The matching between the ME emission and the PS emission is controlled by a so-called h_{damp} parameter, which damps real emission of POWHEG by a factor $h_{damp}/(h_{damp} + p_T)$.

SHERPA [47] is a general purpose MC generator able to both calculate ME at NLO and subsequently shower it using its own PS algorithm based on the Catani-Seymour dipole factorisation [48, 49].

PYTHIA [50] is a general purpose MC event generator able to generate events at LO including ME+PS. It is commonly used as a PS algorithm taking the input from other ME calculations and model the showering of the produced particles. It can be

[1] POWHEG is an abbreviation for POsitive Weight Hardest Emission Generator

interfaced to both aMC@NLO and POWHEG. PYTHIA uses a momentum-ordered PS algorithm. This work uses the A14 tune of PYTHIA8 [51].

HERWIG [52, 53] is also a general purpose MC event generator. It is used as an alternative PS algorithm to PYTHIA and uses an angular-ordered PS algorithm.

MADSPIN [54] can be applied after a ME generator to decay heavy particles with spin. The decay is based on ME techniques allowing to preserve angular correlations between the decaying particles. The output of MADSPIN can be interfaced to PS algorithms.

EvtGen [55] is a MC event generator able to simulate the decay of heavy flavour particles, e.g. hadrons containing c- and b-quarks, produced in the hadronisation step.

Chapter 3

The Atlas Experiment at the Large Hadron Collider

To enable the study of top quarks in a model independent way, they have to be produced in a controlled environment. Currently the only machine capable of reaching high enough energies for producing top quarks is the Large Hadron Collider (LHC) located at the CERN laboratory, near Geneva in Switzerland. The analysis presented in this thesis uses proton-proton collisions recorded by the ATLAS experiment during the running period from 2015 until 2018 referred to as Run 2. This chapter introduces the LHC and the ATLAS experiment during the data taking period of Run 2. For future analysis, upgrades of the experimental setup are needed. These upgrades are also briefly discussed in this chapter.

3.1 The Large Hadron Collider

The LHC [56] is a hadron-hadron collider installed in the 27 km long tunnel of the former LEP collider [57]. It consists of two separate rings containing particles travelling in opposite directions. The LHC is operating during the largest fraction of the year with protons, however it can be filled with heavy ions as well. The LHC is designed to collide protons at a centre of mass energy of 14 TeV.

Before protons enter the LHC, they pass through a sequence of pre-accelerators. After exiting each pre-accelerator, the protons have increased energy and are injected in the next step of the chain. The complete chain of accelerators at the CERN site is illustrated in fig. 3.1. The chain starts with hydrogen gas which is ionised to create a continuous stream of protons. They are collected into proton bunches and consequently accelerated in the LINAC, the Proton Synchroton Booster (BOOSTER), the Proton Synchroton (PS) and the Super Proton Synchroton (SPS). They are finally injected into the LHC with an energy of 450 GeV, where they are accelerated to their final energy. A variety of different filling schemes exist, targeting various instantaneous luminosities and creating different conditions. An important element in these conditions is the number of pile-up collisions. These pile-up collisions are additional proton on proton scattering events which happen during the same bunch-crossing. Having more protons inside one bunch increases the number of hard scattering collisions, however also results in more pile-up interactions.

The proton-proton collisions used in this analysis are recorded at a centre of mass energy of 13 TeV. The particles collide at four points along the LHC ring. At these locations particle detectors are stationed. There are two general purpose detectors located at the LHC ring: ATLAS [58] and CMS [59], designed to study the full spectrum of proton collisions. These two experiments operate independently of another which allows for cross-confirmations of their measurements. The two other exper-

iments are ALICE [60] which focus is on studying the quark gluon plasma created during heavy ion collisions and LHCb [61], a forward spectrometer focussing on the study of b-hadrons. In addition to the four main detectors, several smaller experiments are installed at the LHC with dedicated physics objectives, like very forward physics or search for exotic particles.

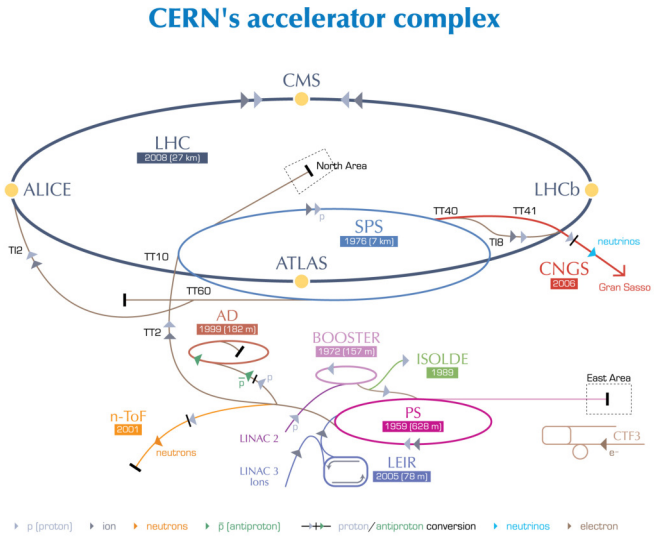

Figure 3.1: Sketch of the CERN accelerator complex [62].

3.2 The ATLAS experiment

The ATLAS (A Toroidal LHC ApparatuS) detector is the largest detector around the LHC ring. The analysis presented in this thesis uses data collected by the ATLAS detector during the Run 2 data taking period. It is briefly described in this chapter. A detailed description can be found in technical design reports [58, 63, 64]. This section outlines the detector configuration as it was during the Run 2 data taking period and briefly discusses the upgrades for the future runs.

The ATLAS detector allows one to measure and identify multiple, different particles in an almost 4π solid angle. It consists of a cylindrical barrel region enclosed by end-cap structures on both sides. It is build in multiple layers of different subdetectors. These subdetectors are the Inner Detector (ID), the electromagnetic and hadronic calorimeters (ECAL/HCAL) and the Muon Spectrometer (MS). The ID is enclosed by a superconducting solenoid providing a 2 T magnetic field. In the MS, superconducting coils provide a toroidal field of typical 0.5 T. A cutaway illustration of the ATLAS detector is shown in fig. 3.2.

The ATLAS detector uses a right-handed Cartesian coordinate system in which the x-axis point towards the center of the LHC, the y-axis upwards and the z-axis in the

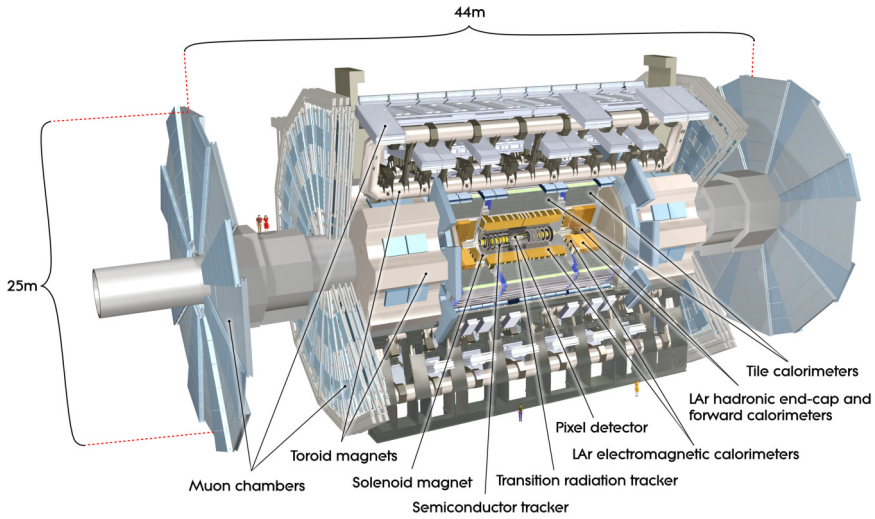

Figure 3.2: Cutaway sketch of the ATLAS detector from [58].

beam pipe direction. Due to the (almost) cylindrical shape of the ATLAS detector it is common to use cylindrical coordinates (r, ϕ). Here ϕ is the angle with respect to the x-axis and r the distance, both in the transversal plane. Instead of using the polar angle θ with respect to the z-axis it is common to use the pseudo-rapidity η defined as $\eta = -\ln\left(\tan\left(\theta/2\right)\right)$. The pseudo-rapidity is commonly used in collider physics. It is related to the rapidity defined as $y = \frac{1}{2}\frac{E+p_z}{E-p_z}$. Differences in rapidities are invaraint under Lorentz transformations. In the ultrarelativistic limit the pseudorapidity and rapidity are equivalent.

Signature of particles

In total there are six different types of (isolated) particles traveling through the detector. These are electrons, muons, photons, charged and neutral hadrons and, lastly, neutrinos. They each leave a different trace in the ATLAS detector.

Electrons are electrically charged and thus leave a trace in the ID and are then stopped in the ECAL. Photons are also stopped in the ECAL however leave no trace in the ID. Charged hadrons, like protons or charged pions, leave a trace in the ID, but are stopped in the HCAL. Neutral hadrons, like neutrons, leave no trace in the ID and are stopped in the HCAL. Muons leave a trace in the ID, deposit some energy (typically few GeV) in the calorimeters, but are not stopped to leave a trace in the MS. Finally, neutrinos do not interact with any material and escape the detector unnoticed. Their presence can only be inferred from a momentum imbalance in the transversal plane. A sketch of how all these different particles interact is shown in fig. 3.3. The jets, originating from a quark or gluon, consist of a condensed spray of all particle mentioned above.

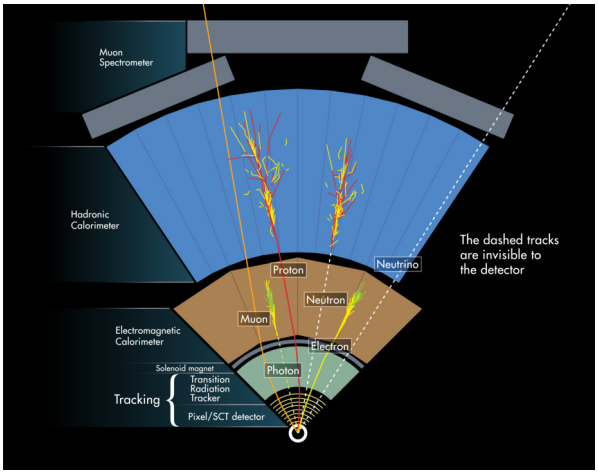

Figure 3.3: Illustration of the different traces the different particles leave in the ATLAS detector [65].

In order to reconstruct t-channel single top events, the ATLAS detector has to fulfil the following requirements. It needs to be able to identify the produced electrons and have a good momentum and energy measurement from the inner detector and electromagnetic calorimeter. A very precise momentum measurement of muons using a combination of measurements in the ID and the MS is required. Also, it needs to provide a good measurement of the energy and direction of the produced jets by the calorimeter system. Additionally, it needs to distinguish jets originating from b-quarks and light quarks, using primary and secondary vertex information in the ID.

3.2.1 Triggering

Besides providing measurements of particles for offline reconstruction, the interesting events need to be real-time selected, which is called triggering. Triggering is the process of selecting which collisions are stored for further processing and which collisions are rejected. This is done to reduce the rate of which collision events are written to disk for further analysis such that the computing infrastructure is able to handle the vast amount of data. The trigger system reduces the rate from 1.7 billion proton-proton collisions per second to about 1000 collisions per second used for further processing.

The ATLAS trigger system is based on a two-stage trigger system. The first stage, called L1 trigger, is a hardware based trigger system, using information of the calorimeter and muon subdetectors. Dedicated triggers looking for electrons, muons, photon, τ-jets, and missing transverse energy are implemented in this stage of the trigger. Events that are selected by this trigger are temporary stored and passed into a second stage trigger called the High Level Trigger (HLT). This trigger does a simplified event reconstruction. Based on the properties of the reconstructed particles of this

event reconstruction, the event is either discarded or stored to tape. Examples of properties that are searched for are muons or electrons above a certain momentum threshold.

3.2.2 Inner Detector

The Inner Detector (ID) is the subsystem directly surrounding the beam pipe of the LHC. When charged particles travel through the detector material they leave a signal in the ID, enabling tracking of the particles trajectory. Due to the magnetic solenoid field these trajectories are curved. This information is exploited to identify the charge of each particle and to reconstruct its transversal momentum.

The ID consists of three different subdetectors, each with different technology and precision. The most inner layer is the Pixel detector. It is made out of four layers of silicon pixel sensors in the barrel region and 3 disks in each end-cap structures. It covers a region up to $|\eta| < 2.47$. The innermost layer of the barrel region is referred to as the Insertable B-Layer (IBL), at a radial distance of only 33 mm from the beam-line. The second subdetector is the Semi-Conducting Tracker (SCT). It is made of silicon strips with a mean pitch of 80 μm. It consists of four layers in the barrel region and nine discs in both end-cap regions. The outermost part of the ID is the Transition Radiation Detector (TRT). It is based on straws, drift-tubes with 4 mm diameter, embedded in radiator material. The TRT mainly provides hit positions of the trajectories used for pattern recognition and also improves the electron identification. A cutaway view of the ID can be seen in fig. 3.4.

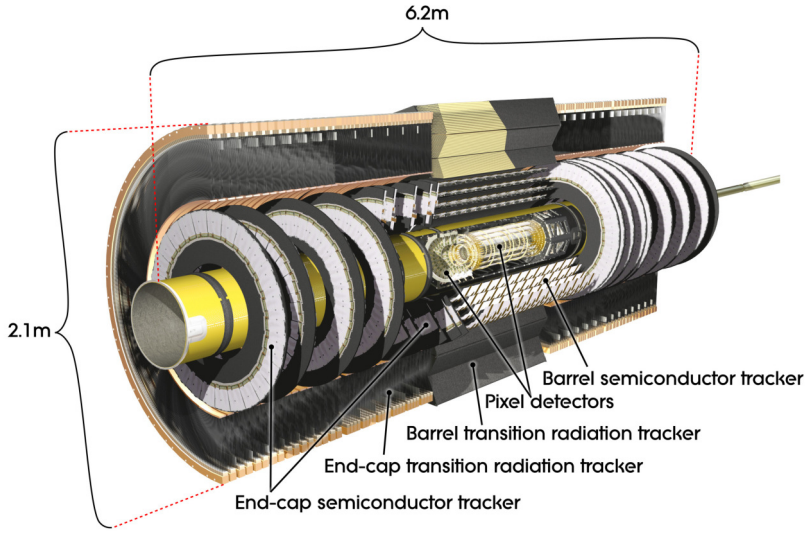

Figure 3.4: Cutaway view of the ID from [58].

Upgrades of the ATLAS tracking system

After the Run 3 period, expected to end in 2024, the LHC will be upgraded to run with even higher collision rates for the HL-LHC period starting in 2029. The ATLAS detector will be upgraded in this time. The current ID will be replaced with the newly built ITk [66]. Silicon will be used as detecting material for the full ITk, making it more radiation hard and allowing for higher granularity. The tracker will cover an area up to pseudorapidity values of 4. This allows for a precise identification of b-jets even in the forward direction. To cope with the higher bandwidth the readout system will be upgraded to the FELIX system [67].

The ITk will be installed in 2028. This upgrade will also include the ATLAS High Granularity Timing Detector (HGTD) [68]. This detector uses low gain avalanche detector technology to achieve a timing resolution of 30 ps for minimum-ionising particles. It covers the pseudorapidity region between 2.4 and 4.0. Its main purpose is to reduce the background from pile-up by an improved vertex association, using timing information.

3.2.3 Calorimeters

The ATLAS calorimeter system consists of two layers, the electromagnetic calorimeter (ECAL) and hadronic calorimeter (HCAL). The main goal of the calorimeters is to stop particles and measure the energy they deposited. It stops all known stable particles apart from muons and neutrinos. The calorimeter used in ATLAS exploits the sampling method, where passive layers are interleaved by active layers. The passive material slows down and eventually stops particles. A sketch of the ATLAS calorimeter system can be found in fig. 3.5.

Electromagnetic particles (electrons and photons) create an electromagnetic shower in the ECAL. The energy of the intitial particle is obtained from the measurement of ioniosation in the active layers. The ECAL is made of liquid Argon as active and lead for the passive material. The barrel region covers up until $|\eta| < 1.475$, the end-caps cover the range from $1.357 < |\eta| < 3.2$. The overlap region $1.357 < |\eta| < 1.52$ is used for services.

Hadronic particles also develop a shower, but they penetrate much deeper and are mainly measured in the HCAL. The HCAL surrounds the ECAL with passive layers of steel and either scintillator or liquid Argon as active material. The barrel region covers ranges up to $|\eta| < 3.2$, while the end-cap regions cover $3.1 < |\eta| < 4.9$.

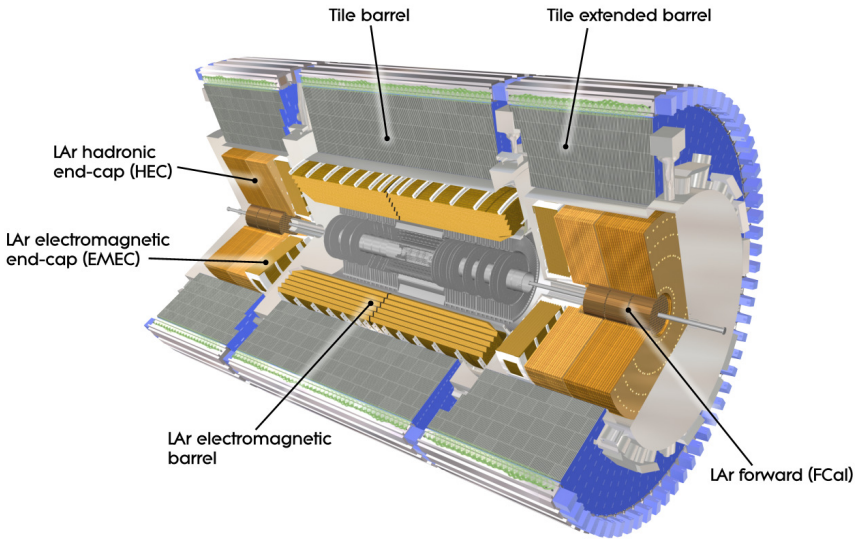

Figure 3.5: Cutaway view of the calorimeter system of the ATLAS detector from [58]

3.2.4 Muon Spectrometer

The outermost layer of ATLAS is the Muon Spectrometer (MS). A sketch of the MS can be seen in fig. 3.6. The goals of the MS are to firstly identify and precisely measure the momentum of the traversing muons and, secondly, to provide a trigger signal.

Highly energetic muons only lose a few GeV by ionisation in the calorimeters and are thus not stopped. Other particles are stopped in the calorimeters[1], apart from neutrinos that escape undetected. A reconstructed track in the MS is therefore assigned to a muon.

The barrel region of the MS covers $|\eta| < 1.05$. It consists of three layers with increasing radial distance named Inner, Middle or Outer. Each layer has 12 different sections with increasing η-ranges, six for positive η and six for negative η. To cover different ranges in ϕ the MS consists of in total 16 sectors, 8 so-called large sectors and 8 small sectors.

The end-cap of the MS is covering a range from $1.05 < |\eta| < 2.7$. It is made out of 3 wheels, also referred to as small, middle or outer wheel depending on their distance to the interaction point in the longitudinal direction. The small wheel has a diameter of approximately 9.3 meter while the middle and outer have a diameter of approximately 20 meter. It consists of 16 sectors in ϕ, again corresponding to large

[1] Very high energetic hadronic showers might not be completely stopped and particles may punch through the calorimeters, leading to noise into the MS.

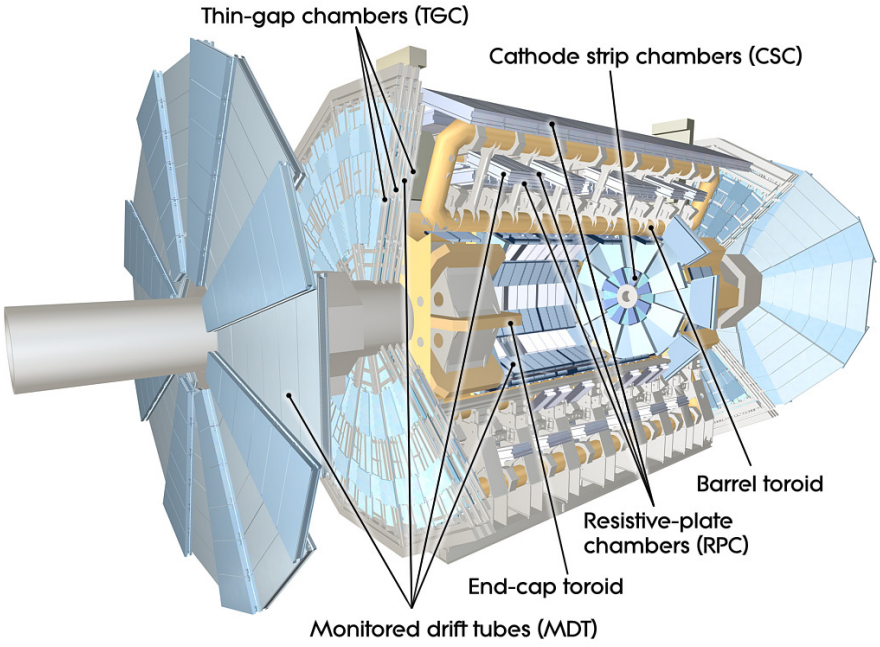

Figure 3.6: Cutaway view of the ATLAS MS taken from [58]

and small sectors.

The precision measurement of the muon trajectory is mostly based on panels or chambers with Monitoring Drift Tubes (MDT). Each MDT chamber consists of six layers of tubes with a diameter of 30 mm, which allow for precise tracking of the muons. In the forward region of the small wheel, Cathode Strip Chambers (CSC) are installed. These are multi-wire proportional chambers, able to deal with the large flux in the very forward region.

To trigger on muons, dedicated trigger chambers are installed in ATLAS. These chambers are able to detect the passage of a muon within a single bunch-crossing and have thus a time resolution of only a few nanoseconds. In the middle and outer barrel layers Resistive Plate Chambers (RPC) are installed, while in the middle wheels Thin Gap Chambers (TGC) are installed.

Future upgrades to the ATLAS MS

Upgrades to the ATLAS MS after Run 2 include the installation of the New Small Wheel (NSW) and the Barrel Inner chambers in the Small sector (BIS) of η regions 7 and 8. They have been installed in the MS before the start of the ongoing Run 3 data taking period in 2022. Especially the installation of the NSW is important to deal with the large number of collisions during the Run 3 data taking period as it can more reliable trigger on muons in the very forward region of the detector. This

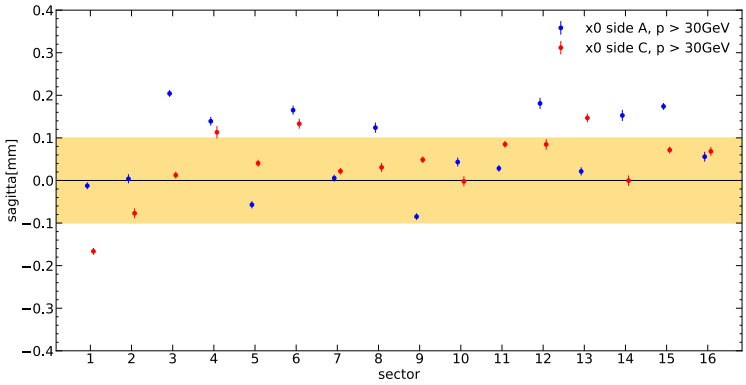

Figure 3.7: Distribution of the false sagittas measured for each sector for side A in blue and side C in red. The yellow band indicates values of $\pm$ 100 μm .

allows one to make a coincidence between the middle and innermost wheel in the trigger, reducing the fake trigger rate significantly. The new small wheel consists of two types of chambers, small Thin Gap Chambers (sTGC) and MicroMegas (MM). The NSW is constructed to have two MM chambers surrounded by sTGC chambers. In appendix A.1 a study is presented on the alignment of the newly installed NSW. It shows the measurement of the alignment of the middle chamber with respect to the inner and outer chamber resulting in a ”false” sagitta. In fig. 3.7 a summary of the false sagittas is shown. These measurements are used to calibrate the alignment system to the targeted tolerance of 100 μm.

For Run 3 the innermost barrel chamber in the small sector, BIS1-6, will be replaced. The new chambers will have six layers of small Muon Drift Tubes (sMDT) with a diameter of 15 mm (compared to the 30 mm tubes of the MDT chambers). This creates place to install an additional RPC chamber in the innermost layer of the MS to improve the trigger by adding a hit in the trigger system. To accommodate this space, the in-plane alignment system has to be more compact. At Nikhef, a prototype alignment frame was constructed and tests are performed on how this prototype is able to reconstruct deformations. These studies are documented in appendix A.2.

3.3 Detector simulation

To understand how the particles produced in proton-proton collisions interact with the detector, a simulation of the complete ATLAS detector is needed [69]. To achieve this, a simulation of the ATLAS detector is done within the GEANT4 framework [70–72]. Within this simulation, the passage of particles travelling through the detector is modelled and the signals that these particles leave in the various subsystems is given as an output. This simulation takes as input hard scattering collisions. The final state particles of these events are overlaid with different pile-up conditions allowing to

simulate how these events look like when recorded by the ATLAS detector. As this simulation requires a lot of computing resources, an additional lightweight detector simulation is also available. This simulation parameterises the response of different particles in the calorimeters. This lightweight simulation of the detector is called ATLFAST.

This simulation of the ATLAS detector enables comparisons of different processes directly with the data recorded by the ATLAS detector. It additionally allows to compare the particles before detector simulation, referred to as ”truth level”, with their corresponding response after the detector simulation, which is referred to as ”reco”, or ”reconstruction level”. Events at reconstruction level are used to optimise the analysis, as well as to extract the EFT parameters from the collected data.

Chapter 4

Reconstruction of physics objects

The signals from the different sub-detectors have to be combined to reconstruct the detected objects that are associated with particles produced in the collision. This chapter describes how these objects are identified and selected for the analysis of single top quark events.

4.1 Leptons

Events originating from t-channel events are required to have exactly one electron or muon measured in the ATLAS detector. As explained in the previous chapter, electrons and muons have a specific, very different, signature in the sub-detectors. Below, the identification criteria for both electrons and muons are described.

4.1.1 Electrons

The electron reconstruction and identification is described in more detail in [73]. Here the strategy and main requirements are briefly discussed.

The electrons produced in the collisions will leave a trace in the ID and the ECAL. The energy of electrons is mostly determined by the ECAL, while the direction is determined by the ID. Clusters of energy deposits in the ECAL are combined and matched to tracks in the ID to have a precise reconstruction of the electron energy, taking into account Bremstrahlung of the initial electron. The energy resolution is of the order of 7 % for electrons with an E_{T} of 10 GeV and reduces to 1 % for electrons with E_{T} >100 GeV. To calibrate the electron momentum measurement and correct for differences in electron identification, scale factors are applied. These corrections are determined from data of $Z \to ee$ events.

Electrons are required to have a p_{T} larger than 30 GeV. Additionally, electrons that are too forward to leave a trace in the ID, $|\eta| > 2.5$, are not used in this analysis.

Since narrow jets and photons could mimic the signature of electrons, a likelihood-based electron identification algorithm is used [73]. Three different working points are defined (Loose, Medium, Tight), with a higher signal efficiency for the Loose working point to Tight with a lower signal efficiency, but the highest background rejection. This analysis uses electrons passing the Tight working point to measure the EFT coefficients. This working point has an efficiency of 70 % for electrons with an E_{T} of 30 GeV, and increases to an efficiency of 85 % for electrons with an E_{T} of 100 GeV. The efficiency also depends on the pseudorapidity of the electron, with a higher efficiency in the central region. When an additional electron fullfills the

LooseAndBLayerLH[1], the event is discarded to suppress the contribution of non t-channel events.

To reduce the amount of (fake) electrons originating from decaying particles inside jets, an additional requirement on the "isolation" of the electron is applied, based on the surrounding energy deposits and tracks. Several working points are defined depending on the energy measured in a cone around the electron candidate. The Tight working point is used in this analysis which has an efficiency of 80 % at 30 GeV and increases to almost 100 % at a transversal energy of 100 GeV.

Electron candidates which pass the LooseAndBLayerLH identification criterion and do not pass the Tight isolation criterion are used to estimate the background originating from multijet events, which will be discussed in more detail in section 5.1.4.

4.1.2 Muons

In the following the reconstruction and identification of muons used for this analysis is briefly discussed. A more detailed explanation is presented in [74].

Muon tracks are reconstructed from hits in the MS and the ID. In this analysis so-called combined muons are used. A combined muon is reconstructed in an iterative approach, where individual tracks are first created in the ID and MS separately. After matching the MS track with an ID track, the final muon track is obtained from refitting the combined information. This procedure provides the best estimate of the muon momentum from the track's curvature, which is driven by the ID for low momentum, while for $p_{\mathrm{T}} > 100\,\mathrm{GeV}$, the accuracy of the MS dominates the momentum measurement.

The muon momentum measurement is calibrated from data and additional scale factors are used to correct for differences of the muon identification between simulation and data. These corrections are estimated from $Z \to \mu\mu$ and $J/\psi \to \mu\mu$ events. The relative resolution of the charge-to-momentum ratio, q/p, is of the order of 5 % for muons with $p_{\mathrm{T}} < 300\,\mathrm{GeV}$ and degrades for higher momentum.

Similar to the electron identification strategy, several working points are defined with different signal efficiency and background rejection [74]. These are based on requirements on the number of matched hits to the track in the ID and MS and the significance of the charge-to-momentum ratio q/p. The muons that are selected for the analysis described in this thesis are required to pass the medium working point which has an efficiency of 98 %. When in the event 1 charged lepton is selected and when an additional muon fullfills the medium identification criteria with a $p_{\mathrm{T}} > 10\,\mathrm{GeV}$, the event is vetoed.

Additionally, several working points depending on the isolation of muons are created. These serve to remove muons originating from jets. The PromptLeptonImprovedVeto PLIVTight working point is used with an efficiency of selecting muons of 80 % at a p_{T} of 30 GeV and increasing to 95 % for muons with a $p_{\mathrm{T}} > 40\,\mathrm{GeV}$.

[1] This criterion requires electrons to pass the Loose identification working point, while additionally having a hit in the innermost pixel layer.

Muons that do not pass this isolation requirement are used to estimate the contribution from the multijet background.

4.2 Jets

A jet is a spray of final state particles, originating from the fragmentation and hadronisation of partons. The energy of the particles are measured in the calorimeter, with the exception of muons and neutrinos. The charged particles also lead to tracks in the ID. The combined information of ID tracks and calorimeter information is used for the reconstruction of the jets with the particle flow algorithm [75]. The energies of these particles are combined using clustering algorithms, which serve to reconstruct the four momentum of the parton that initiated the jet. These clustering algorithms should be infrared and collinear safe, meaning that perturbative QCD radiation at low energy or emissions in the parton direction do not alter the reconstruction of the jet.

In ATLAS the anti-k_{T} algorithm [76] is used to reconstruct jets. It takes the energy clusters in the calorimeter and the tracks in the ID as input objects and combines these objects into a set of jets. It combines two objects depending on their transverse energy, k_{T}, and their relative distance, $\Delta R_{ij} = \sqrt{\Delta\phi_{ij}^2 + \Delta\eta_{ij}^2}$. This procedure is applied iteratively. The objects are combined using the following measure:

$$d_{ij} = min(k_{\mathrm{T},i}^{-2}, k_{\mathrm{T},j}^{-2}) \frac{\Delta R_{ij}^2}{R^2}. \tag{4.1}$$

This value is computed for each combination, i and j, in the collection. The two objects with the lowest value of d_{ij} are combined, resulting in a new object with the combined energy and direction. This is repeated with the remaining objects and this newly combined object. If d_{ij} exceeds $k_{\mathrm{T},i}^{-2}$, object i is removed from the collection and called a jet. The jet radius parameter, R, can be tuned to optimise the correspondance between jets and the initial (hard) parton. The common value of $R = 0.4$ is used in this analysis. The resulting set of objects of this algorithm is the jet collection.

To reduce the contamination of jets originating from pile-up, a special tagger called Jet Vertex Tagger (JVT) is used. This tagger combines tracking information into a multivariate discriminator to veto jets that do not originate from the primary vertex of the hard scattering process. In the forward region a similar discriminator is created referred to as f(orward)JVT.

The energy calibration of jets takes into account effects from pile-up contributions and differences in calorimeter response between data and detector modelling effects [77]. This is done by applying a set of corrections to each jet which are estimated both from MC studies and data. The resulting relative energy resolution on jets is approximately 20 % for jets with p_{T} = 30 GeV and decreases to approximately 10 % for jets with a p_{T} around 100 GeV.

4.2.1 Flavour tagging

A crucial tool for performing top quark analysis is to identify jets that originate from a b-quark. This procedure is referred to as flavour tagging. The b-quarks lead to hadrons with a relatively long lifetime that travel a small, but detectable distance before they decay. Therefore not all tracks in these jets originate from the point where the hard scattering occurs, e.g. the primary vertex (PV), but several have a small displacement, leading to a high impact parameter. In some cases it is even possible to reconstruct the point of decay, the secondary vertex (SV), see fig. 4.1. Jets originating from lighter quarks or gluons do not have this feature and their tracks point to the primary vertex.

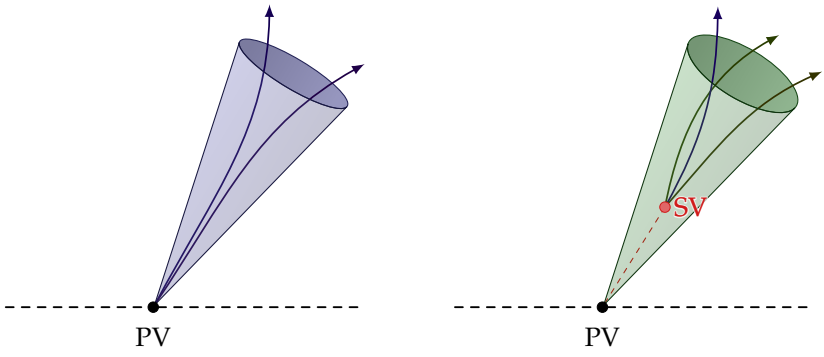

Figure 4.1: Sketch of the signatures induced by jets originating from light quarks on the left and from b-quarks on the right.

Additionally, jets originating from b-quarks produce on average more stable particles in comparison to jets from other quarks or gluons. A multivariate algorithm is used to identify jets initiated by b-quarks. This algorithm is based on several low level algorithms. These take as input the track information of the jets and search for secondary vertices, calculate impact parameters and compute the number of associated particles to the secondary vertex. The output of these low level algorithms is combined using a feed forward neural network with three output nodes that correspond to the probability that the jet is originating from a b-quark a c-quark or a light quark. This discriminator is called DL1r [78]. As this algorithm depends on reliable track reconstruction, only central jets are considered with a pseudorapidity up to 2.5.

In fig. 4.2 a plot of the b-jet efficiency versus the background rejection is shown in the upper panel for the DL1r tagger and two previous taggers. In this plot the solid line shows the rejection against light-jets and the dashed line the rejection against c-jets. The lower two panels show the improved rejection rate with comparison to the BDT based tagger MV2c10.

In total four different working points are provided that differ in the b-quark identification efficiency and the rejection of jets originating from other quarks or gluons. These points have a b-jet tagging efficiency of 85 %, 77 %, 70 % and 60 %. This analy-

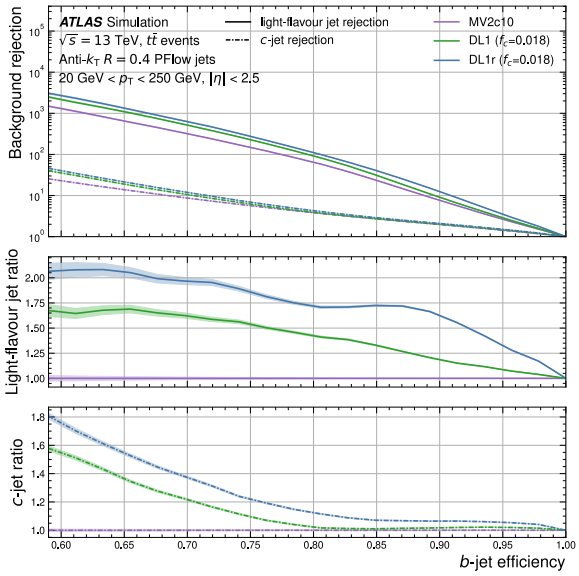

Figure 4.2: Distribution of the b-jet efficiency versus the light- and c-jet rejection rate for the taggers MV2c10, DL1 and DL1r. The lower panels show the ratio with respect to MV2c10 for light-jets and c-jets [78].

sis uses the tightest working point of 60 %. If a jet passes (fails) this working point, it is considered a b-jet (light-jet).

The identification efficiency is calibrated to data for these working points and corrections depending on the energy and direction of the jet are applied to the simulations.

4.3 Missing energy

The incoming protons (and their constituents) do not have a significant momentum in the transversal plane. Hence, an imbalance of the transverse momentum, the missing transverse energy $E_{\mathrm{T}}^{\mathrm{miss}}$ is used to recover the (transverse) energy of neutrino's that leave the detector undetected. The $E_{\mathrm{T}}^{\mathrm{miss}}$ reconstruction is computed via the sum of the transverse energies of all calibrated objects in the event and energy deposits that are not associated to any object, but are compatible with the primary vertex [79, 80]. The missing momentum is calculated separately for the x and y direction using the same approach.

In t-channel single top production, all $E_{\mathrm{T}}^{\mathrm{miss}}$ is assigned to the neutrino of the W-boson. The z component of the missing energy cannot be reconstructed without prior assumptions, as the momentum of the initial state particles is unknown. Therefore, the known mass of the W-boson is used to constrain the neutrino z component. By solving the quadratic equation of the invariant mass one can calculate the longitudinal

neutrino momentum:

$$(p_W)^2 = (m_W)^2 \tag{4.2}$$
$$(p_W)^2 = (p_l + p_\nu)^2 = m_l^2 + 2(E_l E_\nu - \vec{p}_l \cdot \vec{p}_\nu) \tag{4.3}$$
$$(m_W)^2 = m_l^2 + 2(E_l E_\nu - \vec{p}_l \cdot \vec{p}_\nu) \tag{4.4}$$

This equation has in general two solutions. In previous works, the solution with the lowest z momentum for the neutrino was taken [81]. In this analysis the solution where the sum of the W-boson momentum and the b-jet momentum is closest to the top mass of 172.5 GeV is used. This selects the correct solution slightly more frequently.

4.4 Kinematic Likelihood Fit

The final goal of the analysis presented in this thesis is to have the most stringent measurement of the EFT parameters in single top. Background events dilute the sensitivity. Therefore a likelihood apprach is used to reconstruct the full event topology in order to only select events, which are kinematically compatible with single top t-channel production. Furthermore, this approach rejects genuine t-channel single top events, which are not properly reconstructed.

The likelihood fit is implemented in the KLFitter package [82]. In this approach the energy of the final state particles are fitted for each event to a likelihood using constraints of the t-channel single top production. This likelihood is based on transfer functions $W(E_i^{meas}|E_i)$, where E_i^{meas} is the detector-level measurement for reconstructed object i, E_i is its parton-level equivalent, and $i \in \{\text{light-jet}, b\text{-jet}, \text{lepton}, E_{\text{miss,x}}, E_{\text{miss,y}}\}$. Constraints on the reconstructed top and W-boson masses are applied in this likelihood. Additionally, constraints requiring that the sum over all final state particles of p_x and p_y be consistent with zero within uncertainty σ are applied. This results in the following likelihood:

$$\begin{aligned}
&\ln \mathcal{L}\left(E_{\text{light-jet}}, E_{\text{bjet}}, E_{\text{lepton}}, E_{\text{miss,x}}, E_{\text{miss,y}}\right) \\
&= \ln\left(B(m_{l\nu}|M_W, \Gamma_W)\right) + \ln\left(B(m_{Wb}|M_t, \Gamma_t)\right) \\
&+ \ln\left(W_{\text{light-jet}}(E^{\text{meas}}_{\text{light-jet}}|E_{\text{light-jet}})\right) + \ln\left(W_{\text{bjet}}(E^{\text{meas}}_{\text{bjet}}|E_{\text{bjet}})\right) + \ln\left(W_l(E_l^{\text{meas}}|E_l)\right) \\
&+ \ln\left(W_{\text{miss}}(E^{\text{meas}}_{\text{miss,x}}|E_{\text{miss,x}})\right) + \ln\left(W_{\text{miss}}(E^{\text{meas}}_{\text{miss,y}}|E_{\text{miss,y}})\right) \\
&- \frac{1}{2}\{\frac{\sum p_x}{\sigma}\}^2 - \frac{1}{2}\{\frac{\sum p_y}{\sigma}\}^2.
\end{aligned} \tag{4.5}$$

In this equation $B\left(m_{l\nu}|M_{\mathrm{W}},\Gamma_W\right)$ is the Breit-Wigner distribution for the $\ell\nu$ system with a mean value at m_W= 80.4 GeV and a width of Γ_W = 2.1 GeV. The second term involving $B\left(m_{\mathrm{Wb}}|M_t,\Gamma_t\right)$ is a Breit-Wigner distribution for the Wb system which has its mean value at m_t = 172.5 GeV and has a width of Γ_t = 1.5 GeV. The transfer functions $W(...)$ are described by double Gaussians having the following form:

$$f(E_i^{\mathrm{meas}}|E_i) = \frac{1}{\sqrt{2\pi}(\sigma_1 + p_3\sigma_2)}(e^{-\frac{1}{2}(\Delta E-\mu_1)/\sigma_1^2} + p_3 e^{-\frac{1}{2}(\Delta E-\mu_2)/\sigma_2^2}), \tag{4.6}$$

with:

$$\Delta E = \frac{E_i - E_i^{\mathrm{meas}}}{E_i}. \tag{4.7}$$

The 5 parameters are for each object different and are functions of the energy of the object and its pseudorapidity. In the following, the estimation of the transfer functions is described and afterwards the performance of the likelihood fit is discussed.

4.4.1 Transfer functions

The transfer functions are estimated from a SM MC simulation of the t-channel process. The hard scattering is modelled using POWHEG. The decay of the top quarks is modelled via MADSPIN to preserve angular correlations. The events are interfaced with PYTHIA8 for the hadronisation and fragmentation. The decay of b-quarks and c-quarks is performed within the EvtGen program. These generators are described in more detail in section 2.4.4. A full detector simulation, as discussed in section 3.3, is used to obtain the response to all final state particles.

In this section the estimation of the b-jet transfer functions is discussed. The other objects have been obtained using a similar approach. The transfer functions for each object are presented in appendix B. These functions are used in the kinematic likelihood fit.

For the estimation of the b-jet transfer functions, events with exactly one b-jet are selected. The reconstructed b-jet and the truth b-quark have to be matched within $\Delta R(\mathrm{reco,truth}) < 0.3$. These are then split according to the pseudorapidity of the b-jet taking into account the detector lay-out. The regions are defined as:

- $|\eta_b| < 0.8$,
- $0.8 < |\eta_b| < 1.37$,
- $1.37 < |\eta_b| < 1.52$,
- $1.52 < |\eta_b| < 2.5$.

In each region a specific set of transfer functions is estimated. The estimation of the transfer function in the region for $\eta_b < 0.8$ is discussed as an example. This is done in three steps.

First histograms of the relative difference between reconstructed b-jet energy and truth b-quark energy are made in bins of the truth b-quark energy:

$$\Delta E = \frac{E^b_{\text{truth}} - E^b_{\text{reco}}}{E^b_{\text{truth}}}. \tag{4.8}$$

To each histogram a double Gaussian function is fitted and its parameters are extracted. The histograms with the fitted double Gaussian functions are shown in fig. 4.3. The individual fits agree for most energy regions very well, with some small discrepancies in the low energy range. As one can see from these figures, the distribution peaks at zero which implies that for the majority of the events, the original energy is reconstructed. The width of the distributions decreases for higher energies as is expected since the relative energy resolution is better for higher energetic jets. An interesting feature is the tail towards higher energies, which becomes more pronounced at higher energies. This tail probably originates from b-jets that decay leptonically, creating a charged lepton and a neutrino, which escapes the detector undetected.

In the next step, each parameter of the double Gaussian is fitted as function of the truth b-quark energy, where the mid-value of the range is used. This is done to have parametric descriptions for the transfer function and not just a binned estimation, where one has to interpolate between the points. The empirical functions for each of the 5 parameters of the double Gaussian function from eq. (4.6) are:

$$\mu_1 = a_1 + \frac{b_1}{E_{\text{Truth}}}, \tag{4.9}$$

$$\sigma_1 = a_2 + \frac{b_2}{\sqrt{E_{\text{Truth}}}}, \tag{4.10}$$

$$p_3 = a_3 + \frac{b_3}{E_{\text{Truth}}}, \tag{4.11}$$

$$\mu_2 = a_4 + \frac{b_4}{\sqrt{E_{\text{Truth}}}}, \tag{4.12}$$

$$\sigma_2 = a_5 + b_5 E_{\text{Truth}}. \tag{4.13}$$

Each of the parameters that define the double Gaussian depends on two parameters, a_i and b_i. The obtained double Gaussian parameters are first fitted individually to obtain starting parameters a_i and b_i. In the final step, all 10 parameters of the double Gaussian shapes, are re-fitted simultaneously to the histograms. The result of this fit gives the final set of transfer functions. The obtained transfer functions for all the energy ranges are shown in fig. 4.4. Although still a small discrepancy at the lowest energy bin of 35 GeV is observed, all the other transfer functions agree well with the histograms.

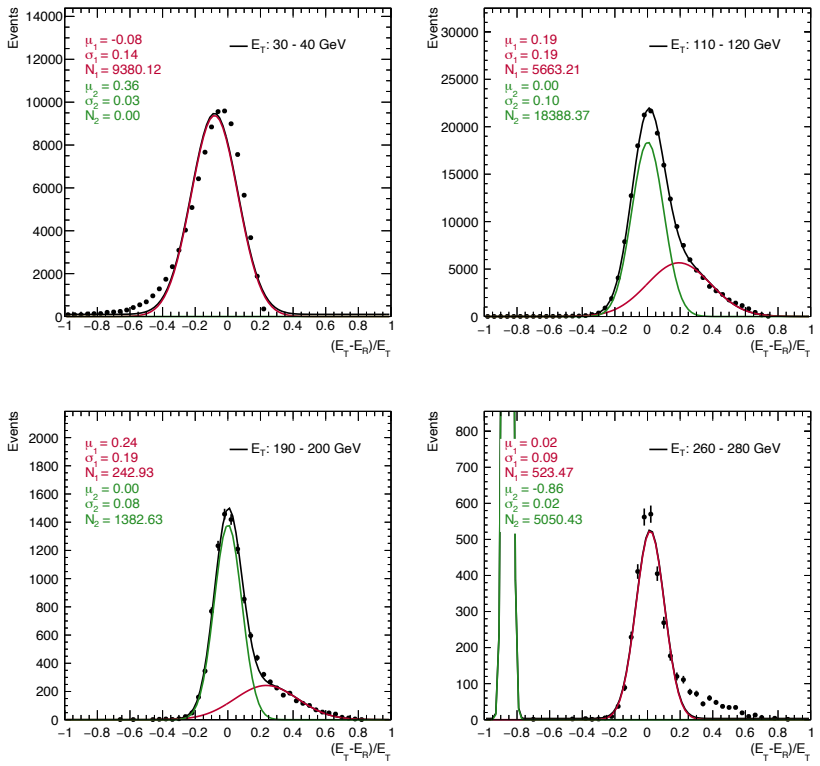

Figure 4.3: Distributions of $\frac{E_T - E_R}{E_T}$ for b-jets with $|\eta| < 0.8$ with the full double Gaussian fit in black performed in each energy range individually. The two individual Gaussians are shown in red and green. The range of the true b-quark energy is shown in the histogram.

4.4.2 Performance

To study the performance of the KLFit, simulated events are used, generated with POWHEG. The reconstructed objects of each individual event are used as input for the fitting procedure. For the longitudinal momentum of the neutrino, p_z, both solutions of the quadratic equation are taken into account. The solution that leads to the highest likelihood is used, the other one is disregarded.

In fig. 4.5 the likelihood distribution from KLFit for all the events is shown. A double peak structure is observed with the majority of events at the peak around -32. Studies on the events with a likelihood around -40 showed that these events have a wrong estimation of the neutrino momentum. These mostly originate from events where in the decay of the b-quark additional neutrinos are produced. These neutrinos escape the detector and thus contribute to the missing energy. Consequently, the relation between the missing energy and the neutrino originating from the top

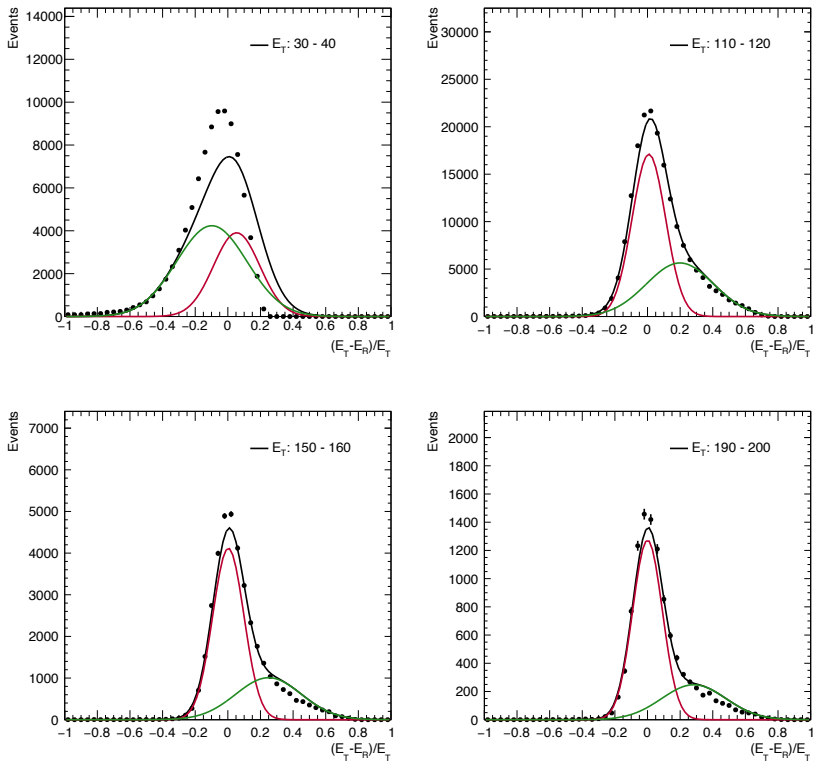

Figure 4.4: Distributions of $\frac{E_T - E_R}{ET}$ for b-jets with $|\eta| < 0.8$ with the full double Gaussian fit in black using the parametric description of the transferfunctions. The two individual Gaussians are shown in red and green. The range of the true b-quark energy is shown in the histogram.

decay is affected, leading to badly reconstructed events. This will be exploited to reduce the number of background events and events that are not well reconstructed by selecting only events with a minimum log-likelihood of -36.

The performance of the kinematic likelihood fit is further investigated by comparing several variables at reconstruction level with their corresponding value at parton truth level. For this, the reconstructed and the truth particle are matched on a ΔR(reco,truth) criterion. Events are matched if ΔR(reco,truth) is smaller than 0.1 for leptons and smaller than 0.3 for light- and b-jets. The results for p_{T} and p_z of the neutrino are shown in fig. 4.6. The KLFit result is represented by the green histogram, which exhibits a substantial improvement with respect to the original (classic) reconstruction in red. For completeness the distribution in black shows the original distribution before applying the likelihood selection.

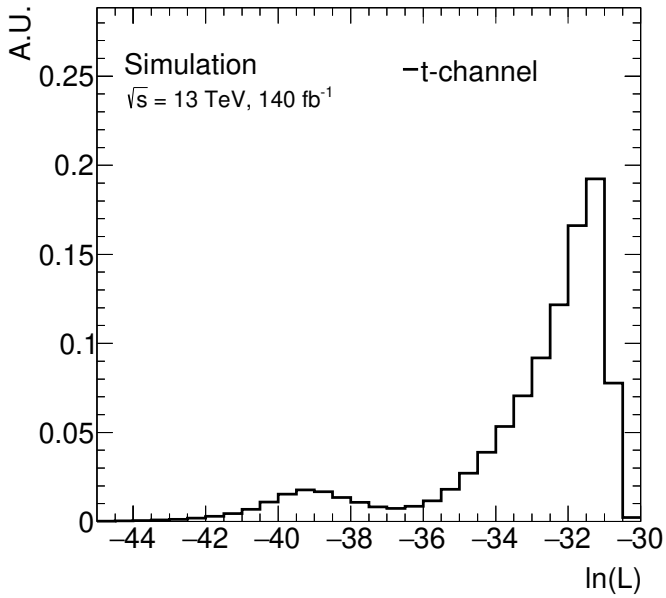

Figure 4.5: The result of KLFit, showing the distribution of the logarithm of the likelihood for all events for a POWHEG single top t-channel MC simulation.

In figs. 4.7 to 4.9 the results for p_{T} and η are shown for the b-jet, W-boson and the top quark. The distributions demonstrate that reconstructed events fitted with KLFit have better agreement with their corresponding truth value. The distributions exhibit a smaller width and are more centred around zero. Furthermore, the tails of the b-jet p_{T} and the neutrino p_{T} distributions are substantially reduced. The improved reconstruction of these two particles is also beneficial for the top and W-boson reconstruction. In contrast, this has only a modest effect on the reconstruction of the angular observables, as can be seen in fig. 4.10. The angular observables are only slightly improved after the KLFit, which can be explained by correlations between the reconstructed objects and the, still large, uncertainty on the longitudinal momentum of the neutrino.

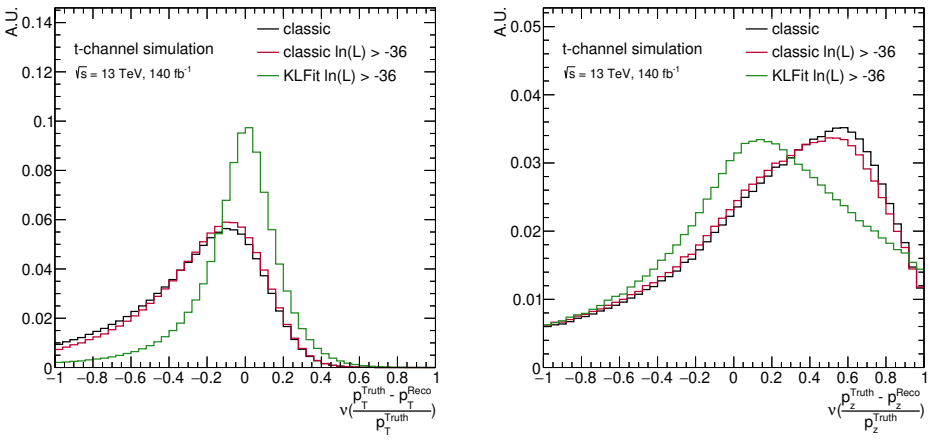

Figure 4.6: Distribution of the difference between reconstruction and truth level for p_{T} (left) and p_z (right) of the neutrino. Results are shown for KLFit and the original (classic) reconstruction before and after selection on the likelihood value as indicated in the histograms.

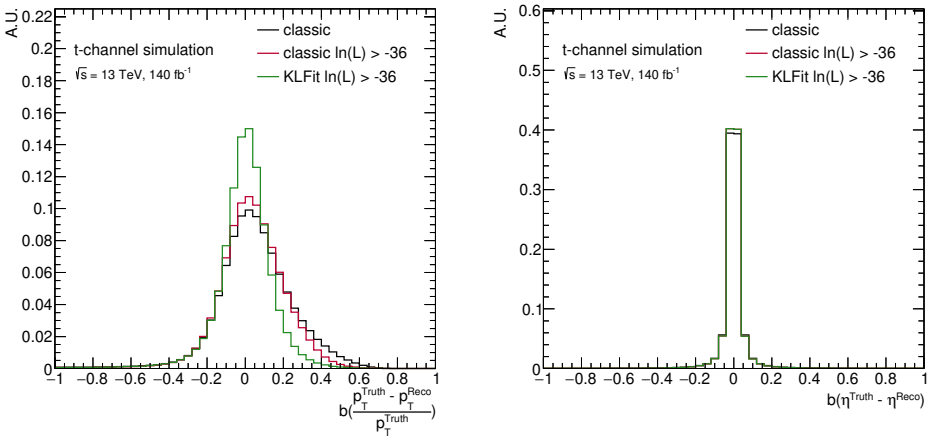

Figure 4.7: Distribution of the difference between reconstruction and truth level for p_{T} (left) and η (right) of the b-jet. Results are shown for KLFit and the original (classic) reconstruction before and after selection on the likelihood value as indicated in the histograms.

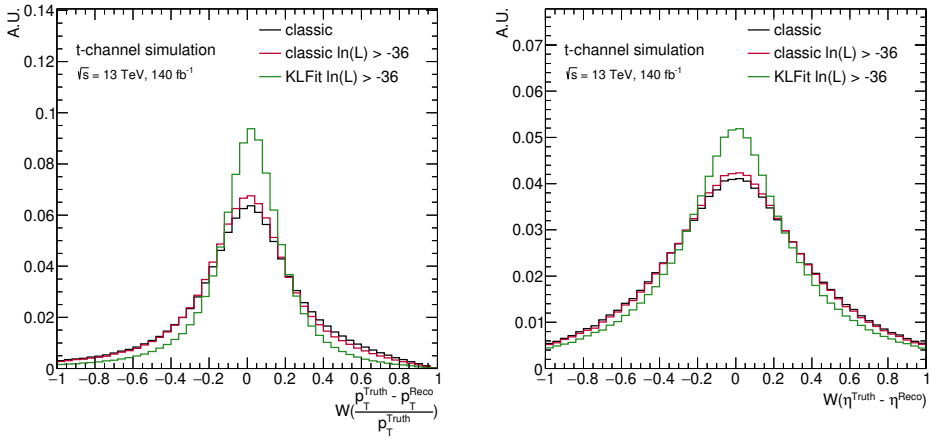

Figure 4.8: Distribution of the difference between reconstruction and truth level for p_{T} (left) and η (right) of the W-boson. Results are shown for KLFit and the original (classic) reconstruction before and after selection on the likelihood value as indicated in the histograms.

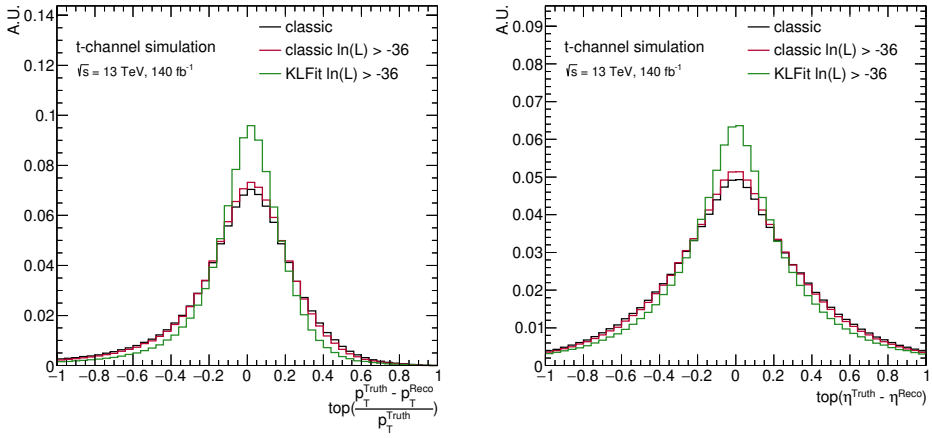

Figure 4.9: Distribution of the difference between reconstruction and truth level for p_{T} (left) and η (right) of the top quark. Results are shown for KLFit and the original (classic) reconstruction before and after selection on the likelihood value as indicated in the histograms.

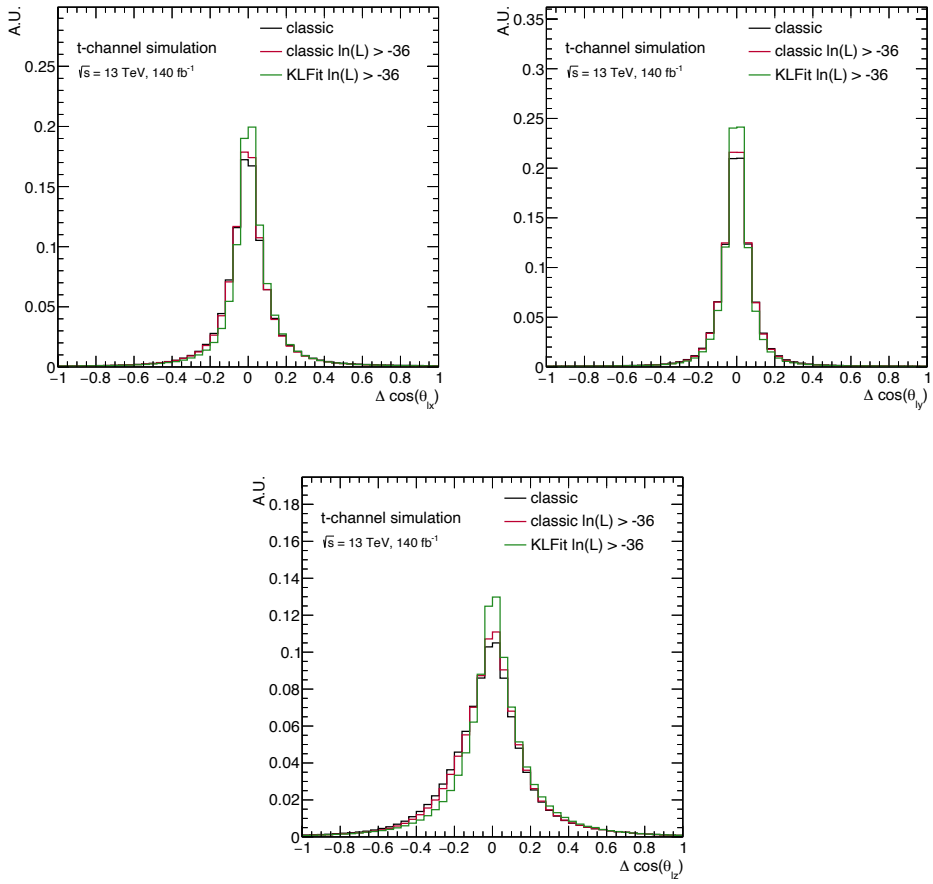

Figure 4.10: Distribution of the difference between reconstruction and truth level for $\cos\theta_{\ell x}$, $\cos\theta_{\ell y}$ and $\cos\theta_{\ell z}$. Results are shown for KLFit and the original (classic) reconstruction before and after selection on the likelihood value as indicated in the histograms.

4.4.3 Use of KLFitter in the further analysis

In the previous section, it has been demonstrated that KLFitter enables to flag mis-reconstructed single top quark events by using a selection on the likelihood of $\ln(L) > -36$. Additionally it is able to reduce the number of background events, which will be discussed in section 5.2. Therefore a cut on the likelihood value of $\ln(L) > -36$ will be applied to reject such events.

It also has been shown that the resolution of observables in t-channel MC events is improved by KLFitter. Despite this apparent virtue, the further analysis on EFT parameters presented in this thesis, will **not** use KLFitted observables. Initial studies to optimise the sensitivity of the analysis for EFT effects have suggested that using KLFitter leads to larger systematic uncertainties. This can be understood by the fact that the relation between MC truth and reconstruction level is exploited, which is affected by both instrumental and modelling systematic uncertainties.

As will be discussed in the following chapters, systematic uncertainties dominate this analysis. Therefore, using KLFitter other than for rejecting mis-reconstructed and background events, does not improve the sensitivity to EFT effects in this analysis.

Chapter 5

Modelling, selection and EFT parameterisation

The aim of the analysis is to search for new physics interactions by a precise study of the t-channel single top production process. The expected effects of new physics interactions are described by EFT and the goal is to measure the corresponding EFT parameters in data collected by the ATLAS experiment. The analysed data were recorded by the ATLAS detector during proton-proton collisions with a center of mass energy of $\sqrt{s} = 13\,\text{TeV}$ at the LHC from 2015 to 2018. This resulted in $140\,\text{fb}^{-1}$ of collected data.

To search for these new interactions in t-channel candidate events, the background contributions have to be minimised and possible effects of EFT operators have to be understood. The t-channel event selection is optimised based on a precise modelling of both background and signal processes. The signature and modelling of the t-channel process and all background processes are discussed in section 5.1. The signal selection is discussed in section 5.2.

In section 5.3, possible EFT effects on signal and background events are discussed. The observable sensitive to EFT effects and a parameterisation of these effects is also presented.

5.1 Signal and backgrounds

To illustrate the different contributions from different processes, the distribution of the reconstructed top p_{T} and mass, after the signal selection as explained later, are shown in fig. 5.14. This section discusses the signal and background processes and how the background processes mimic the signal signature.

5.1.1 The t-channel process

In fig. 5.1 a single top quark produced in the t-channel is depicted. The top quark decays to a W-boson and b-quark. The W-boson subsequently decays either hadronically or leptonically. This analysis is restricted to signatures of t-channel events with W decays to an electron or a muon, which are well identifiable in the detector. The final state is further characterised by large missing transverse energy from the neutrino and two high energetic jets. One of these two jets is a b-jet, while the other jet is a light-flavour jet usually with high pseudorapidity. A candidate t-channel event display recorded by the ATLAS detector in Run 2 is shown in fig. 5.2.

The t-channel process is modelled using MC methods. The SM hard scattering process is modelled with POWHEG at NLO accuracy in QCD up until stable top

quarks[44, 45, 83–87]. The top quarks are decayed using MADSPIN to preserve spin correlations[54, 88]. The PS and hadronisation of the produced particles is performed with PYTHIA.

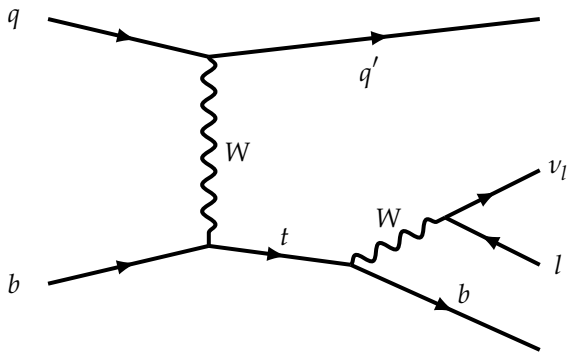

Figure 5.1: The Feynman diagram of t-channel single top production with a top quark decaying in a b-quark and a W-boson. The W-boson decays leptonically.

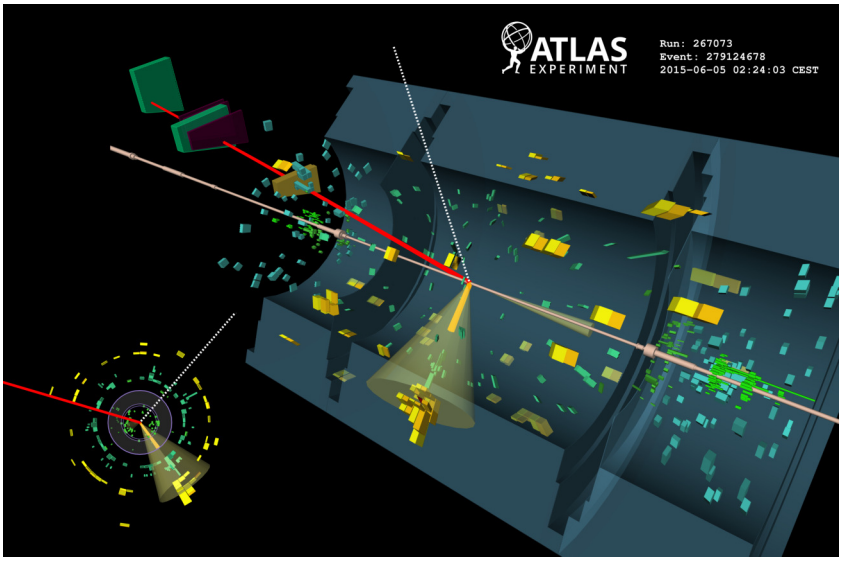

Figure 5.2: Event display of a t-channel single top event candidate, recorded by the ATLAS detector on 4 June 2015 in a 13 TeV run. The red line shows a muon. The cone in the middle is the b-jet candidate while the very forward cone shows the light-flavour jet candidate. The dashed line indicates the missing transverse energy in the event. Taken from [89].

5.1.2 Top backgrounds

Top pair production

One of the main backgrounds in this analysis is the $t\bar{t}$ process. When one of the top quarks decays leptonically, producing a muon or electron while the other top quark decays hadronically, the signature only differs from the t-channel by the number of (b-) quarks in the final state. There are several possibilities how this final state can mimic the t-channel process due to finite detector resolution and acceptance. For instance, when jets overlap and one b-jet is not identified, a $t\bar{t}$ event is wrongly classified as a t-channel event. Although this does not occur very frequent, due to the high cross-section of the $t\bar{t}$ process, a relatively large contribution of events are still selected in the analysis as shown in fig. 5.14.

The $t\bar{t}$ process is modelled with the same tools as the t-channel process. POWHEG is used to simulate the SM hard scattering process with undecayed top quarks at NLO accuracy in QCD. The produced top quarks are decayed at LO accuracy using MADSPIN. The produced particles are interfaced with PYTHIA to simulate the PS and the hadronisation. Recently, predictions of top pair production have been calculated with NNLO precision in QCD, including electroweak corrections at NLO [90]. Hence, a small correction to the modelling has been applied to match the top quark p_{T} distribution at this higher order.

The probability that a small fraction of the $t\bar{t}$ events mimic the signal, depends on non-perturbative QCD radiation and subtle instrumental effects. Therefore, the normalisation of the falsely selected $t\bar{t}$ event is eventually obtained from the data itself as will be explained later.

Other single top production modes

Relatively small background contributions involve top quarks originating from the tW and s-channel process, see fig. 2.4 the upper right and lower Feynman diagram. These are simulated with NLO accuracy in QCD. As there is an overlap between the tW process at NLO and the $t\bar{t}$ process, particular care has to be taken to not double count the processes [91]. This is done by removing certain diagrams from the ME calculation of the tW process, referred to as the diagram removal (dR) scheme. An alternative method is to subtract the contribution of the double counted processes from the tW processes which is called the diagram subtraction (dS) scheme. The performance of these methods, and more details, can be found in [92].

Backgrounds from rare top processes

Processes with (a) top quark(s) produced in association with (a) gauge boson(s) or a Higgs boson lead to relatively small background contributions. Processes of this type, considered in this analysis are: $t\bar{t}Z$, $t\bar{t}W$, $t\bar{t}H$, tZq, tHq and tWZ. Also three and four quark production processes are considered. They are, apart from $t\bar{t}H$, simulated with aMC@NLO and showered using PYTHIA. The $t\bar{t}H$ process uses POWHEG to generate the hard scattering process. They are all produced with NLO accuracy in

QCD. The produced top quarks and W/Z-boson are decayed using MADSPIN.

5.1.3 Electroweak processes

W-boson with associated jet production

Events with a W-boson and additional jets constitute a relatively large background to this analysis. Unlike, the background discussed above, these events do not contain a genuine top quark. Nevertheless, when the W-boson decays leptonically and additional light-jets and b-jets are produced, the detectable state closely resembles the t-channel process. Note that usually the b-quarks are produced in pairs, while one b-jet is required for the signal. Still, one b-jet can escape detection or the jets overlap, leading to a single b-jet.

There is also a significant contribution from jets originating from c-quarks that are (wrongly) identified as b-jets. All these effects occur with small probability, but convoluted with the large cross-section, this background is relatively large.

The matrix element of the W+jets process is simulated with SHERPA at NLO for up to two jets and at LO for three to five jets. They are consequently showered and hadronised also within SHERPA. To avoid double counting different jet multiplicities, they are merged using the CKKW matching procedure [93, 94].

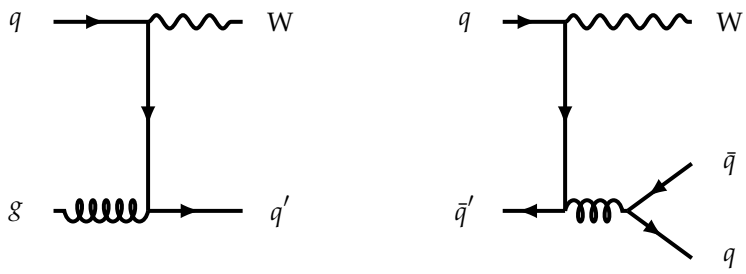

Figure 5.3: Two example Feynman diagram of W+jets production with one (left) and two (right) additional jets.

Z-boson and multi boson production

Smaller background contributions originate from the production of a Z-boson-boson in association with quarks or from diboson production (labelled as VV). They are simulated in a similar way as the W+jets process using SHERPA for the ME calculation, the showering and the hadronisation.

Higgs boson production

A small contribution is expected from Higgs boson production in the gluon fusion (ggF), the vector boson fusion (VBF) and the VH production modes. They are estimated using MC methods. POWHEG and PYTHIA are used for the gluon fusion and VBF processes. PYTHIA is used to model the VH production.

5.1.4 Fake background

Events with muons or electrons not produced at the hard scattering interaction but originating from soft processes are referred to as "fake" leptons. This background includes events where a jet is misidentified as an electron or a muon is produced in the decay of a heavy flavour quark. This background contribution is difficult to estimate from MC predictions. It is therefore estimated using a data-driven method called the matrix method [95]. This method uses weighted events from data. These weights are estimated from a region with relaxed lepton criteria. The fake background is strongly reduced by event selection criteria, but taken into account throughout the analysis.

5.2 Event selection

Selection criteria are applied on reconstructed event properties to create a purified signal region. The largest backgrounds are the $t\bar{t}$ and W+jets backgrounds. Dedicated regions are constructed to measure the EFT coefficients simultaneously with the normalisation of $t\bar{t}$ and W+jets in a data-driven approach. The selection criteria for the signal and control regions are explained in the following. A flowchart of the event selection and categorisation is shown in fig. 5.9.

5.2.1 Pre-selection requirements

Events are required to pass an initial selection, called the pre-selection, which is mainly designed to reduce the fake background. If an event fulfils these requirements it will fall in the so-called pre-selection region.

Events need to be triggered on one of the lowest not pre-scaled[1] triggers for electrons or muons. They are listed in table 5.1. Events need to fulfil the transverse momentum requirements and the identification requirement after the HLT reconstruction [96, 97].

Triggered events are required to have exactly 1 charged Tight lepton with $p_{\mathrm{T}} > 30\,\mathrm{GeV}$ and $|\eta| < 2.5$ with a veto on a secondary low-p_{T} charged Loose lepton ($p_{\mathrm{T}} > 10\,\mathrm{GeV}$ and $|\eta| < 2.5$) and have exactly two jets, with at least on of these jets being b-tagged.

[1] A pre-scaled trigger discards a fraction of the events at random.

Table 5.1.: Un-prescaled single-lepton trigger selections of the ATLAS trigger menu per lepton flavour per year. These single-lepton triggers are combined using a logical OR.

Year	Single-electron trigger	Single-muon trigger
2015	HLT_e24_lhmedium_L1EM20VH HLT_e60_lhmedium HLT_e120_lhloose	HLT_mu20_iloose_L1MU15 HLT_mu50
2016–2018	HLT_e26_lhtight_nod0_ivarloose HLT_e60_lhmedium_nod0 HLT_e140_lhloose_nod0	HLT_mu26_ivarmedium HLT_mu50

Furthermore, there is a requirement on the transverse mass of the W-boson, $m_{\mathrm{T}}(\ell E_{\mathrm{T}}^{\mathrm{miss}})>60\,\mathrm{GeV}$. The transverse mass is obtained from the transverse momenta of the lepton and $E_{\mathrm{T}}^{\mathrm{miss}}$. In fig. 5.4, the distribution of $m_{\mathrm{T}}(\ell E_{\mathrm{T}}^{\mathrm{miss}})$ before the final selection is shown, to illustrate the level of the initial background. Only systematic uncertainties affecting the fake background are shown. The uncertainty on the other processes is of the order of 5-10%, indicating that the modelling of the background processes is consistent with data, even for events with low transverse mass. To further reduce backgrounds, the $E_{\mathrm{T}}^{\mathrm{miss}}$ is additionally required to be larger than 35 GeV. This is to ensure that there is a large amount of missing momentum which is associated with the neutrino.

Lastly a cut on the lepton (l) p_{T} depending on the azimuthal difference with the jet with highest transverse momentum (*leadjet*), is applied as follows:

$$p_{\mathrm{T}}(l) > 50(1 - \frac{\pi - \Delta\phi(l, leadjet)}{\pi - 1})\ \mathrm{GeV}. \tag{5.1}$$

A two-dimensional distribution of the lepton transverse momentum versus $\Delta\phi(l, leadjet)$ is shown in fig. 5.5 for t-channel events on the left and for the fake background on the right. This selection criterion removes the fake events populating the upper left region, while keeping a significant amount of t-channel events.

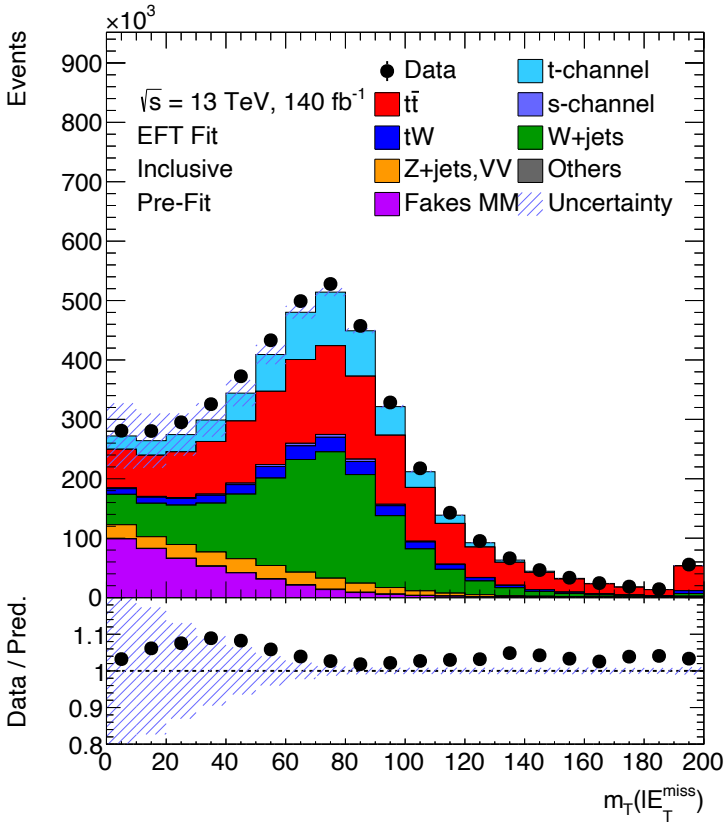

Figure 5.4: Distribution of $m_{\mathrm{T}}(\ell E_{\mathrm{T}}^{\mathrm{miss}})$ for the different expected processes stacked upon each other as well as the data (dots). An intermediate stage of the selection, based only on the number of leptons, number of jets and number of b-tagged jets is applied, see text. The uncertainty band only includes systematic effects from fake backgrounds.

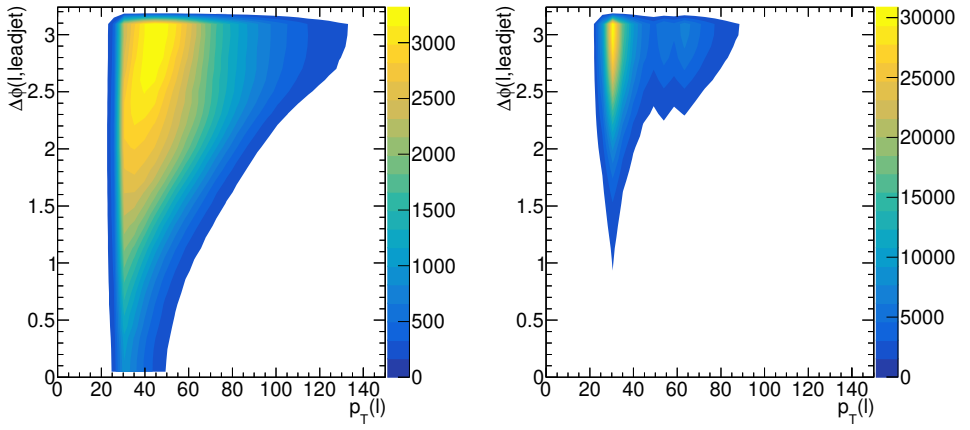

Figure 5.5: Distribution of the transverse momentum of the lepton, $p_T(lepton)$, versus the azimuthal angle between the jet with the highest momentum and the lepton, $\Delta\phi$(l,leadjet), for t-channel events on the left and for fake background on the right.

5.2.2 The $t\bar{t}$ and W+jets control regions

Events that pass these selection criteria are further categorised. A $t\bar{t}$ enriched region is constructed, where both jets are tagged as a b-jet. This region is defined to constrain the $t\bar{t}$ normalisation from data. Events with one tagged b-jet and one non b-tagged jet are further divided into a signal region and a control region for the W+jets background. Events in the W+jets control region are all events that fail any of the final selection requirements described in the next section.

5.2.3 Final selection requirements

In fig. 5.6 a distribution of m_{lb} is shown for events which pass the pre-selection criteria and have one tagged b-jet and one non b-tagged jet. The contribution of the different processes is shown stacked upon each-other. The data is shown as black dots. The uncertainty band includes all systematic uncertainties which are discussed in more detail in the next chapter. The expectations agree well with the data within their uncertainty. The backgrounds still can be significantly reduced to obtain a pure signal region as will be explained in the following.

The first requirement is that the invariant mass of the lepton b-jet system, $m_{\ell b}$, must be smaller than 153 GeV. This selection reduces the background contribution substantially while keeping most of the signal, as is clear from the distribution of $m_{\ell b}$. The reconstructed mass of the $m_{\ell E_T^{\text{miss}} b}$system is required to have a value between 120.6 and 234.6 GeV. This criterion is used to select events that have a mass which is around the top quark mass.

In addition, a requirement is set on the invariant mass of the reconstructed top quark

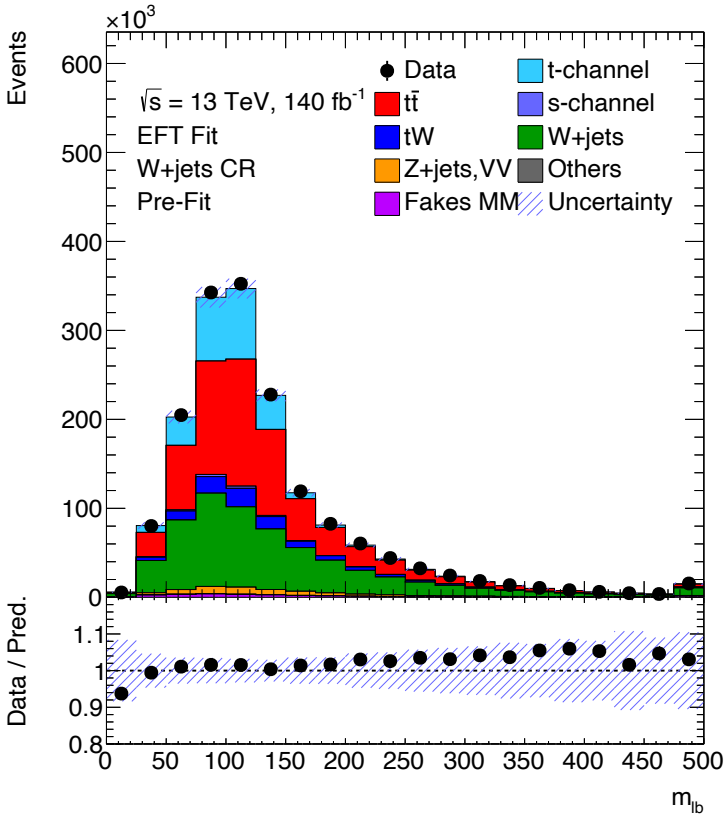

Figure 5.6: Distribution of m_{lb} for events surviving the pre-selection criteria and have only 1 b-tagged jet. The contributions for the different processes are stacked upon each other. The black dots represent the data. The uncertainties explained in section 6.2 are taken into account and shown as the grey band. The lower panel corresponds to the ratio between data and prediction.

and the spectator jet, $m_{jlE_{\mathrm{T}}^{\mathrm{miss}}b}$. Since in t-channel events the angle between these two particles is expected to be large, only events with $m_{jlE_{\mathrm{T}}^{\mathrm{miss}}b}$ larger than 320 GeV are selected. Also H_{T}, which is the scalar sum of the transverse energies of the b-jet, the light-jet, the lepton and $E_{\mathrm{T}}^{\mathrm{miss}}$, is required to be larger than 190 GeV.

Trapezoidal requirement

Lastly the selected events in the signal region have to fulfil a trapezoidal requirement defined as:

$$\begin{aligned}
&\eta_j < \left(a_1 \eta_{l E_{\mathrm{T}}^{\mathrm{miss}} b} + b_1\right) \,\&\\
&\eta_j > \left(a_1 \eta_{l E_{\mathrm{T}}^{\mathrm{miss}} b} - b_1\right) \,\&\\
&(\eta_j > \left(a_2 \eta_{l E_{\mathrm{T}}^{\mathrm{miss}} b} + b_2\right) \,||\\
&\eta_j < \left(a_2 \eta_{l E_{\mathrm{T}}^{\mathrm{miss}} b} - b_2\right))
\end{aligned} \tag{5.2}$$

In this equation $a_{1/2}$ and $b_{1/2}$ have been optimised for having a large S/B, and simultaneously have a large $S/\sqrt{S+B}$. The values used are: $a_1 = 3$, $b_1 = 10.5$, $a_2 = 0.25$ and $b_2 = 2.5$. The two-dimensional distribution of the pseudorapidity of the top quark versus the pseudorapidity of the jet is shown for different processes in fig. 5.7. The upper left plot shows the distribution for t-channel events, the upper right for the sum of all backgrounds. In the bottom left picture the distribution for $t\bar{t}$ is shown and on the bottom right for W+jets. The black lines show the trapezoidal requirement, where jets with a central top and a forward jet are kept. The double peak structure of the distribution for t-channel is expected as the spectator quark originates commonly, but not always, from a valence quark while the top quark originates from a sea quark. This means that the spectator quark has in general large longitudinal momentum, while the top quark has a low longitudinal momentum and is thus more central. This cut greatly reduces the number of background events, in particular for $t\bar{t}$ events. Events that fulfil all these requirements are selected in the signal region (SR).

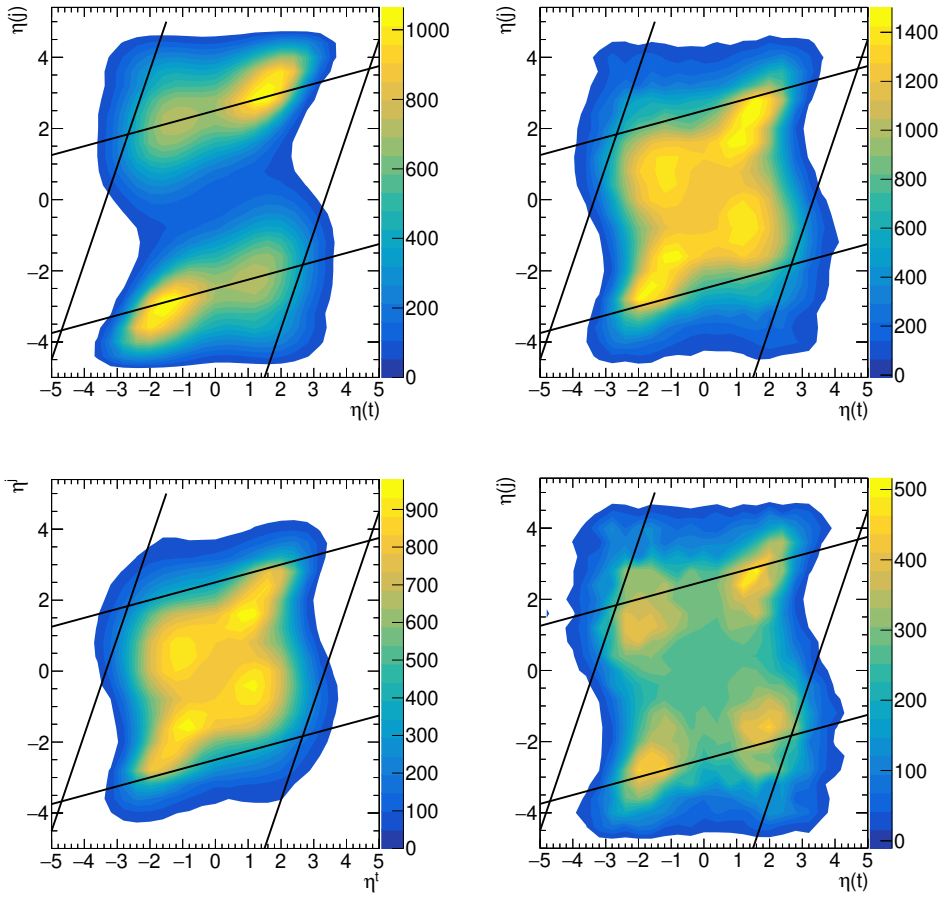

Figure 5.7: Distribution of the pseudorapidity of the top quark versus the pseudorapidity of the spectator jet for events with 1 b-jet and 1 light-jet that survived the pre-selection criteria. The upper left the plot shows the distribution for signal events and the upper right for the combination of all backgrounds. The bottom left shows the distribution for the $t\bar{t}$ background while the bottom left shows the distribution for W+jets. The black lines show the trapezoidal requirements as explained in the text.

The KLFit likelihood requirement for the Signal Region

In fig. 5.8 the distribution of the logarithm of the KLFit likelihood, $\ln(L)$, is shown for events that enter the SR. The plot shows the number of expected events for each different process stacked upon each other as well as the data in black points. The shaded band shows the systematic uncertainty in each bin. The systematic sources are explained in more detail in section 6.2. SR events are required to have $\ln(L) > -36$, which enriches the purity of t-channel events. Furthermore, as discussed in chapter section 4.4.3, wrongly reconstructed t-channel events are also rejected by this cut.

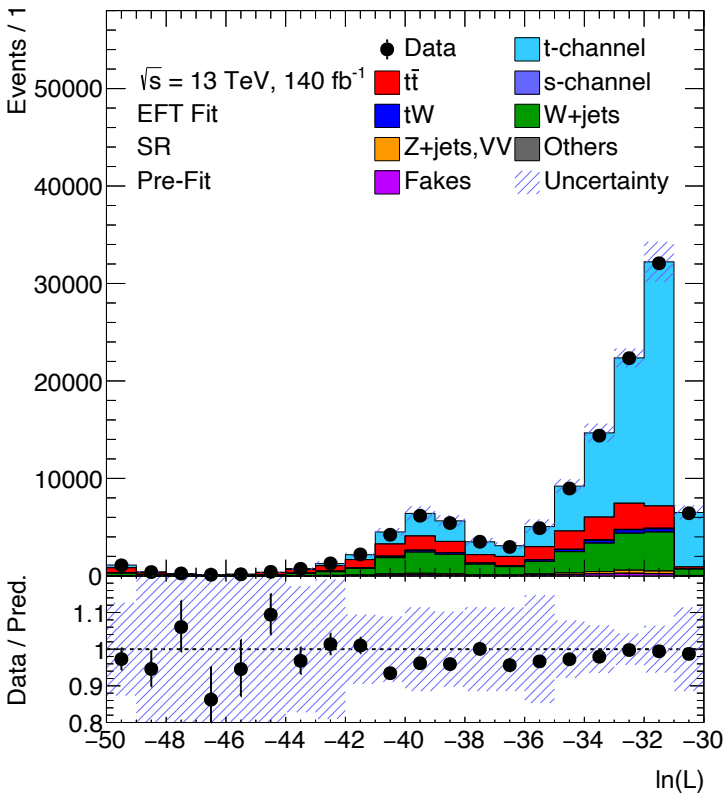

Figure 5.8: Distribution of the logarithm of the likelihood, $\ln(L)$, after the kinematic fit in the Signal Region. The contributions for the different processes are stacked upon each other. The black dots represent the data. The uncertainties explained in section 6.2 are taken into account and shown as the grey band. The lower panel corresponds to the ratio between data and prediction.

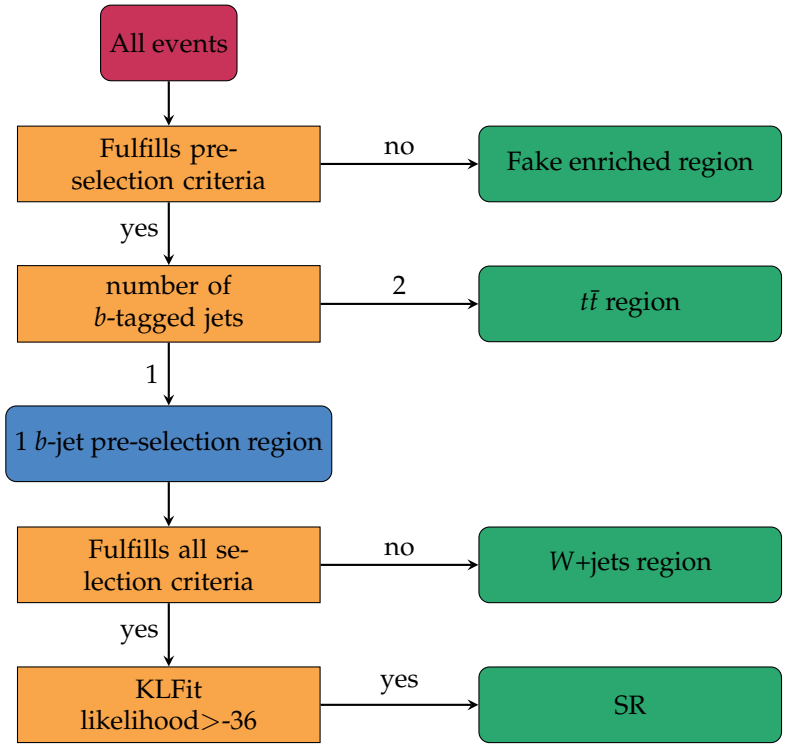

Figure 5.9: Flowchart describing the event selection and categorisation of events.

5.2.4 Event distributions

This section presents the distribution of reconstructed event quantities in the SR to further validate the modelling and simulation of different processes. In appendix C these distributions are shown in the $t\bar{t}$ and W+jets CR.

The first set of kinematic variables shown are the transverse momentum and pseudorapidity of the lepton, b-jet and light-jet. In fig. 5.10 the lepton transverse momentum (left) and pseudorapidity (right) are shown. The b-jet transverse momentum (left) and pseudorapidity (right) are shown in fig. 5.11 and the transverse momentum (left) and pseudorapidity (right) of the light-jet are shown in fig. 5.12. Lastly the missing transverse energy of the event is shown in fig. 5.13. In these distributions the SM expectation for t-channel events is stacked on top of the expectation from all the backgrounds. The data is shown with black points. The lower panel of each plot corresponds to the ratio between data and prediction. The uncertainties explained in section 6.2 are taken into account and shown as the grey band. In the final fit the normalisation of the t-channel, $t\bar{t}$ and W+jets process are left freely floating as will be explained in more detail in chapter 6. This is not accounted for in these plots. The prediction of the background and signal modelling agrees very well with the data, and is well within the uncertainties band for all variables. A small trend is observed for the jet momentum but is covered by the systematic uncertainty.

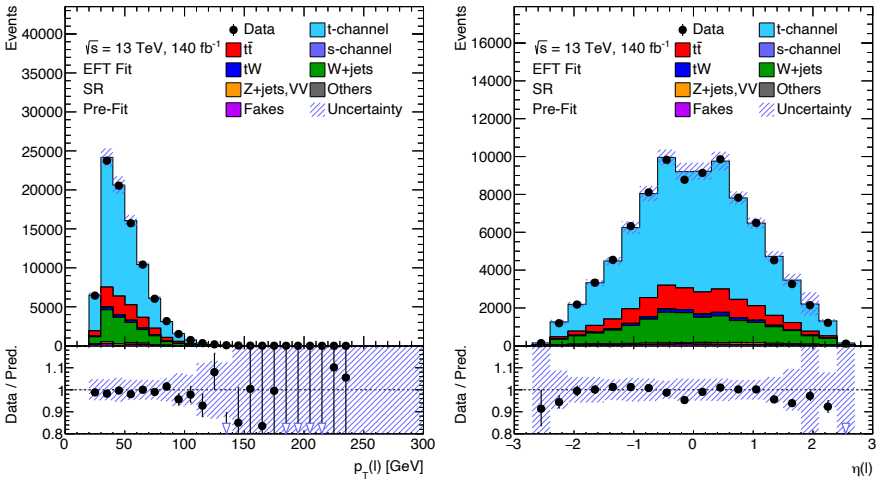

Figure 5.10: Distribution of the lepton p_{T} (left) and pseudorapidity (right) for events in the signal region. For the different processes, the contributions are stacked upon each other. The black dots represent the data. The uncertainties explained in section 6.2 are taken into account and shown as the grey band. The lower panels correspond to the ratio between data and prediction.

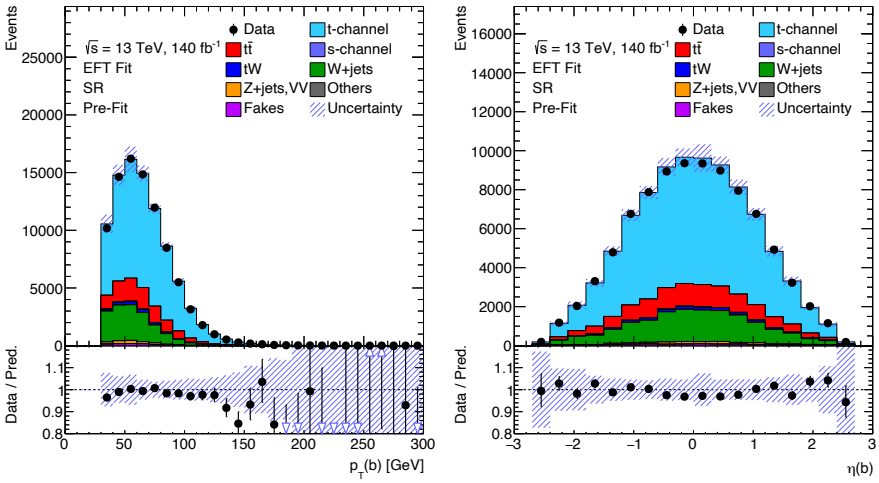

Figure 5.11: Distribution of the b-jet p_{T} (left) and pseudorapidity (right) for events in the signal region. The contributions for the different processes are stacked upon each other. The black dots represent the data. The uncertainties explained in section 6.2 are taken into account and shown as the grey band. The lower panels correspond to the ratio between data and prediction.

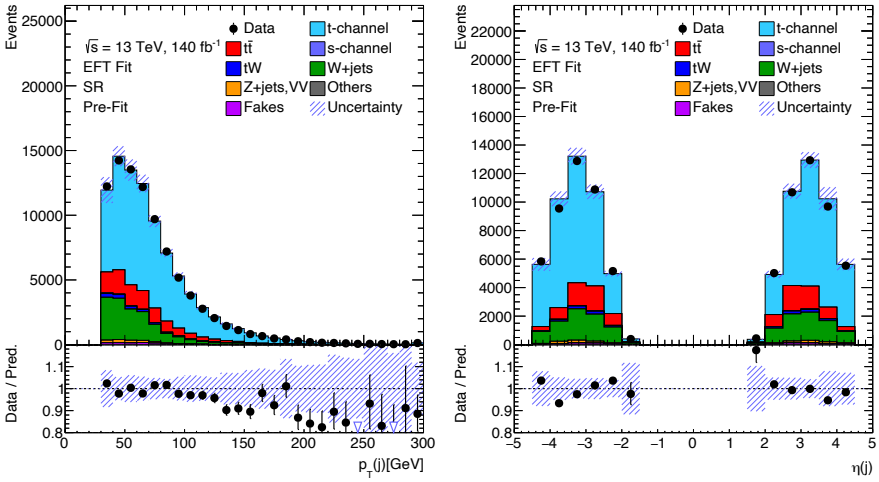

Figure 5.12: Distribution of the light-jet p_{T} (left) and pseudorapidity (right) for events in the signal region. The contributions for the different processes are stacked upon each other. The black dots represent the data. The uncertainties explained in section 6.2 are taken into account and shown as the grey band. The lower panels correspond to the ratio between data and prediction.

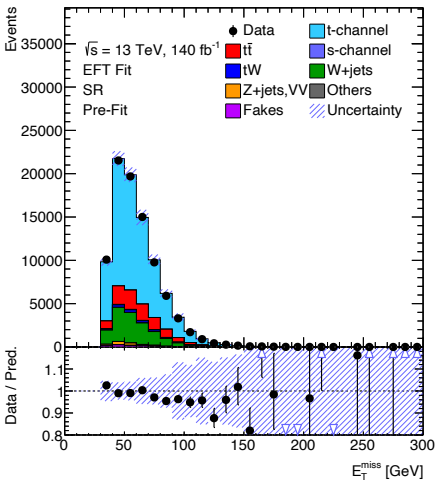

Figure 5.13: Distribution of missing transverse energy for events in the signal region. The contributions for the different processes are stacked upon each other. The black dots represent the data. The uncertainties explained in section 6.2 are taken into account and shown as the grey band. The lower panels correspond to the ratio between data and prediction.

The reconstructed top quark transverse momentum (left) and mass (right) are shown in fig. 5.14. The reconstruction of the top kinematic distribution depends on the correct modelling and reconstruction of all the final state particles. The predictions agree with the data within uncertainty. A small slope is observed in the top p_{T} spectrum, which is however within uncertainties.

Lastly the three polarisation angles are shown in the SR in fig. 5.15. The distribution for $\cos\theta_{\ell x}$ is shown in the upper left panel, $\cos\theta_{\ell y}$ is shown in the upper right panel and $\cos\theta_{\ell z}$ is shown in the bottom panel. These three angular distributions, together with the top p_{T} spectrum are the main input of the analysis presented in the next chapter. Below, the EFT dependence of these quantities is discussed.

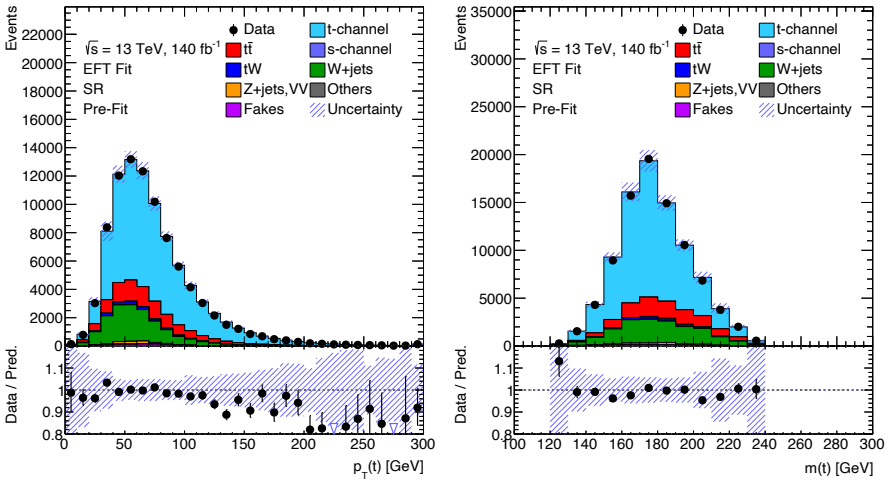

Figure 5.14: Distribution of the transverse momentum of the top p_{T}(t) (left) and its invariant mass m_t (right) for events in the signal region. The contributions for the different processes are stacked upon each other The black dots represent the data. The uncertainties explained in section 6.2 are taken into account and shown as the grey band. The lower panel of each plot corresponds to the ratio between data and prediction.

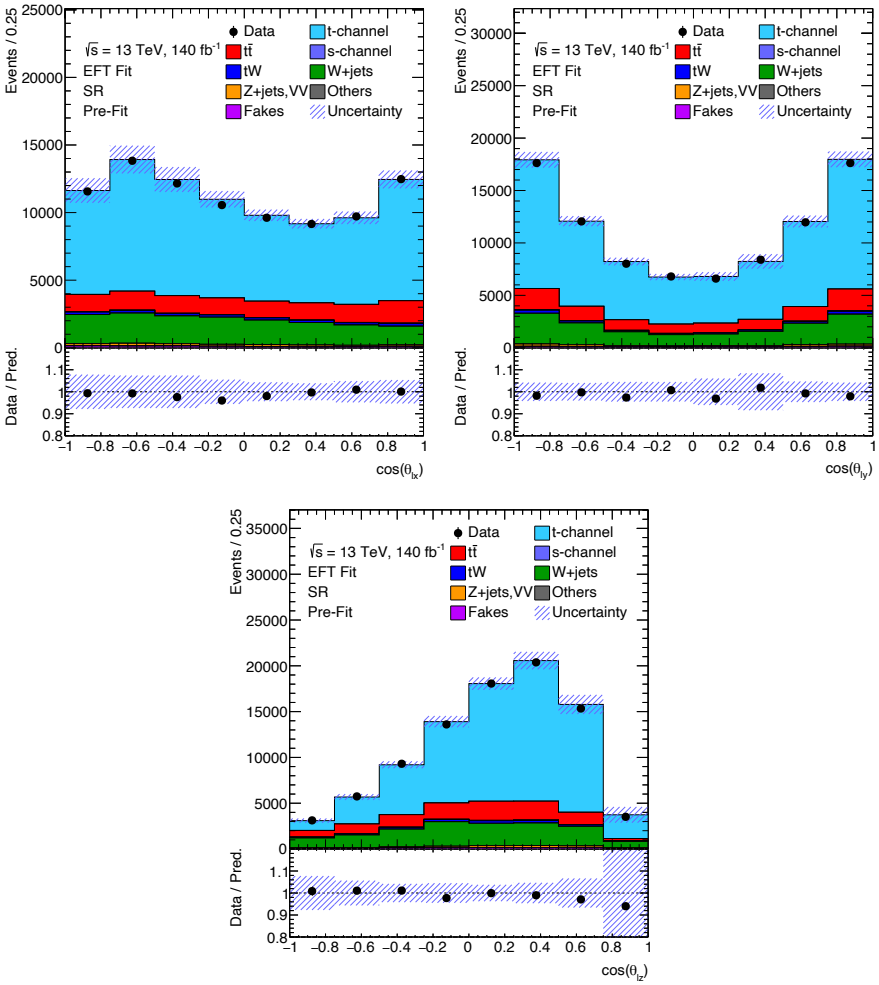

Figure 5.15: Distribution of $\cos\theta_{\ell x}$ (upper left), $\cos\theta_{\ell y}$ (upper right) and $\cos\theta_{\ell z}$ (bottom) for events in the signal region. The contributions for the different processes are stacked upon each other. The black dots represent the data. The uncertainties explained in section 6.2 are taken into account and shown as the grey band. The lower panel of each plot corresponds to the ratio between data and prediction.

5.3 The EFT dependency

5.3.1 Modelling of EFT effects

The aMC@NLO generator is used to study the effects of EFT operators on proton-proton collisions. In this analysis, the dim-6 top model [98] is exploited. To limit the number of possible new EFT operators, several assumptions are made. In this model the EFT operators modify the three lepton generations simultaneously and thus no distinction is made between the corresponding Wilson coefficients. The same approach is adopted for the first two generations of quarks, while the third generation with the top and bottom quark acquire their own set of Wilson coefficients.

Several predictions for a plethora of EFT points are needed to parameterise the dependence of the Wilson coefficients. Instead of generating several different MC samples, each with its own showering and full detector simulation, a different approach is used. This approach uses the reweighting procedure of the aMC@NLO generator with LO accuracy. This method uses only one fully simulated sample.

The simulation provides for each simulated event a weight, which corresponds to its cross-section. The reweighting method uses this original weight to calculate a new weight for each event for different model assumptions, i.e. different values for the Wilson coefficients. This new weight is obtained from:

$$W_{new} = \frac{\mid M^{new} \mid^2}{\mid M^{old} \mid^2} W_{old}. \tag{5.3}$$

Here W_{old} is the weight of the original calculation and M^{new} (M^{old}) is the matrix element of the new (original) model. The original calculation uses the SM expectation and the new model has non-zero EFT Wilson coefficients.

In total there is a plethora of different EFT values created with the reweighting method. For c_{tW} these values are [-3,-2,0,2,3]. The values for c_{itW} are [-1.5,-1,0,1,1.5] and for c_{qQ} the values are [-3,0,3]. Insertions of two EFT coefficients at the same time are also considered however combinations of $c_{tW} = \pm 3$ and $c_{itW} = \pm 1.5$ are not generated to limit computing resources.

There are two challenges when using the reweighting technique.

Firstly the procedure recomputes the partial decay width while keeping the total decay width of the top quark constant. Consequently, the width always equals the SM value in the calculation of the cross-section and the branching ratio in eq. (2.23) is incorrect as the numerator is affected by EFT effects while the denominator is kept constant. This has a negligible effect on the predicted shapes of distributions, however the overall normalisation is affected. In this analysis a correction on the normalisation is applied for each reweighted EFT point i. This correction, w^i_Γ, is

defined as:

$$w_{\Gamma}^{i} = \frac{\Gamma_{SM}(t)}{\Gamma_{EFT}^{i}(t)}. \tag{5.4}$$

Here $\Gamma_{EFT}^{i}(t)$ is calculated using the dim-6 model in aMC@NLO and $\Gamma^{SM}(t)$ is set to 1.48 GeV.

The second challenge is that large weights can occur for an event from a region where the original model has a small cross-section and where the new model predicts an enhanced cross-section. Hence, large event weights create large fluctuations in the distributions and enlarge the uncertainty due to limited statistics of the sample. Therefore, after the procedure, the event weights are checked to avoid unstable results.

5.3.2 The EFT sensitive observable

Observables with a high sensitivity to EFT coefficients c_{tW} and c_{itW} are the polarisation angles $\cos\theta_{\ell x}$, $\cos\theta_{\ell y}$ and $\cos\theta_{\ell z}$ as explained in section 2.2.1. In fig. 5.16 the sensitivity of $\cos\theta_{\ell x}$ on c_{tW} and c_{itW} is illustrated. Coefficient c_{tW} creates an asymmetry around a zero value of $\cos\theta_{\ell x}$ as is clear from fig. 5.16 (left). Fig. 5.16 (right) shows that c_{itW} does not alter this distribution.

The dependence of $\cos\theta_{\ell y}$ on c_{tW} is shown in fig. 5.17 (left) and is fairly modest. In contrast, the effect of c_{itW}, see fig. 5.17 (right), leads to a significant asymmetry. This is indeed expected as c_{itW} corresponds to a CP-violating interaction, while $\cos\theta_{\ell y}$ is the CP-odd observable. Fig. 5.18 shows the sensitivity of $\cos\theta_{\ell z}$, which is related to the spin polarisation of the top quark. The effects of c_{tW} can be seen in fig. 5.18 (left). This coefficient modifies the slope of the $\cos\theta_{\ell z}$ distribution. This is expected as O_{tW} leads to top quarks with right-handed chirality. The effect of c_{itW} is relatively small as shown in fig. 5.18 (right).

The 4-fermion operator $O_{qQ}^{3,1}$ has no effect on the angular observables. Instead, it modifies the cross section as function of the energy scale of the hard subprocess. Therefore, the p_{T} of the top quark is a sensitive observable to extract c_{qQ}. A distribution of the top quark p_{T} for the SM and for $c_{qQ} = \pm 3$ is shown in fig. 5.19. The effect on the cross-section of c_{qQ} is large, but in this analysis we restrict to the shape of the top p_{T} distribution, specifically the ratio between events at relatively low and high transverse momentum. This also implies that this measurement is insenstive to operator $c_{\phi Q}$. An analysis that extracts c_{qQ} and $c_{\phi Q}$ from the cross-section is published here [99].

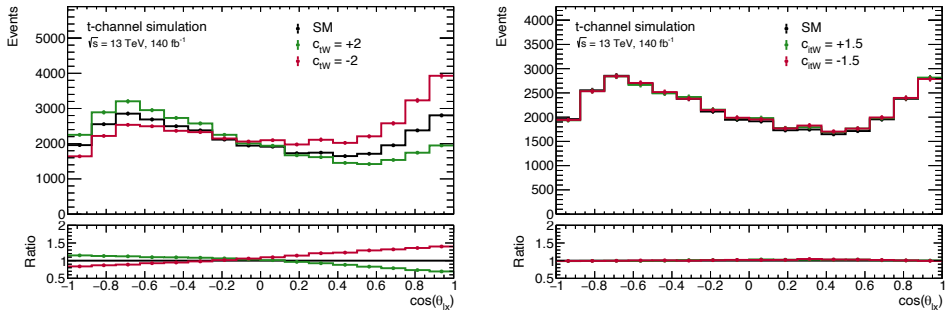

Figure 5.16: Dependency of $\cos\theta_{\ell x}$ on c_{tW} (left) and c_{itW} (right). The lower panels show the ratio with respect to the SM.

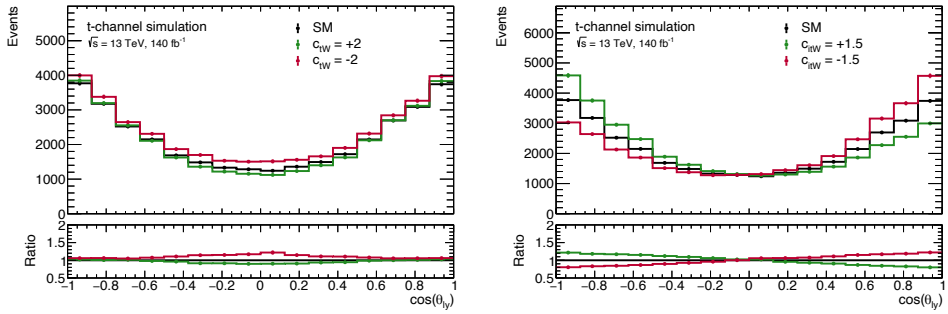

Figure 5.17: Dependency of $\cos\theta_{\ell y}$ on c_{tW} (left) and c_{itW} (right). The lower panels show the ratio with respect to the SM.

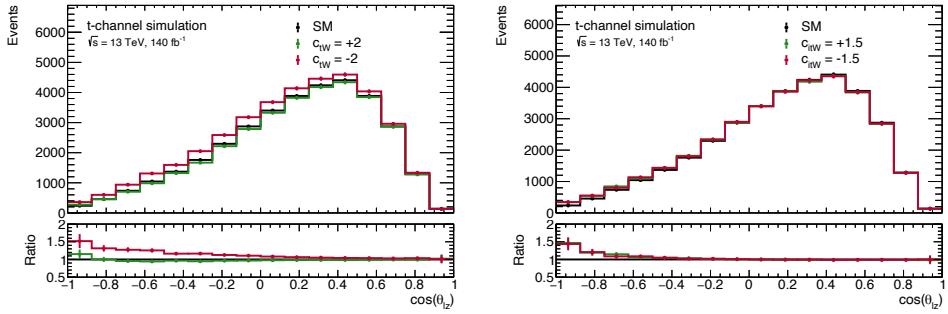

Figure 5.18: Dependency of $\cos\theta_{\ell z}$ on c_{tW} (left) and c_{itW} (right). The lower panels show the ratio with respect to the SM.

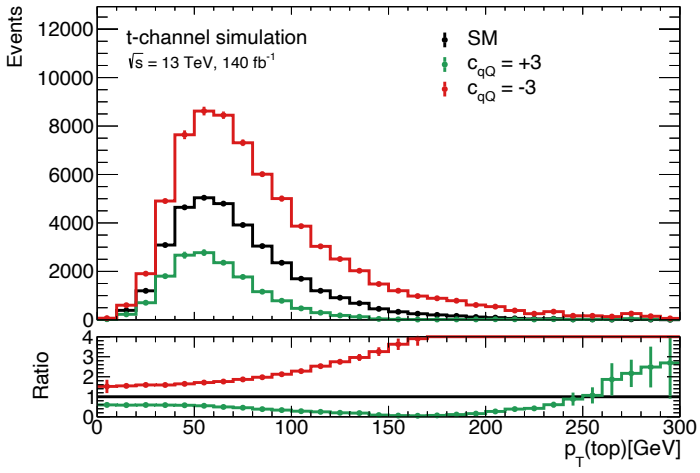

Figure 5.19: Dependency of the top quark p_{T} on operator c_{qQ}. The lower panel shows the ratio with respect to the SM.

The final observable

To frame all the information in a single (multidimensional) distribution with a reasonable number of bins is not straightforward. However, the asymmetries of the angular distributions contain most information of EFT operators. Hence, the signs of the polarisation angles $\cos\theta_{\ell x}$, $\cos\theta_{\ell y}$ and $\cos\theta_{\ell z}$, thus 2 bins per angle, contain the sensitivity to the Wilson coefficients. The p_{T} distribution of the top quark is also divided in two bins, $p_{\mathrm{T}}(\mathrm{top}) < 80\,\mathrm{GeV}$ and $p_{\mathrm{T}}(\mathrm{top}) > 80\,\mathrm{GeV}$ respectively. The bins of the angular observables and the top p_{T} distribution are now combined into a single observable O(16) with $2^4 = 16$ statistically independent bins. The *bin* number is given by:

$$\begin{aligned} bin(O(16)) = &(\cos\theta_{\ell y} > 0) \\ &+ 2(\cos\theta_{\ell x} > 0) \\ &+ 4(\cos\theta_{\ell z} > 0) \\ &+ 8(p_{\mathrm{T}}(\mathrm{top}) > 80\,\mathrm{GeV}). \end{aligned} \tag{5.5}$$

Distributions for several EFT scenarios are shown in fig. 5.20. In the top plot the dependency on c_{tW} is displayed, in the middle the dependency on c_{itW} and in the bottom the dependency on c_{qQ} is shown. The effect of each Wilson coefficient corresponds to a specific change in O(16). The effect of c_{qQ} can be easily recognised: the first 8 bins exhibit a different behaviour than the last 8 bins. For the EFT coefficients there is another feature that increases the sensitivity. As can be seen in these plots, differences are enhanced for the last 8 bins which correspond to events with large transverse momentum of the top. This is due to two reasons, firstly events with higher momentum are reconstructed with higher precision. Secondly they have a larger energy exchange, which increases the sensitivity on the EFT coefficients.

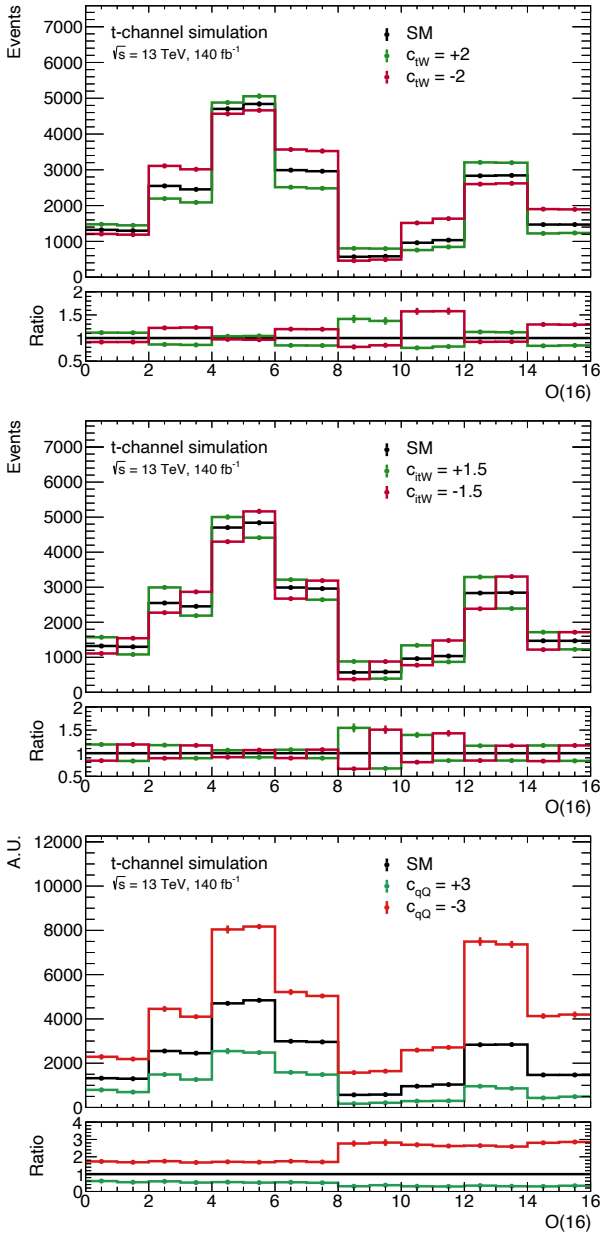

Figure 5.20: Dependency of the observable $O(16)$ as defined in eq. (5.5) on c_{tW} (top), c_{itW} (middle) and c_{qQ} (bottom). The lower panel shows the ratio with respect to the SM.

5.3.3 EFT parameterisation of t-channel events

This analsysis uses a likelihood function to extract the Wilson coefficients from the O(16) observable. Therefore, the predicted number of events in each bin of O(16) has to be parameterised as function of these Wilson coefficients. To obtain this parameterisation, predictions in each bin are produced for multiple values of EFT coefficients. The procedure is explained in more detail in the following for the SR. The two control regions also have an EFT dependency, and are parameterised in a similar way.

The predictions for the three EFT coefficients c_{tW}, c_{itW}, c_{qQ} are obtained via the reweighting method explained in section section 5.3.1. The expectations are divided by the LO SM prediction and multiplied by the NLO prediction of the SM.

Using these predictions, a quadratic function depending on the EFT coefficients is fitted for each bin separately. The form of this function is:

$$N_{EFT}(c_{tW}, c_{itW}, c_{qQ}) = \left[1 + \sum_{x=c_{tW},c_{itW},c_{qQ}} a_x \cdot c_x + \sum_{x,y=c_{tW},c_{itW},c_{qQ}} b_{x,y} \cdot c_x \cdot c_y\right] N_{SM}. \tag{5.6}$$

The first sum incorporates the linear dependence on the EFT coefficient c_x and the second sum expresses the quadratic dependence, where EFT cross-terms are allowed. Since the quadratic terms are suppressed by Λ^{-4} in the expansion of the squared matrix element, they are expected to be smaller than the linear terms.

Figure 5.21 shows for each bin of O(16) its dependence on c_{tW} (top row), c_{itW} (middle row) and c_{qQ} (bottom row). The horizontal axis shows the value of the plotted EFT coefficient and the vertical axis the relative change with respect to the SM. The black points are estimated from points where only the indicated EFT coefficient is varied, and the other parameters constant. The grey points are EFT samples where multiple EFT coefficients are varied. The quadratic functions are plotted in red curves for the particular EFT coefficient and describes the EFT points well. This demonstrates that the EFT effect retains a quadratic functional form, even after detector simulation and event selection. In table 5.2 the value of each term is listed.

Table 5.2.: EFT parameterisation for t-channel in each bin for each term of eq. (5.6).

bin	1.0	c_{tW}	c_{tW}^2	$c_{tW}c_{itW}$	$c_{tW}c_{qQ}$	c_{itW}	c_{itW}^2	$c_{itW}c_{qQ}$	c_{qQ}	c_{qQ}^2
SR_bin0	1.00	0.05	0.01	0.00	-0.01	0.11	0.01	-0.01	-0.19	0.02
SR_bin1	1.00	0.05	0.01	-0.00	-0.01	-0.12	0.01	0.01	-0.19	0.01
SR_bin2	1.00	-0.09	0.01	0.00	0.01	0.09	0.01	-0.01	-0.19	0.02
SR_bin3	1.00	-0.09	0.01	-0.00	0.01	-0.09	0.01	0.01	-0.19	0.03
SR_bin4	1.00	0.02	0.00	-0.00	0.00	0.05	-0.00	-0.01	-0.19	0.01
SR_bin5	1.00	0.02	0.00	0.00	0.00	-0.05	-0.00	0.01	-0.19	0.01
SR_bin6	1.00	-0.09	0.00	-0.00	0.01	0.06	-0.00	-0.01	-0.20	0.01
SR_bin7	1.00	-0.09	0.00	0.00	0.01	-0.06	-0.00	0.01	-0.20	0.01
SR_bin8	1.00	0.15	0.03	0.02	-0.05	0.29	0.04	-0.07	-0.40	0.06
SR_bin9	1.00	0.13	0.03	-0.01	-0.04	-0.27	0.03	0.07	-0.40	0.06
SR_bin10	1.00	-0.19	0.04	0.01	0.04	0.19	0.05	-0.04	-0.40	0.06
SR_bin11	1.00	-0.19	0.05	-0.00	0.04	-0.19	0.06	0.05	-0.39	0.05
SR_bin12	1.00	0.05	0.01	-0.00	-0.01	0.11	0.00	-0.02	-0.38	0.05
SR_bin13	1.00	0.05	0.01	0.00	-0.01	-0.11	0.00	0.02	-0.38	0.07
SR_bin14	1.00	-0.11	0.01	0.00	0.03	0.11	0.01	-0.03	-0.42	0.06
SR_bin15	1.00	-0.11	0.02	-0.00	0.03	-0.11	0.00	0.03	-0.42	0.06
ASR	1.00	-0.01	0.02	-0.00	0.00	0.00	0.01	0.00	-0.35	0.17
$t\bar{t}$	1.00	-0.02	0.01	0.00	0.00	0.00	0.01	-0.00	-0.17	0.14

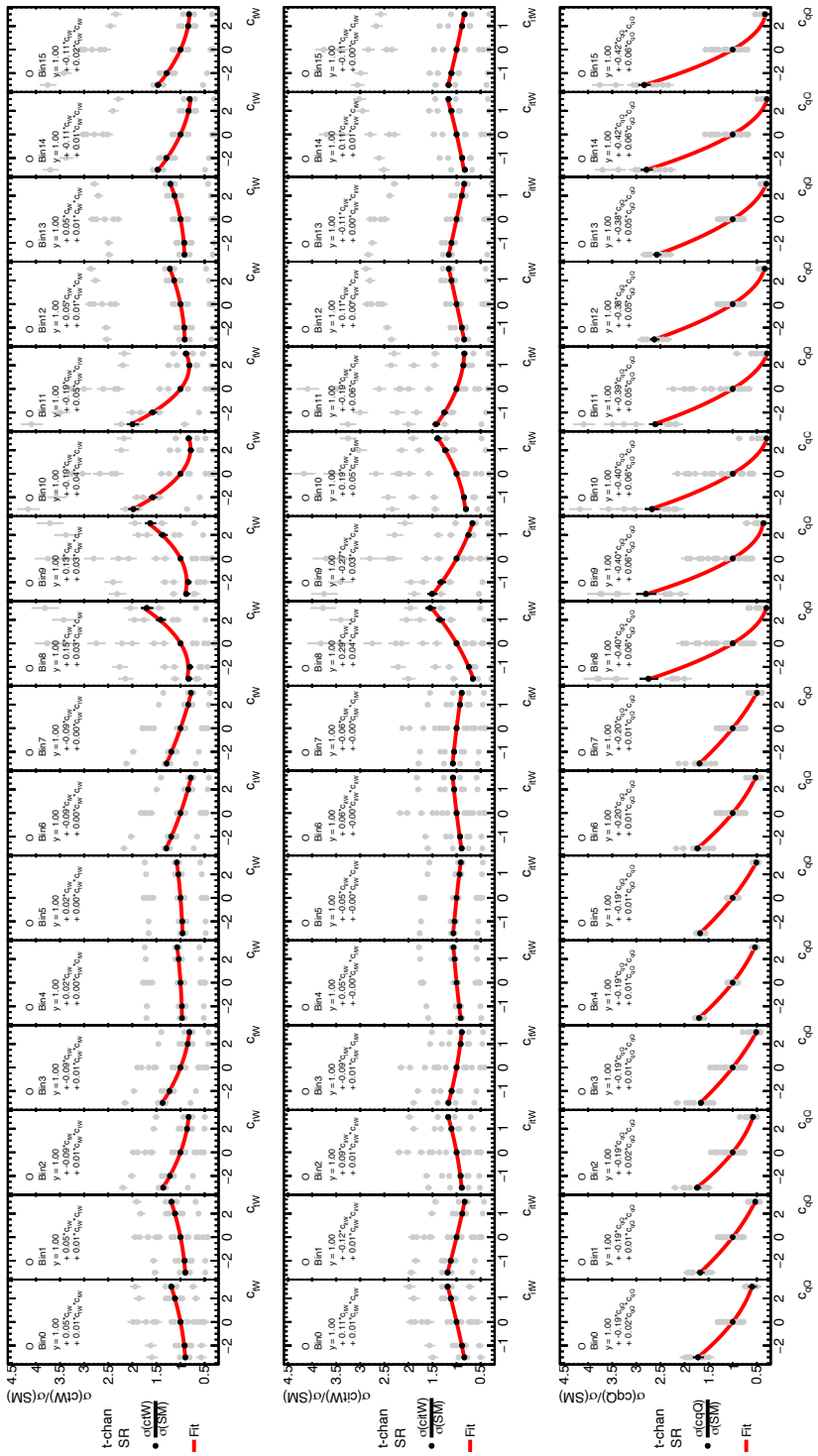

Figure 5.21: The dependence of O(16) on c_{tW} (top row) and c_{qQ} (bottom row), for the t-channel single top process in the signal region. Each panel in a row, corresponds to a bin of O(16). The curves represent the parametrisation of the EFT effects, see text.

5.3.4 EFT parameterisation of the $t\bar{t}$ background

In previous analyses, a common assumption was that only the signal, e.g. the t-channel single top process, can be affected by "new" physics interactions. In contrast, in the EFT approach, the SM prediction is modified by additional operators which are not limited to a single process. Therefore, in general, the background predictions also need to take EFT effects into account. Since this analysis focuses on EFT operators involving top processes, only the $t\bar{t}$ background needs to be modified. The other backgrounds are considered to be Standard Model.

To parameterise the $t\bar{t}$ background as function of EFT coefficients the same approach is followed as for the t-channel process. However now only c_{tW} and c_{itW} are expressed by EFT coefficients, since c_{qQ} does not affect the $t\bar{t}$ process and the effect of c_{qQ} on the top decay is considered to be negligible.

Figure 5.22, 5.23 and 5.24 show the normalised distributions from the $t\bar{t}$ sample for $\cos\theta_{\ell x}$, $\cos\theta_{\ell y}$ and $\cos\theta_{\ell z}$ respectively. The effects for different values of c_{tW} (left plot) and c_{itW} (right plot) are also displayed. Small asymmetries are introced by the EFT operators on $\cos\theta_{\ell x}$ and $\cos\theta_{\ell z}$ in the opposite direction for $t\bar{t}$ as for t-channel. There is practically no effect from c_{itW} on these distributions. The EFT dependency of the O(16) observable is shown in fig. 5.25. The effect appears to be modest and within the statistical uncertainty due to limited number of simulated events.

In table 5.3 the final parameterisation is summarised. A very small dependence of the cross-section is observed for both c_{tW} and c_{qQ}.

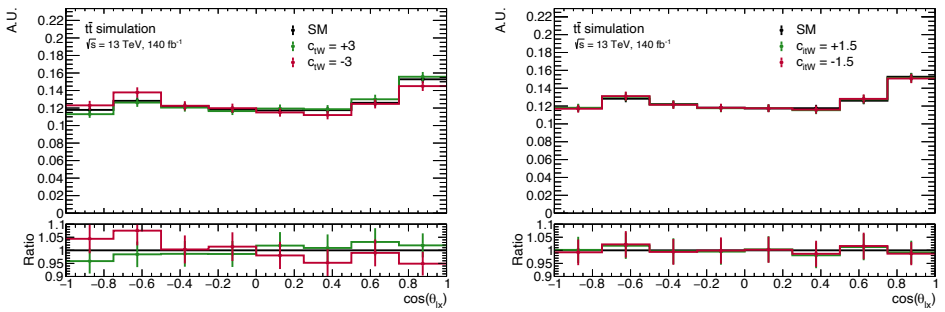

Figure 5.22: Dependency of $\cos\theta_{\ell x}$ on c_{tW} (left) and c_{itW} (right) for the $t\bar{t}$ process. The lower panels show the ratio with respect to the SM.

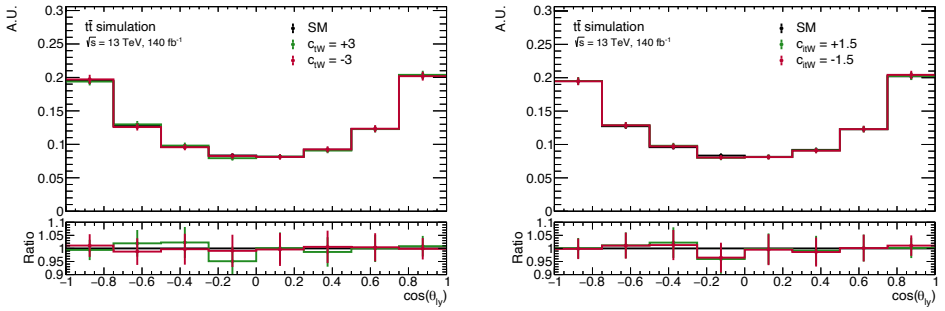

Figure 5.23: Dependency of $\cos\theta_{\ell y}$ on c_{tW} (left) and c_{itW} (right) for the $t\bar{t}$ process. The lower panels show the ratio with respect to the SM.

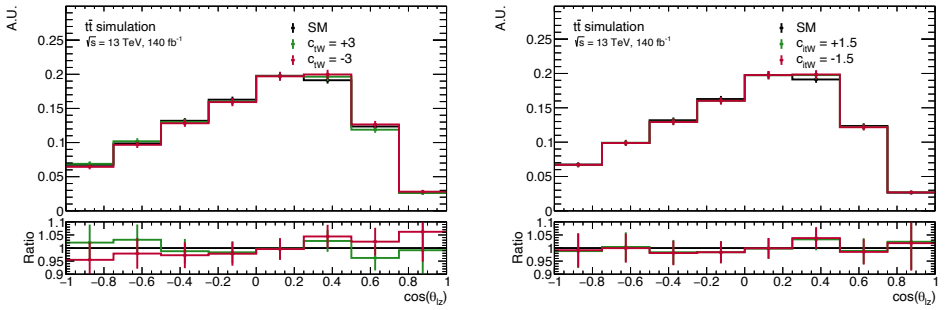

Figure 5.24: Dependency of $\cos\theta_{\ell z}$ on c_{tW} (left) and c_{itW} (right) for the $t\bar{t}$ process. The lower panels show the ratio with respect to the SM.

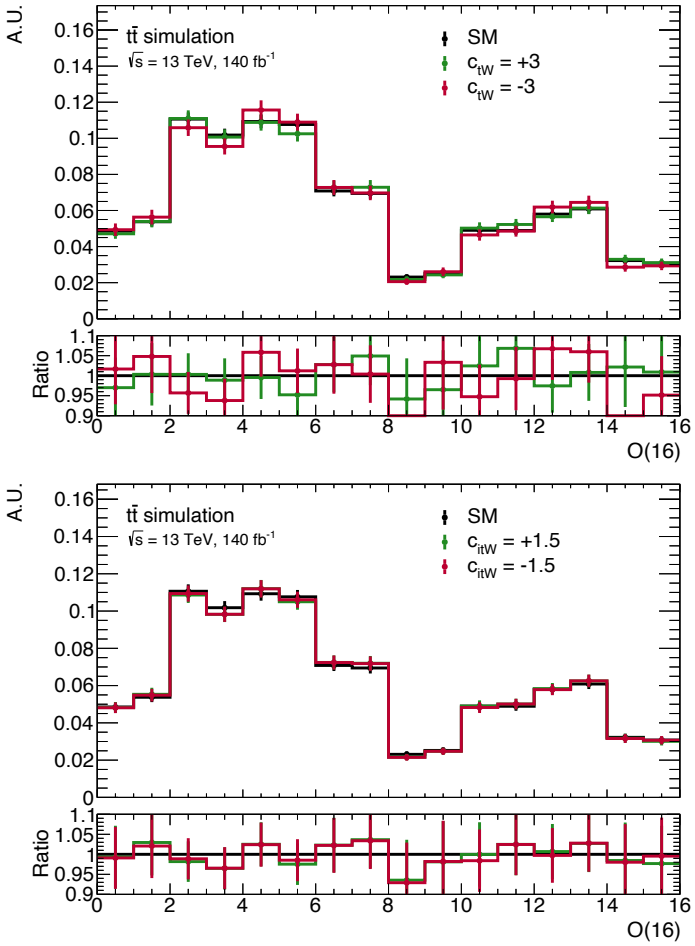

Figure 5.25: Dependency of O(16) on c_{tW} (top) and c_{itW} (bottom) for the $t\bar{t}$ process. The lower panels show the ratio with respect to the SM.

Table 5.3.: EFT parameterisation for $t\bar{t}$ in each bin for each term of eq. (5.6).

bin	1.0	$\mathbf{c_{tW}}$	$\mathbf{c_{tW}^2}$	$\mathbf{c_{tW}c_{itW}}$	$\mathbf{c_{itW}}$	$\mathbf{c_{itW}^2}$
SR_bin0	0.99	-0.01	-0.01	-0.00	0.00	-0.03
SR_bin1	1.00	-0.01	-0.01	-0.00	0.00	-0.02
SR_bin2	0.99	0.00	-0.01	0.00	-0.00	-0.03
SR_bin3	0.99	0.00	-0.01	0.00	-0.00	-0.04
SR_bin4	1.00	-0.02	-0.01	0.00	-0.00	-0.02
SR_bin5	0.99	-0.02	-0.01	0.00	-0.00	-0.03
SR_bin6	1.00	-0.01	-0.01	-0.00	0.00	-0.02
SR_bin7	1.00	0.00	-0.01	0.00	0.00	-0.02
SR_bin8	0.99	0.00	-0.02	-0.00	0.00	-0.05
SR_bin9	0.99	-0.02	-0.01	0.00	-0.00	-0.03
SR_bin10	0.99	0.01	-0.01	-0.00	0.01	-0.03
SR_bin11	1.00	0.01	-0.01	0.00	-0.00	-0.02
SR_bin12	1.00	-0.02	-0.01	-0.00	0.00	-0.03
SR_bin13	1.00	-0.01	-0.01	0.00	-0.00	-0.02
SR_bin14	0.99	0.01	-0.02	0.00	0.00	-0.03
SR_bin15	0.99	0.00	-0.01	0.00	-0.01	-0.03
ASR	1.00	-0.01	-0.01	-0.00	0.00	-0.02
$t\bar{t}$	1.00	0.00	-0.01	-0.00	0.00	-0.03

Chapter 6

Measurement of the EFT Wilson coefficients

This chapter presents the measurent of the EFT Wilson coefficients. First the statistical method in this measurement is explained. This is followed by a discussion of the systematic uncertainties affecting this analysis. Lastly the results are presented and discussed.

6.1 Statistical inference

To perform a quantitative analysis of the possible contribution of EFT operators a likelihood[1] based approach is performed. Since the number of events in each bin, for each region is measured, each individual bin can be seen as an independent counting experiment, which follows a Poisson distribution. Hence, the likelihood for measuring the event count in a certain bin, i, is given by:

$$L_i(\vec{D}|\vec{\mu},\vec{c}_w) = \frac{[\mu_s S_i(\vec{c}_w) + \mu_b^x B_i^x]^{D_i}}{D_i!} \exp[-\mu_s S_i(\vec{c}_w) - \mu_b^x B_i^x]. \tag{6.1}$$

In this formula S_i is the number of expected signal events, which depends on the EFT coefficients, $\vec{c}_w = \{c_{tW}, c_{itW}, c_{qQ}\}$, as described in section 5.3.3. In a similar way the expected number of events for a certain background x is denoted by B_i^x. The background, $B_i^{t\bar{t}}$, from $t\bar{t}$ also depends on the EFT coefficients. The number of events, observed in data is given by D_i. The parameter $\vec{\mu}$ is a vector of normalisation factors for t-channel, denoted by $\mu_{t-\text{channel}}$ and for the backgrounds, μ_b^x, with one normalisation factor for $t\bar{t}$, $\mu_{t\bar{t}}$ and $\mu_{W+\text{jets}}$ for the W+jets background.

The measurement is affected by uncertainties from several systematic sources. For these systematic uncertainties, the expected number of signal and background events are parameterised by a set of nuisance parameters $\vec{\theta}$. These change the number of events for the signal and for each background sample separately. For each bin of each sample, the number of events generically denoted by N_i is then given by:

$$N_i = N_i \cdot (1 + \sum_{j=1}^{m} \begin{cases} \theta_j \cdot \Delta_{i,j}^{UP} & \text{if } \theta_j \geq 0 \\ \theta_j \cdot \Delta_{i,j}^{DOWN} & \text{if } \theta_j < 0 \end{cases}). \tag{6.2}$$

[1] Here the likelihood method is exploited to extract the EFT coefficients from data, which should not be confused with the likelihood method applied in KLFit described in section 4.4, used to reject poorly reconstructed events.

Where $\Delta_{i,j}^{UP}$ is the expected one standard (1-sigma) upwards deviation of systematic j in bin i and $\Delta_{i,j}^{DOWN}$ is its corresponding downwards deviation. The sources of systematic uncertainties are described in detail in section 6.2.

Since the systematic uncertainties are estimated in subsidiary measurements an additional constraint term is added to the likelihood for each nuisance parameter. This is a Gaussian likelihood term, G, with a mean value of 0, and a width of unity. The complete likelihood can thus be parameterised in the following way:

$$L(\vec{D}|\vec{\mu},\vec{c}_w,\vec{\theta}) = \prod_{i=1}^{n} L_i(\vec{D}|\vec{\mu},\vec{c}_w,\vec{\theta}) \cdot \prod_{j=1}^{m} G(0|\theta_j,1). \tag{6.3}$$

To find the value of the EFT parameters that are most compatible with the data, the likelihood function has to be maximised. To find these values in practice, for numerical stability, the negative logarithm of this likelihood function is minimised and the profile likelihood ratio q is defined by:

$$q(\vec{c}_w) = -2\ln(\lambda) = -2\ln\frac{\left(L(\vec{D}|\hat{\hat{\vec{\mu}}}(\vec{c}_w),\vec{c}_w,\hat{\hat{\vec{\theta}}}(\vec{c}_w))\right)}{\left(L(\vec{D}|\hat{\vec{\mu}},\hat{\vec{c}}_w,\hat{\vec{\theta}})\right)}. \tag{6.4}$$

In this equation the denominator $L(\vec{D}|\hat{\vec{\mu}},\hat{\vec{c}}_w,\hat{\vec{\theta}})$ is where the "log-likelihood" is maximised for all parameters of $\vec{\mu},\vec{c}_w$ and $\vec{\theta}$ which is indicated with a $\hat{}$ above the parameter. The numerator is the maximised log-likelihood for a given value of EFT coefficients $\vec{c}_w$ with respect to $\vec{\mu}$ and $\vec{\theta}$ indicated by the double $\hat{\hat{}}$ symbol. The one-dimensional 1-sigma interval is found by the value where $q(\vec{c}_w)$ has increased to +1 for one EFT parameter, while refitting all the other parameters, including the other EFT parameters. This method is referred to as "profile likelihood fit".

6.2 Sources of uncertainties

Systematic effects are categorised in two types of uncertainties. The first type corresponds to experimental uncertainties related to detector performance effects, in particular the reconstruction and identification of physics objects. The second type originates from the uncertainties on theoretical modelling of the signal and background processes. These are referred to as theoretical uncertainties and include uncertainties from the calculation of cross-sections, as well as assumptions made in the simulation of these processes. Both types of systematic uncertainties are discussed in the following.

6.2.1 Experimental uncertainties

Experimental uncertainties are estimated in dedicated measurements to obtain a lower and upper bound, the $\pm 1\sigma$ effect, around the nominal value of a parameter or shape of a distribution. The impact of each systematic source individually is evaluated by setting the values in the estimation to their $\pm 1\sigma$ values and used in the fitting method as explained above. As will turn out later, the main experimental uncertainties for the analysis are from the reconstruction of jets.

Luminosity and pile-up uncertainties

The luminosity for the full Run 2 is measured at a central value of $140\,\text{fb}^{-1}$ with an uncertainty of 0.83 % [100]. This uncertainty is applied to each MC simulated process. MC simulated processes are reweighted to match the observed distribution of the average number of interactions per bunch-crossing. The pile-up uncertainty is estimated by changing this reweight factor by 4 % [101]. The contribution of these sources on the measurement of the Wilson coefficients is very small.

Lepton uncertainties

Systematic uncertainties on the momentum scale, momentum resolution, identification and isolation corrections of electrons and muons are applied [73, 74]. Additionally, an uncertainty on the trigger efficiencies is taken into account [96, 97]. The uncertainties on electrons and muons have only a very small impact on the precision of the analysis.

Jet uncertainties

Since the spectator jet is used as reference axis to define the polarisation angles and the b-jet is needed to reconstruct the top quark, uncertainties on the jets are of great importance for the analysis.

Uncertainties affecting jets that are considered in this analysis are related to the jet energy scale (JES), the jet energy resolution (JER) [77] and the identification efficiencies of the jets.

The JES uncertainty is parameterised by 30 nuisance parameters, i.e. independent sources of systematic uncertainties. These incorporate effects on the theoretical modelling used to extract the energy scale corrections, detector component effects, a factor taken into account the effect of pile-up and nuisance parameters for the inter- and extrapolation of the JES between momentum and pseudorapidity regions. Furthermore terms affecting the flavour composition of jets are considered. These terms account for the effect that a jet which is initiated by a light quark has a different response than a jet initiated by a gluon. As the fraction of jets that originate from which type of particles is a priori unknown, an additional flavour composition uncertainty is applied. The fraction of jets originating from gluons is set to 50 % in the nominal setup. As upwards uncertainty a 100 % gluon fraction is applied and the down uncertainty is a gluon fraction of 0 %. This gluon fraction is specific per pro-

cess, therefore an individual nuisance parameter changing this fraction separately for each process is used. For instance, the gluon fraction in t-channel events is expected to be smaller, as most jets originate from the spectator quark produced in the hard scattering event and the b-quark from the top decay. In fig. 6.1 the distribution of the O(16) variable in the SR is shown for the up (down) variation in red (blue) for the flavour composition uncertainty. The shape is very similar to the effect that c_{tW} would have, limiting the precision of this EFT parameter. Effects from the JES uncertainty are of the order of 1 to 5 % percent.

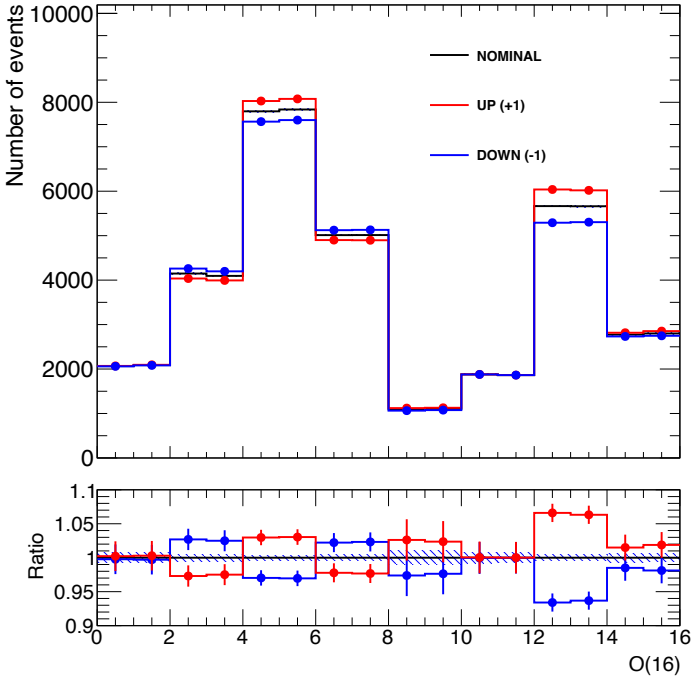

Figure 6.1: The impact on the O(16) observable from the JES flavour composition uncertainty of the t-channel process.

For the JER a total of 13 nuisance parameters is considered. Twelve effective modelling components and one component that takes into account the difference between data and MC. The uncertainty from the JER is obtained from the difference between the measured resolutions in data and in MC.

The effect is implemented by 'smearing' the jet p_{T} in MC using a scale factor generated from a Gaussian shape with the appropriate width to account for the JER uncertainty. As jets cannot be under-smeared the resulting uncertainty is one-sided. The effect on the p_{T} is of the order of 1.5 % for jets with a momentum of 20 GeV to 0.5 % percent for a jet with a momentum of 300 GeV. If the JER is larger in MC with respect to data the MC can not be further smeared to match data. In this case an additional uncertainty is added to cover the difference in resolution from data and

MC.

Additional uncertainties on the tagging of jets are considered. These include differences in the efficiency of the flavour tagging and the tagging of pile-up jets by the (f)JVT algorithms. The total uncertainty on the tagging efficiency of b-jets is of the order of 10 %. The uncertainty on the (f)JVT efficiency is a few percent.

Missing Transverse Energy

Systematic effects changing the measured objects also affect the $E_{\mathrm{T}}^{\mathrm{miss}}$ calculation. This is propagated to the $E_{\mathrm{T}}^{\mathrm{miss}}$ by recalculating it, using the physics object with the systematic shift applied. As the calculation of the $E_{\mathrm{T}}^{\mathrm{miss}}$ also has a soft-track component an additional uncertainty for this component is taken into account [79, 80].

6.2.2 Modelling uncertainties

Uncertainties that originate from the simulation of the different processes using MC techniques are referred to as modelling uncertainties. Several assumptions in the calculations of the hard scattering and the showering are made to generate events for the most accurate prediction of the processes. To evaluate the uncertainty on the baseline predictions, alternative generators are used and the (single-sided) difference with the nominal distributions is taken as the +1σ effect. The -1σ effect is estimated by mirroring the effect.

Uncertainties on the t-channel modelling

The uncertainty of the choice of μ_R and μ_F are estimated by doubling/halving their value in the MC generation. This should cover the uncertainty from the value of the different scales used in the MC generation. One nuisance parameter is included to cover the uncertainty from the tune of the generation. Furthermore, choices of the PDF are accounted for by including 30 nuisance parameters using the eigenvector decomposition of the PDF4LHC recommendations [102]. To account for differences in the showering of the process, the nominal sample created with PYTHIA is compared to a MC sample where the events are showered with HERWIG. This uncertainty covers the difference between a momentum ordered showering algorithm (PYTHIA) and the angular ordered algorithm (HERWIG).

The uncertainty from the matching of the hard-scattering process with the shower is estimated by changing internal settings in PYTHIA, referred to as pthard [103, 104]. This changes the definition of the momentum scale of the emission from that calculated by POWHEG to the transverse momentum of the POWHEG emitted parton relative to all other partons in the event. Since POWHEG vetoes additional emissions of partons from PYTHIA depending on the scale, this affects whether additional emissions are modelled by the PYTHIA showering algorithm or are already covered by NLO emissions in the POWHEG event generation. Fig. 6.2 shows the effect on the O(16) observable for this systematic source.

Across the board, the effect on O(16) seems to be small. However the ratio, which is

also shown, reveals a correlated effect: the first 8 bins (mostly) go down, while the last 8 bins go up and vice versa. This systematic effect leads to an asymmetry in the top p_{T}, which resembles the effect of EFT coefficient c_{qQ}.

It would not be reasonable to assume that this effect is correlated among all kinematic regions. Therefore, the effects are conservatively split to four kinematic domains, introducing four new nuisance parameters. Two of these nuisance parameters affect the t-channel SR in the low and high momentum bins respectively. The two remaining nuisance parameters affect the two control regions.

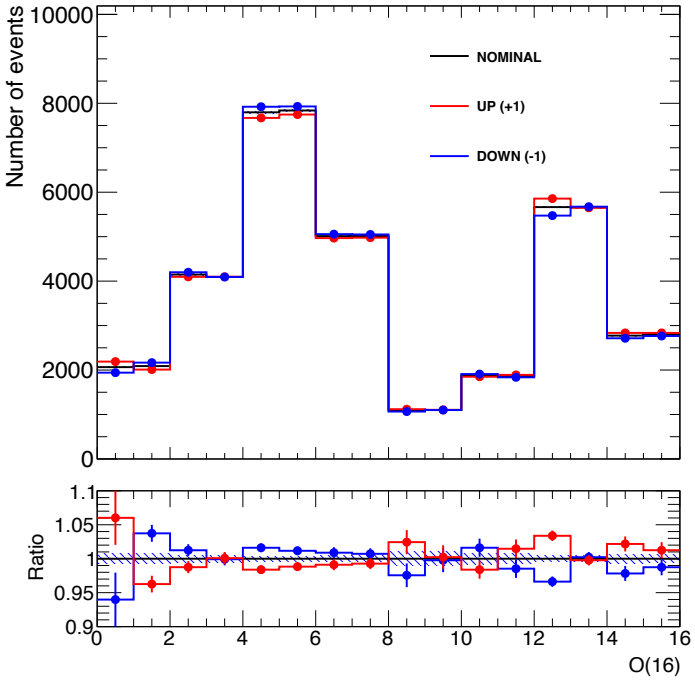

Figure 6.2: Systematic effect from the p_{T} hard matching uncertainty on the t-channel signal. The black line shows the nominal prediction. The red line shows the $+1\sigma$ deviation, which is mirrored to get the uncertainty for -1σ shown by the blue line.

Lastly an uncertainty on the top mass is considered, changing the value by $\pm 0.5\,\mathrm{GeV}$ in the generation of the signal sample.

Uncertainties on the background modelling

The modelling uncertainties of the $t\bar{t}$, tW and s-channel process are similar to the t-channel process. The uncertainties are taken as uncorrelated with the t-channel uncertainties. Additionally, uncertainties on the NNLO reweighting of the $t\bar{t}$ process are considered. The pthard uncertainties on tW and s-channel are not available

yet, the effect from matching is estimated by comparing the POWHEG sample to a MC generated with aMC@NLO. Additionally, an uncertainty on the tW process is applied to estimate the difference between the diagram subtraction and diagram removal scheme to deal with the overlap with top pair production. A 5 % uncertainty on the cross section of the tW and s-channel processes is taken into account. The cross-section of the $t\bar{t}$ process, i.c. the normalisation of the sample, is left freely floating in the fit. As the $t\bar{t}$ process is one of the main backgrounds, uncertainties on this processes have potentially a large impact on the final result.

Uncertainties on the W+jets channel are considered via the scaling of μ_r and μ_f. PDF uncertainties are also taken into account. The total cross-section of the W+jets process is left freely floating. To take into account differences in flavour composition of W+b-jets and W+c-jets an additional uncertainty is added by scaling the W+c-jets contribution up (down) by 10 % while simultaneously scaling the number of W+b-jets down (up) to keep the same total event count.

For all the smaller backgrounds uncertainties affecting the total normalisation of the process are applied.

Uncertainties due to the limited size of the MC samples are taken into account. This is done using the Beeston-Barlow [105] technique, allowing a process to be scaled in a certain bin within the uncertainty of the MC statistical component. This is done by so-called γ-parameters. In each bin a γ-parameter scales the event counts within a Poissonian likelihood constraint. This is done separately for the t-channel, $t\bar{t}$, W+b-jets and W+c-jets templates. Lastly one set of gamma parameters changes the sum of all the other backgrounds.

6.3 Fit results

This section presents the fit results on the EFT parameters c_{tW}, c_{itW} and c_{qQ}. Moreover, the correlations between these parameters, as well as the systematic uncertainties and normalisation factors, are thoroughly examined. In the EFT parameterisation of the fit, both the t-channel signal and the $t\bar{t}$ background sample have an EFT dependency. Complementary fits are presented in section 6.3.2. These include a fit where only the linear EFT terms are considered, a fit where the $t\bar{t}$ process does not include an EFT dependency and a fit where only one EFT parameter is fitted at the same time.

The fit is performed simultaneously in the SR and the two control regions. The EFT parameters c_{tW}, c_{itW} and c_{qQ} are fitted together with the three normalisation factors and all nuisance parameters. The measured values for the EFT parameters are:

$$
\begin{aligned}
c_{tW} &= 0.11^{+0.06}_{-0.06}\,(\text{stat.})^{+0.22}_{-0.22}\,(\text{syst.}),\\
c_{itW} &= 0.03^{+0.05}_{-0.05}\,(\text{stat.})^{+0.07}_{-0.07}\,(\text{syst.}),\\
c_{qQ} &= 0.18^{+0.05}_{-0.05}\,(\text{stat.})^{+0.22}_{-0.22}\,(\text{syst.}).
\end{aligned}
$$

The values of the Wilson coefficients all agree with the SM within one standard deviation. The measurement is dominated by systematic uncertainties. In fig. 6.3 the scan of the negative likelihood is plotted for all three EFT parameters. The plot displays the value of the likelihood ratio as a function of c_{tW} in red, c_{itW} in blue and c_{qQ} in green. The points where q has increased to 1 and just below 4, indicated by the dashed lines, correspond to the 68 % and 95 % confidence level intervals. All the likelihood scans show a quadratic dependence. The expected sensitivities of the EFT coefficients are:

$$c_{tW} = 0.00^{+0.22}_{-0.22},$$
$$c_{itW} = 0.00^{+0.08}_{-0.08},$$
$$c_{qQ} = 0.00^{+0.23}_{-0.23}.$$

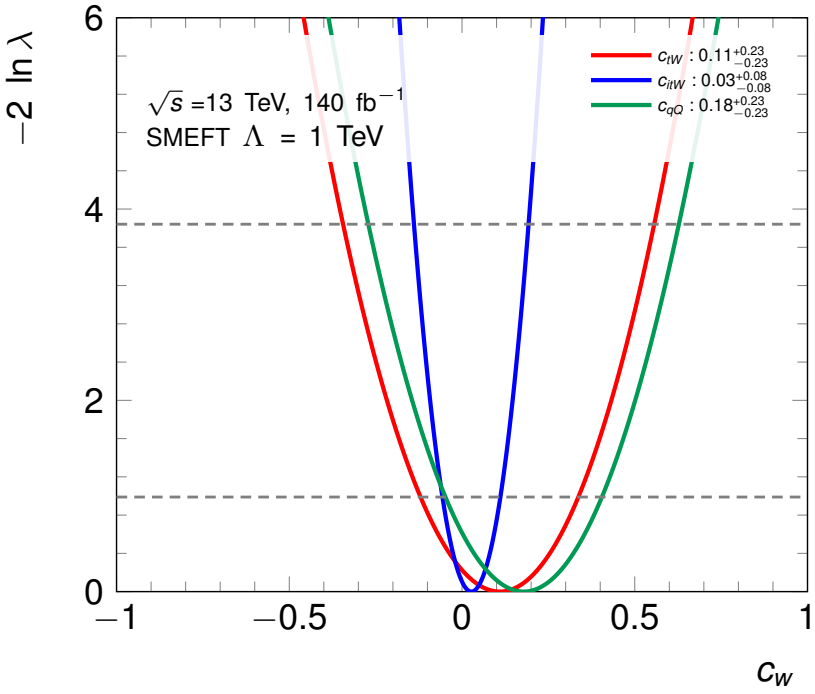

Figure 6.3: Likelihood scan for the EFT parameters c_{tW} in red, c_{qQ} in blue and c_{itW} in green including, EFT effects on the $t\bar{t}$ process. The dashed lines at 1 and just below 4 correspond to the 68 % and 95 % confidence level intervals respectively.

The two-dimensional likelihood contours are shown in fig. 6.4. The contours show the values where the likelihood increased with a value of 1.14 and 3.0. These values represent the 68 % and 95 % confidence limit intervals respectively. A modest correlation between c_{tW} and c_{qQ} is observed. There appears to be no correlation between c_{itW} to the other two EFT parameters.

In the fit the normalisation factors are left freely floating and measured as:

$$\mu_{\text{t-channel}} = 1.05^{+0.09}_{-0.08},$$
$$\mu_{t\bar{t}} = 1.05^{+0.13}_{-0.13},$$
$$\mu_{W+\text{jets}} = 0.99^{+0.11}_{-0.10}.$$

All three are within the expectations of the SM, indicating a good understanding of the signal and background processes. The measured normalisation of the t-channel process can be interpreted as a measurement of Wilson coefficient $c_{\phi Q}$ which only affects the overall normalisation. However since this analysis focuses on using the shape of the distribution and not all systematic sources affecting the rate of the t-channel process are included, parameter $c_{\phi Q}$ is not extracted in this work.

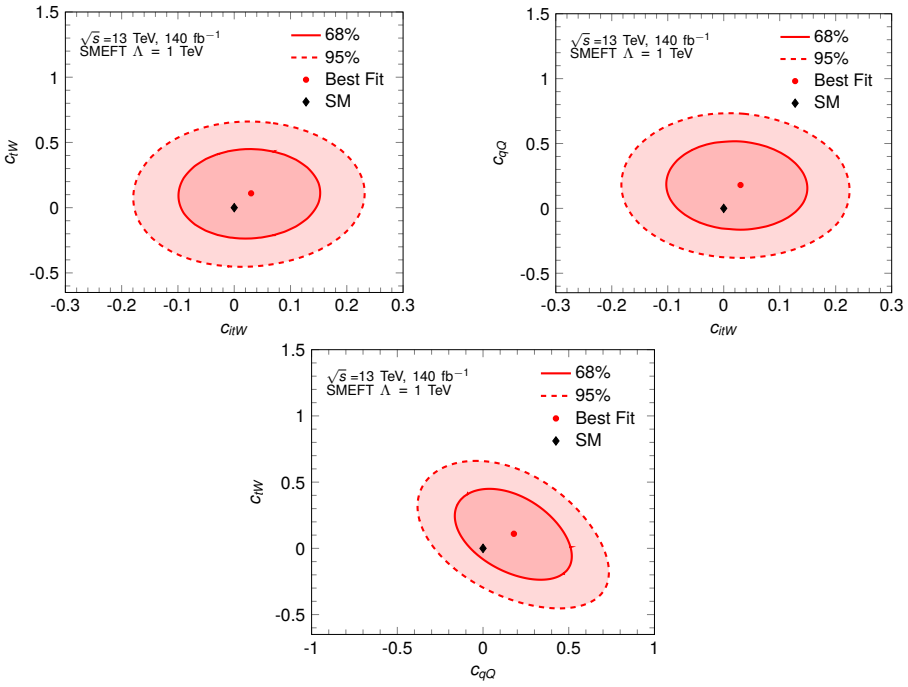

Figure 6.4: Two-dimensional likelihood scans for c_{tW} vs c_{itW} (upper left), c_{itW} vs c_{qQ} (upper right) and c_{tW} vs c_{qQ} (bottom).

Post-fit distribution

The distribution of the O(16) observable after performing the fit is shown in fig. 6.5. In this post-fit distribution the best fit values and uncertainties for all the parameters are used. The agreement between data is good, with a χ^2 value of 0.3 after performing the fit. The event yields of all the different processes and data are shown for the three regions in table 6.1.

Table 6.1.: Yields for the different regions for each process and data.

Process:	SR	W+jets CR	$t\bar{t}$ CR
t-channel	$59\,700 \pm 700$	$170\,000 \pm 6000$	$16\,100 \pm 800$
$t\bar{t}$	$11\,210 \pm 280$	$636\,000 \pm 14\,000$	$150\,500 \pm 1500$
s-channel	207 ± 13	9200 ± 500	4100 ± 500
tW	1380 ± 50	$92\,000 \pm 4000$	4400 ± 600
W+jets	$14\,500 \pm 1200$	$560\,000 \pm 26\,000$	$19\,300 \pm 830$
Z+jets, VV	1100 ± 120	$46\,100 \pm 3300$	2800 ± 340
Others	23 ± 8	1570 ± 540	480 ± 190
Fakes	800 ± 400	$24\,000 \pm 5000$	1030 ± 230
Total	$88\,990 \pm 300$	$1\,539\,500 \pm 1200$	$198\,800 \pm 400$
Data	88 988	1 539 455	198 831

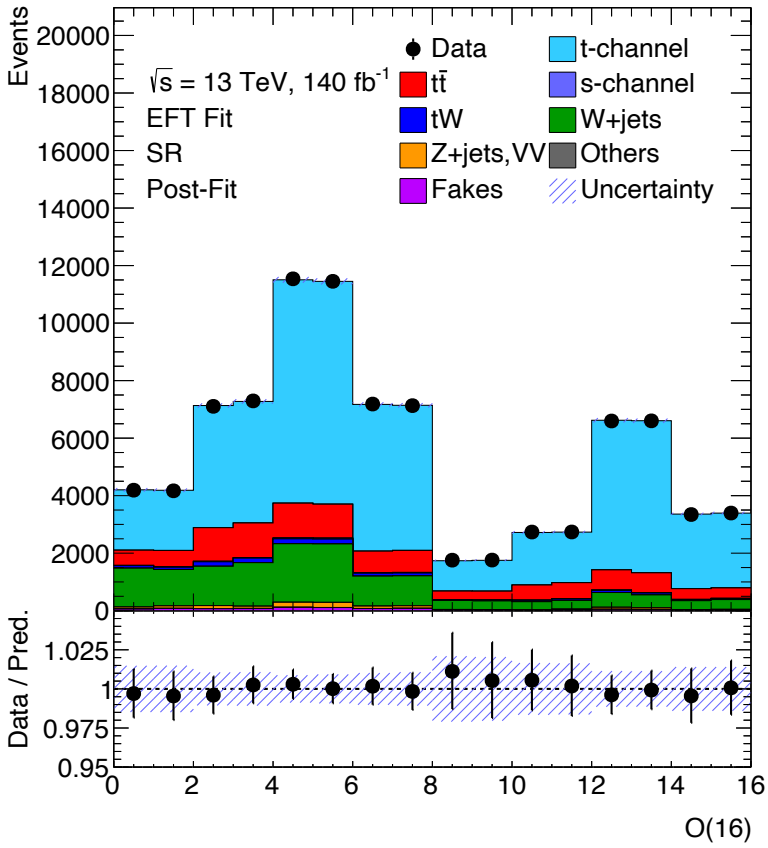

Figure 6.5: Post-fit distribution of the O(16) observable. The observed distribution (dots) is compared with the expected distribution (histograms) where all parameters are set to their values after performing the fit. In the distribution the t-channel contribution is stacked upon the contribution from all considered background processes. The lower panel shows the ratio of data to the prediction in each bin. The shaded uncertainty band includes the uncertainty from systematic sources and from limited MC statistics.

6.3.1 Breakdown of the systematic uncertainties

In this section the dependency on nuisance parameters is further studied. For this purpose, the *pull*, the *constraint* and the *impact* are evaluated.

The pull is the observed offset of a parameter, normalised to units of standard deviation, which is just the value of the nuisance parameter by construction. The constraint is defined by observing a smaller uncertainty of a nuisance parameter than unity.

The impact each parameter has on the total uncertainty is estimated by fixing each nuisance parameter one by one to its up and down error from its best fit value. With each fixed value a new fit is performed, resulting in different estimates of the Wilson coefficients. The difference of the Wilson coefficients of this fit, $\hat{c}'$, with the nominal fit result, $\hat{c}$, is defined as the impact:

$$\text{impact} = \hat{c} - \hat{c}' \tag{6.5}$$

This impact can be estimated using either the pre-fit uncertainties of the nuisance parameters, where the up and down errors are taken as ± 1 or post-fit where the uncertainty is taken from the fit.

In general, when the impact is smaller for the post-fit result than for the pre-fit result, the corresponding nuisance parameter is constrained by the fit. This implies that the fit model has a dependency on this nuisance parameter.

The impact on each Wilson coefficient is ranked by its individual contribution to the final uncertainty. The rankings are shown for each EFT coefficient in figs. 6.6 to 6.8. The open dark and light blue boxes correspond to the +1 and -1 sigma pre-fit impact and the coloured boxes correspond to the post-fit impact. Note that for the normalisation factors, no pre-fit impact is shown since they are left freely floating in the fit.

The black points and error bars represent the best fit value (the pull) and uncertainty for that nuisance parameter and correspond to the lower horizontal axis. If the uncertainty is smaller than unity, the nuisance parameter is constrained.

Across the board, the impact, pull and constraint is relatively small for most nuisance parameters, but there are two exceptions.

The jet flavour composition of t-channel events is $-0.38^{+0.78}_{-0.74}$, which is consistent with the expectation of 0, but its uncertainty indicates a constraint. As the uncertainty on the flavour composition is overestimated as explained in section 6.2, this constraint is expected.

The t-channel p_{T} hard matching uncertainty is an estimated systematic effect by varying the corresponding settings in the MC simulation. It cannot be presumed that all details on the shape of notably the p_{T} distribution are fully described with only one nuisance parameter. Therefore, the t-channel p_{T} hard matching uncertainty

is conservatively split for a nuisance parameter in the high and low momentum.

The measured value of the pthard matching nuisance parameter in the low momentum bins is $-0.22^{+0.81}_{-0.81}$. The high momentum nuisance parameter on the matching uncertainty is measured as $-0.71^{+0.63}_{-0.62}$. Especially the high momentum nuisance parameter is pulled from the expectation. The results suggest that these settings are less consistent with the data than the original simulation.

As a check, additional fits where this nuisance parameter is fixed to zero and ± 1 are conducted. The measured EFT coefficients for a zero-value of pthard are $c_{tW} = 0.08^{+0.23}_{-0.23}$, $c_{itW} = 0.01^{+0.08}_{-0.08}$ and $c_{qQ} = 0.22^{+0.23}_{-0.23}$. This indicates that the impact of fixing this nuisance parameter is smaller than the total uncertainty on each Wilson coefficient. Fixing the nuisance parameter to ± 1 results in a shift of ∓ 0.04 for c_{tW}, a shift of ∓ 0.03 on c_{itW} and a shift of ± 0.06 of c_{qQ}. This check implies that any effects are well within the uncertainty of this measurement, although the observed pull and constraints suggest that the data allows further studies on the matching uncertainty.

Lastly, the contribution of several classes of systematic sources to the uncertainty of the Wilson coefficients is extracted. This "grouped impact" is calculated by fixing all the nuisance parameter of a certain group to their post-fit value and redo the fit with the fixed nuisance parameters. The contribution is defined as the quadratic difference between the uncertainty on the Wilson coefficients of the nominal fit, $\hat{\sigma_c}^2$, and the fit with the nuisance parameters fixed, ${\sigma_{\hat{c}'}}^2$:

$$\text{grouped impact} = \sqrt{{\sigma_{\hat{c}}}^2 - {\sigma_{\hat{c}'}}^2}. \tag{6.6}$$

The results are listed in table 6.2. The systematic uncertainties dominate the measurements. The instrumental systematic effects mostly originate from the jet energy measurements. The theoretical uncertainties are of a similar size as the experimental effects.

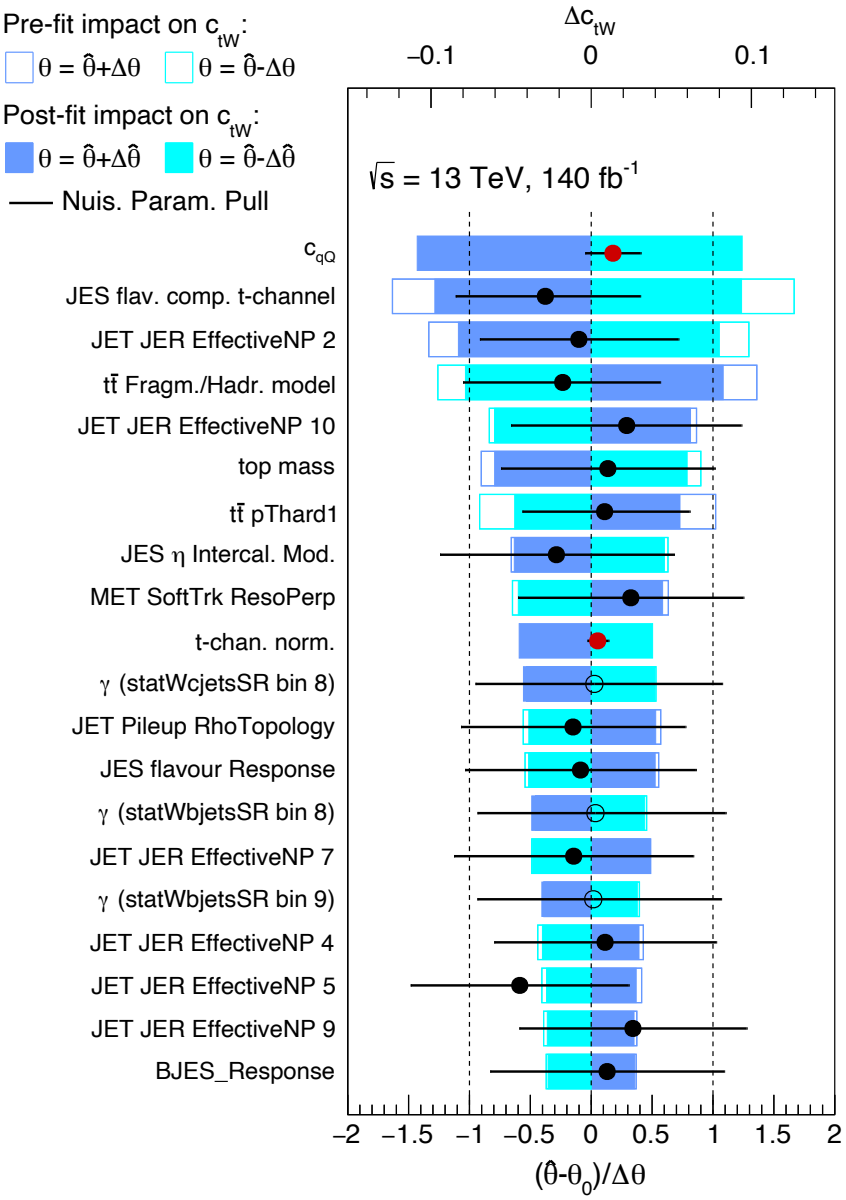

Figure 6.6: The impact of each individual nuisance parameter on the EFT coefficient c_{tW}, sorted in decreasing order. The open dark and light blue boxes correspond to the +1 and -1 sigma pre-fit impact and the coloured boxes correspond to the post-fit impact. The black points and error bars represent the best fit value (the pull) and uncertainty for that nuisance parameter and correspond to the lower horizontal axis.

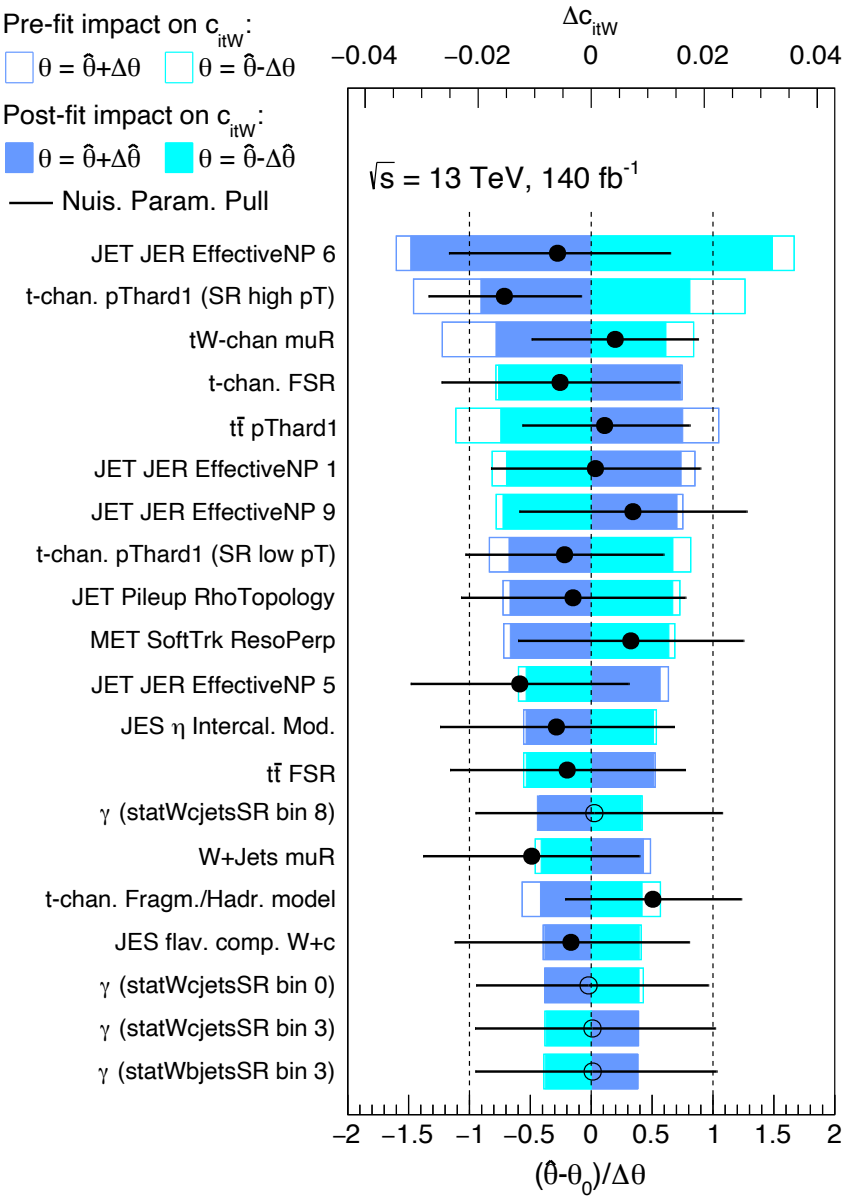

Figure 6.7: The impact of each individual nuisance parameter on the EFT coefficient c_{itW}, sorted in decreasing order. The open dark and light blue boxes correspond to the +1 and -1 sigma pre-fit impact and the coloured boxes correspond to the post-fit impact. The black points and error bars represent the best fit value (the pull) and uncertainty for that nuisance parameter and correspond to the lower horizontal axis.

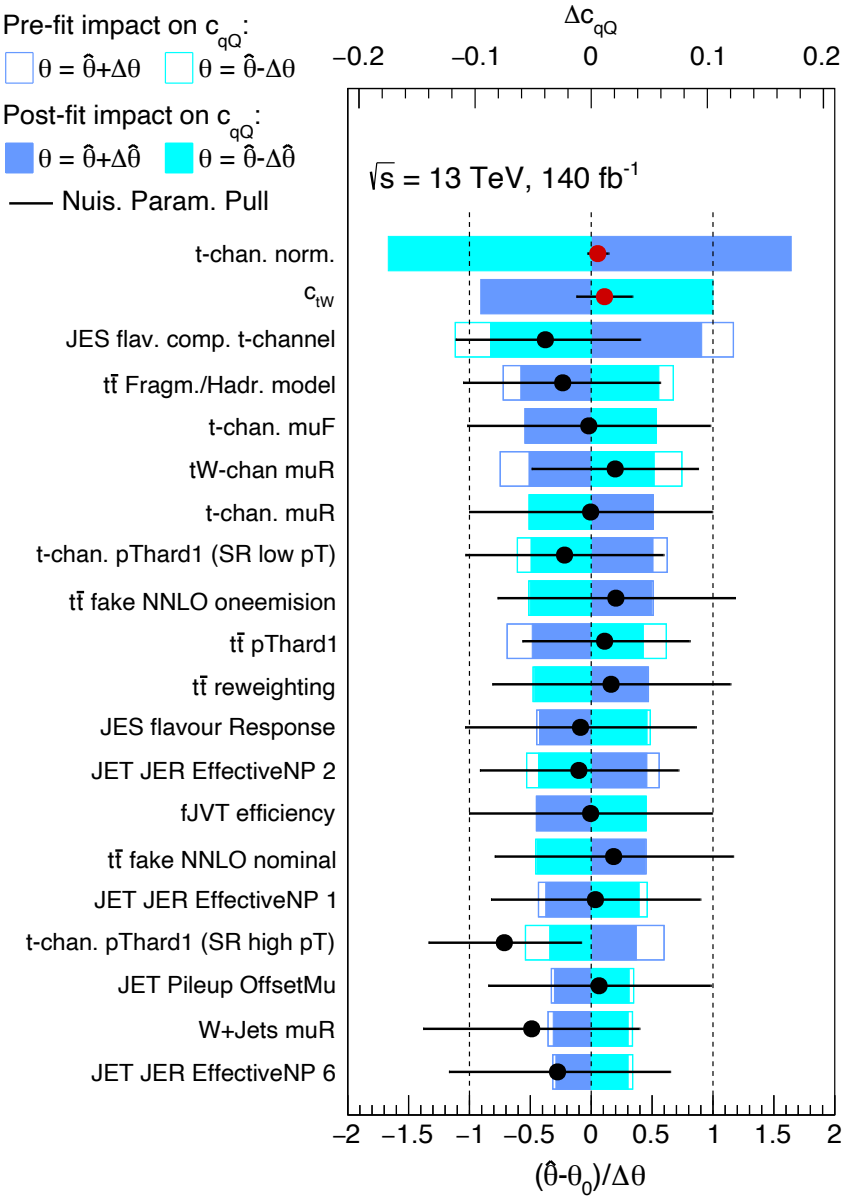

Figure 6.8: The impact of each individual nuisance parameter on the EFT coefficient c_{qQ}, sorted in decreasing order. The open dark and light blue boxes correspond to the +1 and -1 sigma pre-fit impact and the coloured boxes correspond to the post-fit impact. The black points and error bars represent the best fit value (the pull) and uncertainty for that nuisance parameter and correspond to the lower horizontal axis.

Table 6.2.: Breakdown of the contribution of several classes of systematic sources to the uncertainty on the Wilson coefficients. The quadratic sum of the individual sources does not add up to the total sum due to correlations between nuisance parameters.

Source:	c_{tW}	c_{itW}	c_{qQ}
Total uncertainty	0.23	0.08	0.23
Statistical uncertainty	0.06	0.05	0.05
Systematic uncertainty	0.22	0.07	0.22
Experimental uncertainties	0.19	0.05	0.16
Flavour tagging	0.02	0.001	0.01
JER	0.13	0.05	0.09
JES	0.16	0.02	0.13
JET efficiency	0.05	0.02	0.06
MET	0.05	0.01	0.02
Leptons	0.02	<0.01	<0.01
Lumi+Pile.up	<0.01	<0.01	<0.01
Theory uncertainties	0.12	0.05	0.17
PDF	0.04	0.02	0.06
t-channel modelling	0.09	0.03	0.11
$t\bar{t}$ modelling	0.09	0.02	0.12
tW modelling	0.01	<0.01	<0.01
W+jets modelling	0.03	0.02	0.06
Other background modelling	<0.01	<0.01	<0.01
Fake background	0.02	<0.01	0.02
MC stat. uncertainties	0.08	0.03	0.06
t-channel	0.02	<0.01	0.02
$t\bar{t}$	0.02	<0.01	0.01
W+b-jets	0.05	0.02	0.04
W+c-jets	0.05	0.02	0.03
Other	0.02	0.01	0.02

6.3.2 Complementary fit results

When performing a fit with EFT parameters several assumptions are made. For instance, if one considers quadratic terms or not in the EFT parameterisation. Whether the background, in this study the $t\bar{t}$ process, is affected by EFT parameters. And lastly if all EFT parameters are allowed to be freely floating or if only one EFT parameter is allowed to vary at the same time. The impact on the Wilson coefficients of these assumptions are studied in the following. A summary of all the different fit models is presented in table 6.3.

Linear EFT fit

In the nominal analysis presented in this thesis, the quadratic terms of the Wilson coefficients in the parameterisation are included. One could argue that this leads to contributions which are not strictly of order dim-6 in the EFT. To study possible effects, an additional fit has been performed where only the linear terms in EFT are considered. The best-fit values on the EFT coefficients are:

$$c_{tW} = 0.10^{+0.22}_{-0.21},$$
$$c_{itW} = 0.03^{+0.08}_{-0.08},$$
$$c_{qQ} = 0.18^{+0.20}_{-0.22},$$

thus only leading to small changes in the measured values of the EFT parameters. This is an indication that higher dimensional operators are only contributing marginally.

Fit with SM $t\bar{t}$

An assumption made in many EFT measurements is that only the signal events are altered by EFT effects, while the backgrounds remain unaffected. Even in most global combinations, it is implicitly assumed that all backgrounds are SM-like. This is a consequence of using several results on published data that are corrected for backgrounds based on SM simulations.

In this analysis, the EFT effects on the $t\bar{t}$ background are explicitly taken into account. To study the effect of just ignoring this dependence, a fit is conducted with $t\bar{t}$ set to its SM prediction. This results in:

$$c_{tW} = 0.10^{+0.23}_{-0.23},$$
$$c_{itW} = 0.03^{+0.08}_{-0.08},$$
$$c_{qQ} = 0.18^{+0.23}_{-0.23}.$$

The normalisation of the $t\bar{t}$ process is now measured as $\mu_{t\bar{t}} = 1.05^{+0.13}_{-0.11}$ and thus does not change with respect to the nominal fit result. This is also the case for the normalisation of the t-channel and the W+jets process.

Note, the $t\bar{t}$ process is also affected by other operators that do not affect the t-channel production mechanism. These operators are not considered in the (nominal) analysis, as there is only very little sensitivity expected compared to dedicated $t\bar{t}$ analyses.

Individual parameter fit

Individual fits are performed where only one Wilson is changed, while the other two are fixed to the SM value. These fits neglect the correlation between the different coefficients, which would reflect a new physics model in which only one Wilson coefficient changes. The measured values of the EFT coefficients are:

$$c_{tW} = 0.18^{+0.21}_{-0.21},$$
$$c_{itW} = 0.03^{+0.09}_{-0.09},$$
$$c_{qQ} = 0.23^{+0.20}_{-0.21}.$$

Table 6.3.: Results on the Wilson coefficients for different fit models.

Fit type	$\mathbf{c_{tW}}$	$\mathbf{c_{itW}}$	$\mathbf{c_{qQ}}$
Nominal fit	$c_{tW} = 0.11^{+0.23}_{-0.23}$	$c_{itW} = 0.03^{+0.08}_{-0.08}$	$c_{qQ} = 0.18^{+0.23}_{-0.23}$
Linear fit	$c_{tW} = 0.10^{+0.22}_{-0.21}$	$c_{itW} = 0.03^{+0.08}_{-0.08}$	$c_{qQ} = 0.18^{+0.20}_{-0.22}$
$t\bar{t}$ SM fit	$c_{tW} = 0.10^{+0.23}_{-0.23}$	$c_{itW} = 0.03^{+0.08}_{-0.08}$	$c_{qQ} = 0.18^{+0.23}_{-0.23}$
Individual fit	$c_{tW} = 0.18^{+0.21}_{-0.21}$	$c_{itW} = 0.03^{+0.09}_{-0.09}$	$c_{qQ} = 0.23^{+0.20}_{-0.21}$

6.4 Comparison with other analysis

A previous result from ATLAS uses the t-channel polarisation angles [81] only. In this analysis, the respective 68 % confidence level intervals are [-0.3,0.8] for c_{tW} and [-0.5,-0.1] for c_{itW}. This is still the most stringent published limit up to date for c_{itW}, from collider physics experiments. This analysis is a factor 2.5 better with respect to measuring c_{tW} and a factor 3 better for measuring c_{itW}. Additionally, it also measures the c_{qQ} parameter simultaneously.

A combination of Higgs data measured by the ATLAS experiment and electroweak precision observables by LEP also performs a fit on EFT parameters [106]. This analysis does not constrain c_{tW} and c_{itW} and is only able to constrain a linear combination of c_{qQ} with other four quark operators. The constrain on this linear combination is of the same magnitude as this analysis. Including this measurement in a future combination will thus improve the result and will help resolve redundancies in the fit.

CMS recently released an EFT measurement of 26 different Wilson coefficients using final states of top quarks in association with leptons. They measure a 1σ interval of [-0.31,0.22] for c_{tW} and [-0.04,0.03] for c_{qQ} [107]. They only take CP-conserving

coefficients into account.

Global EFT fits are also performed by theorists [108] combining several analyses from ATLAS and CMS. The 95% confidence level is [-0.24,0.09] for c_{tW} and [-0.17,0.20] for c_{qQ}. The result is roughly a factor 2 better than this analysis. Global fits do not (yet) take into account c_{itW}. A more recent result, simultaneously measures parton densitiy function distributions, with a 95% CL of [-0.1,0.3] for c_{tW} and [-0.3,0.1] for c_{qQ} [109].

A large downside of the EFT combinations from theorists is that they do not have access to systematic correlations between different analysis, and need to apply ad-hoc assumptions. These fits also assume that the backgrounds in each analysis is pure SM, which is not necessarily the case.

Chapter 7

Prospects

In the previous chapters, the Wilson coefficients c_{tW}, c_{itW} and c_{qQ} are extracted with unprecedented precision in the single top t-channel process. The precision turns out to be limited by systematic uncertainties. This entails that simply increasing statistics will not make this analysis more precise. In this chapter, potential future improvements are discussed to increase the precision on EFT coefficients.

7.1 Improved uncertainty estimation

The presented result is mainly limited by uncertainties on jets and from the theoretical modelling of top processes. The possibilities to reduce in particular these systematic effects are discussed here.

7.1.1 Jet uncertainties

The largest jet related uncertainty is the flavour composition. The energy response of jets in ATLAS is different for quarks and gluons. In ATLAS the flavour dependent correction of jets is applied on an average basis, assuming that a certain fraction of jets is originating from gluons. In this analysis the assumption is made that 50% of all the jets originate from gluons.

To account for the systematic uncertainty between the jet flavour composition between MC simulation and data, the events are also reconstructed under the extreme assumption that all (and also none) of the jets originate from gluons. This conservative approach has been revised recently in the ATLAS collaboration.

In the new strategy, the assumption on the average flavour composition is dropped and corrections are applied based on the truth parton information of the jet. This approach introduces however several new components to cover the systematic uncertainties based on the actual differences between different parton showering models and the energy response of quarks and gluons jets in different models. Nevertheless, it is expected that the overal effect from this source will be reduced.

7.1.2 Modelling uncertainties

Another large contribution to the overall systematic uncertainty is the impact from the modelling of the different processes. Uncertainties on the shower model and the matching between the showering algorithm with the generator of the hard scattering process are affecting this analysis precision in particular. Further studies are needed to improve the modelling and reduce the uncertainty. New parton shower algo-

rithms like VINCIA [110–113] and DIRE [114] are currently developed. They have improved modelling of the showering algorithm and a more coherent treatment of matching and merging of the parton shower algorithm and the hard scattering matrix element generator. This would allow for a better treatment of the systematic uncertainty arising from the parton showering algorithm.

A second improvement of the modelling of the t-channel is to include higher order calculations. The differential cross-section calculation of the t-channel process used by this analysis is accurate in QCD up to NLO. Recent developments are made to calculate the t-channel process up until NNLO precision in QCD [115]. These NNLO corrections make the top quark transverse momentum distribution harder and the light quark pseudorapidity spectrum more central. The effect of NNLO corrections on the polarisation angles is less profound. The effect is only estimated at parton level and needs to be interfaced with parton showering algorithms.

7.2 Combination with other analysis

One of the main benefits of parameterising new physics in the form of an EFT is that it coherently affects different physics processes. Therefore, different analysis are able to measure EFT Wilson coefficients and by combining these measurements, deviations from the SM can be searched for in a coherent way. This entails that the assumption that only one process is modified while the others are SM is no longer valid. This has been studied for the $t\bar{t}$ process in this analysis. The impact was found to be relatively small, however this is not necessarily true for any other analysis. A combined fit including analysis including top quarks, Higgs bosons and electroweak precision observables would be the ultimate goal to measure the EFT Wilson coefficients. A combination of top pair production, top production in association with other particles and the analysis presented in this thesis would be a first step for a combined search for new physics in top interactions.

Several analyses of the decay of top quarks in $t\bar{t}$ events have been performed. An example is the measurement of the helicity angle, which has good sensitivity to the c_{tW} operator. A future combination between the helicity angle measurement in $t\bar{t}$ events and the t-channel polarisation analysis could potentially improve sensitivity of the c_{tW} operator. Additionally, it could reduce correlations between c_{tW} and c_{qQ}. The $t\bar{t}$ process is also affected via the production by additional Wilson coefficients. Most notably c_{tG} and several four fermion operators. These can also be measured by studying the $t\bar{t}$ production in more detail. These measurements include charge and energy asymmetry of $t\bar{t}$ production, measurement of spin correlations between the two top quarks and a measurement of the invariant mass of the $t\bar{t}$ system.

Including measurements where top quarks are produced in association with a Z- or W-boson can further improve sensitivity. Examples are the $t\bar{t}W$, $t\bar{t}Z$, tZq and the four top production. Due to the significantly smaller cross-section they are usually measured with less precision and give smaller constrains on coefficients with respect to measurements in $t\bar{t}$ and t-channel production. However, they have sensitivity to additional operators, for example c_{tZ} and $c_{\phi t}$. These top+X measurement are not able

to measure all EFT coefficients simultaneously, but a combination with the t-channel and $t\bar{t}$ process will remove blind directions.

7.3 Future ATLAS data taking periods

The ATLAS detector only collected a fraction of the total data it is intended to collect. It currently takes data in the ongoing Run 3 data taking period aiming to double the total amount of luminosity. During the high luminosity LHC the ATLAS detector aims to collect a total luminosity of 4000 fb^{-1}. In this period the ATLAS will also have a new tracker, the ITK.

As this analysis is systematically limited, collecting more data will not increase the precision. Due to the higher number of pile-up interactions the precision may even decrease due to a reduced reconstruction accuracy. However this does not mean that future runs do not offer chances to improve this measurement. The vast amount of data allows to measure t-channel events in more extreme phase-spaces, for example at very high top momentum. Top quarks with transverse momentum of a few 100 GeV are only rarely produced, however have enhanced sensitivity to new physics effects. With the data collected in future LHC runs a precision study of t-channel events in this phase-space is a promising method to search for new physics. With the installment of the ITK, the tracking will cover an area up to a pseudorapidity of 4. This allows to identify b-jets also in the forward region, which should reduce the background contribution of this analysis especially from $t\bar{t}$ and the production of W+b-jets events. This could improve the sensitivity of the t-channel analysis.

7.4 The analysis of the full decay spectrum of the top quark

The measurement of the decay properties of the top quark is a great probe to find new physics. Asymmetries in the polarisation angles, together with the top p_{T} spectrum in the t-channel production mechanism are sensitive probes for the measurement of EFT Wilson coefficients. The number of events in bins of the O(16) observable are used in this work to measure the relevant Wilson coefficients. Instead of doing a binned analysis in the O(16) observable an alternative approach is to decompose the angular decay spectrum of the top quark into a set of eigenfunctions and measure their corresponding coefficients. This procedure is explained in the following and preliminary results are discussed.

7.4.1 Introduction to the M-function decomposition

The decay spectrum of the top quark can be fully described by a set of four angles [116]. These are the spherical angles, ϕ and θ, of the decaying W-boson in the rest-frame of the top quark and the helicity angles, ϕ^* and θ^*, of the lepton in the W-boson rest frame.

In general the decay of a particle can be parameterised using the helicity formalism of Jacob and Wick [117]. This means that the amplitude, A, of the decay can be

parameterised using Wigner D functions:

$$A_{M\lambda_2\lambda_3\lambda_4} = \sum_{\lambda_1} a_{\lambda_1\lambda_2} b_{\lambda_3\lambda_4} D^{1/2*}_{M\Lambda}(\phi,\theta,0) D^{1*}_{\Lambda_1\lambda}(\phi^*,\theta^*,0). \tag{7.1}$$

Here λ_1, λ_2, λ_3 and λ_4 are the helicities of the W-boson, b-quark, charged lepton and the neutrino, M is the third spin component of the top quark, $\Lambda = \lambda_1 - \lambda_2$ and $\lambda = \lambda_3 - \lambda_4$. Lastly $a_{\lambda_1\lambda_2}$ and $b_{\lambda_3\lambda_4}$ are constants.

Due to the spin structure of the Wtb vertex as explained in section 2.2.1, only $a_{1\frac{1}{2}}$, $a_{0\frac{1}{2}}$, $a_{0-\frac{1}{2}}$, and $a_{-1-\frac{1}{2}}$ are non-zero. As the SM decay of the W-boson, in the case of massless leptons, always produces a neutrino with helicity $-1/2$ only one non-zero coefficient b exists for each helicity state of the W-boson.

As the decay distribution is the amplitude A squared the resulting distribution as function of the 4 angles is:

$$\begin{aligned}\frac{1}{\Gamma}\frac{d\Gamma}{d\Omega d\Omega^*} =& \frac{3}{8\pi^2}\frac{1}{N}\sum_{MM'\lambda\lambda_1'\lambda_2} \rho_{MM'} a_{\lambda_1\lambda_2} a^*_{\lambda_1'\lambda_2} D^{1/2*}_{M\Lambda}(\phi,\theta,0) \\ & D^{1/2}_{M'\Lambda'}(\phi,\theta,0) D^{1*}_{\Lambda_1\lambda}(\phi^*,\theta^*,0) D^{1}_{\Lambda_1'\lambda}(\phi^*,\theta^*,0).\end{aligned} \tag{7.2}$$

Here $d\Omega = d\phi d\cos\theta$, $d\Omega^* = d\phi^* d\cos\theta^*$, $\Lambda' = \lambda_1' - \lambda_2$ and N the squared sum of the four non-vanishing amplitudes. The sum over the polarisations of the top quark is parameterised via the spin density matrix:

$$\rho = \frac{1}{2}\begin{pmatrix} 1+P_z & P_x - iP_y \\ P_x + iP_y & 1+P_z \end{pmatrix}. \tag{7.3}$$

Expression 7.2 can further be simplified using the properties of the Wigner D functions and the composition rules of Clebsch-Gordan coefficients, which leads to a set of finite combinations of so-called orthonormal M-functions defined as:

$$M^{j_1 j_2}_{m' m}(\phi,\theta,\phi^*,\theta^*) = \frac{1}{4\pi}(2j_1+1)^{1/2}(2j_2+1)^{1/2} D^{j_1}_{m' m}(\phi,\theta,0) D^{j_2}_{m0}(\phi^*,\theta^*,0). \tag{7.4}$$

The distribution of the decay of the top quark is thus:

$$\frac{1}{\Gamma}\frac{d\Gamma}{d\Omega d\Omega^*} = \sum_{j_1 j_2 m' m} c^{j_1 j_2}_{m' m} M^{j_1 j_2}_{m' m}. \tag{7.5}$$

Using the rules of spin addition we get the following values for the indices $j_1 \in [0,1]$, $j_2 \in [0,1,2]$ and m' and $m \in [-1,0,1]$.

The full distribution can thus be described by a set of 15 M-functions. There are 6 M-functions with a pure real parameter and 9 which are complex resulting in a total of 24 coefficients. These 24 coefficients can be measured by projecting[1] the measured distribution, $g(\phi,\theta,\phi^*,\theta^*)$, on the different M-functions:

$$c^{j_1 j_2}_{m' m} = \int d\Omega d\Omega^* g(\phi,\theta,\phi^*,\theta^*) M^{j_1 j_2}_{m' m}(\phi,\theta,\phi^*,\theta^*)^*. \tag{7.6}$$

In practice, these coefficients are measured by computing the average of $M^{j_1 j_2}_{m' m}(\phi,\theta,\phi^*,\theta^*)^*$ from the dataset.

7.4.2 EFT measurement using the M-function decomposition

A measurement of the Wilson coefficients is performed using the M-function decomposition with the same dataset as the polarisation analysis, using the same MC samples and the same selection criteria. The measurement of EFT coefficients from the M-function decomposition is discussed in the following.

The dependency of the M-function coefficients on Wilson coefficients c_{tW}, c_{itW} and c_{qQ} for t-channel single top production is shown in fig. 7.1. In this plot the first 14 coefficients correspond to the real coefficients, while the last 9 correspond to the imaginary coupling strengths[2]. Wilson coefficient c_{tW} mostly affects the real M-function coefficients, while c_{itW} mostly changes the imaginary coefficients as is clear from the plot. This is expected since imaginary M-function coefficients always have a linear dependency on P_y which is changed by c_{itW}. As this measurement is also sensitive to helicity fractions, the $t\bar{t}$ process now also has a dependency on the Wilson coefficients. The EFT dependency of the $t\bar{t}$ process on the M-function coefficients is shown in fig. 7.2. This means that it is crucial that the $t\bar{t}$ process is also properly parameterised when doing the fit on the M-function coefficients.

Each process results in a different set of M-functions describing the distribution of that process. To compare the M-functions estimated from data with MC predictions of the different processes a weighted average is taken, depending on the number of events of each process. The M-functions coefficients and the expected number of events, N_s, of a certain process s depend on the EFT Wilson coefficients, $\vec{c}_{EFT}$ in $t\bar{t}$ and t-channel events as well as normalisation factors, $\vec{\mu}$ and systematic effects, $\vec{\theta}$. The expected value of each M-function is thus:

$$\vec{c}(\vec{c}_{\text{EFT}},\vec{\mu},\vec{\theta}) = \frac{\sum_s N_s(\vec{c}_{\text{EFT}},\mu_s,\vec{\theta})\vec{c}_s(\vec{c}_{\text{EFT}};\vec{\theta})}{\sum_s N_s(\vec{c}_{\text{EFT}},\mu_s,\vec{\theta})}. \tag{7.7}$$

[1] This procedure is very similar to a Fourier transformation, using the M-functions as basis functions

[2] Coefficient $c^{0,0}_{0,0} = \frac{1}{4\pi}$ is not shown as it is constant

To estimate the values of the EFT coefficients most compatible with data, D, a statistical interpretation similar to the polarisation analysis explained in section 6.1 is followed. Contrary to the polarisation measurement, the observables are not event numbers, but M-function coefficients. Therefore, the likelihood term is not constructed using Poison terms. Instead a multivariate Gaussian (MVG) is used, taking into account the statistical correlation between different coefficients via a covariance matrix Σ. The likelihood in this case is thus:

$$\begin{aligned} L_i(\vec{c}_D|\vec{\mu},\vec{c}_w,\vec{\theta}) =& MVG\left(\left(\vec{c}(\vec{c}_{\text{EFT}},\vec{\mu},\vec{\theta})-\vec{c}_D\right)^T\Sigma^{-1}\left(\vec{c}(\vec{c}_{\text{EFT}},\vec{\mu},\vec{\theta})-\vec{c}_D\right)\right) \\ &\cdot\prod_{j=1}^{m} G(0|\theta_j,1). \end{aligned} \tag{7.8}$$

Here systematic effects are incorporated similar to the polarisation analysis via Gaussian constraint terms. The systematics effects considered are the same as in the polarisation measurement. The measurement of the Wilson coefficients is performed using the profile likelihood method.

In the fit not only the leading 3 EFT coefficients c_{tW}, c_{itW} and c_{qQ} are fitted but the EFT coefficients that only have contribution of order Λ^{-4} are included as well. These are the EFT coefficients $c_{\phi tb}$, c_{bW} and c_{ibW}. Contrary to the fit on the O(16) variable, the top momentum spectrum is treated inclusively. The events are however split in a top quark and a top antiquark region.

Preliminary sensitivities estimated on a SM Asimov dataset for all 6 coefficients using the M-function coefficients are:

- $c_{tW} = 0.00^{+0.2}_{-0.2}$
- $c_{itW} = 0.00^{+0.1}_{-0.1}$
- $c_{\phi tb} = 0.00^{+3}_{-4}$
- $c_{bW} = 0.00^{+1}_{-1}$
- $c_{ibW} = 0.00^{+1}_{-1}$
- $c_{qQ} = 0.00^{+0.3}_{-0.3}$

The result is obtained including only the t-channel process, the $t\bar{t}$ background and the W+jets process which make up 95 % of the total contribution. All systematic uncertainties that affect the detector response are included, however not all theory uncertainties are included. Notably the pthard uncertainty and the uncertainty on the showering algorithm are not yet included in this result. They will be included and further studies on the fit model will be performed. The extraction of 6 Wilson coefficients using the M-functions is promising. A direct comparison with the O(16) based analysis is not yet possible. However, for this setup the sensitivity for c_{tW} and

c_{itW} is approximately similar.

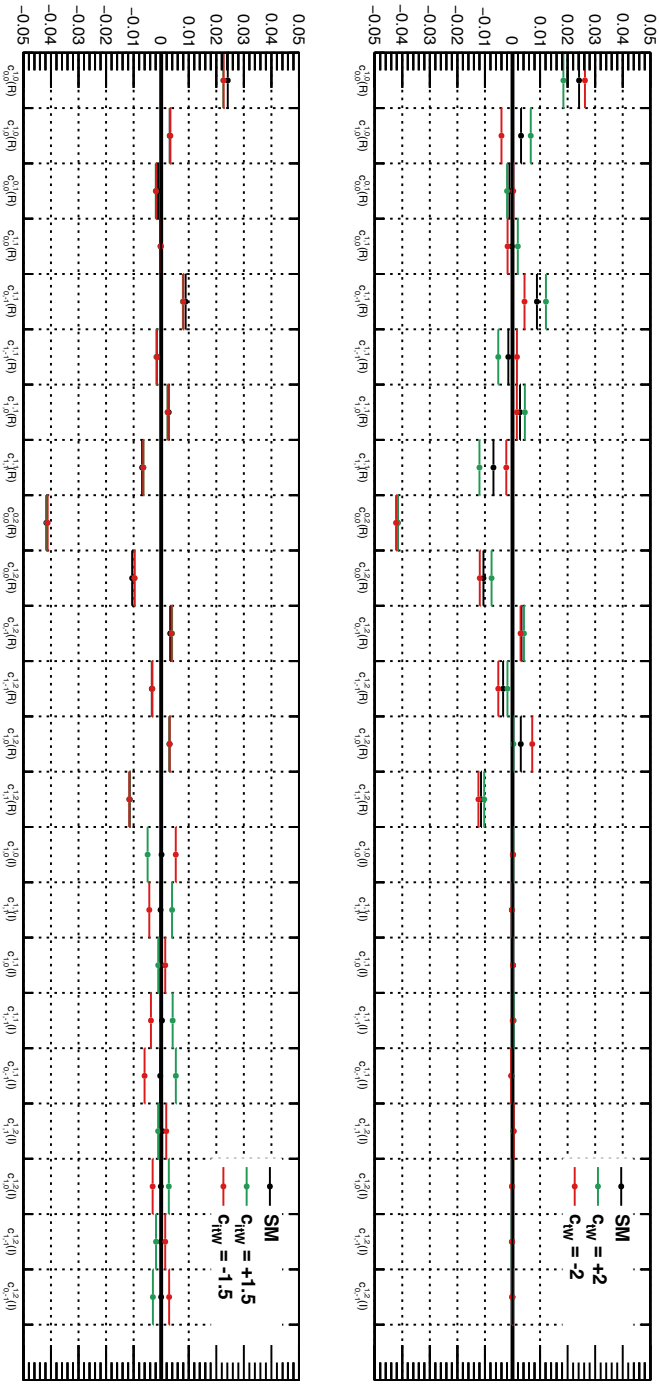

Figure 7.1: Dependency of the M-function coefficients on c_{tW} (top), c_{itW} (bottom) for the t-channel process.

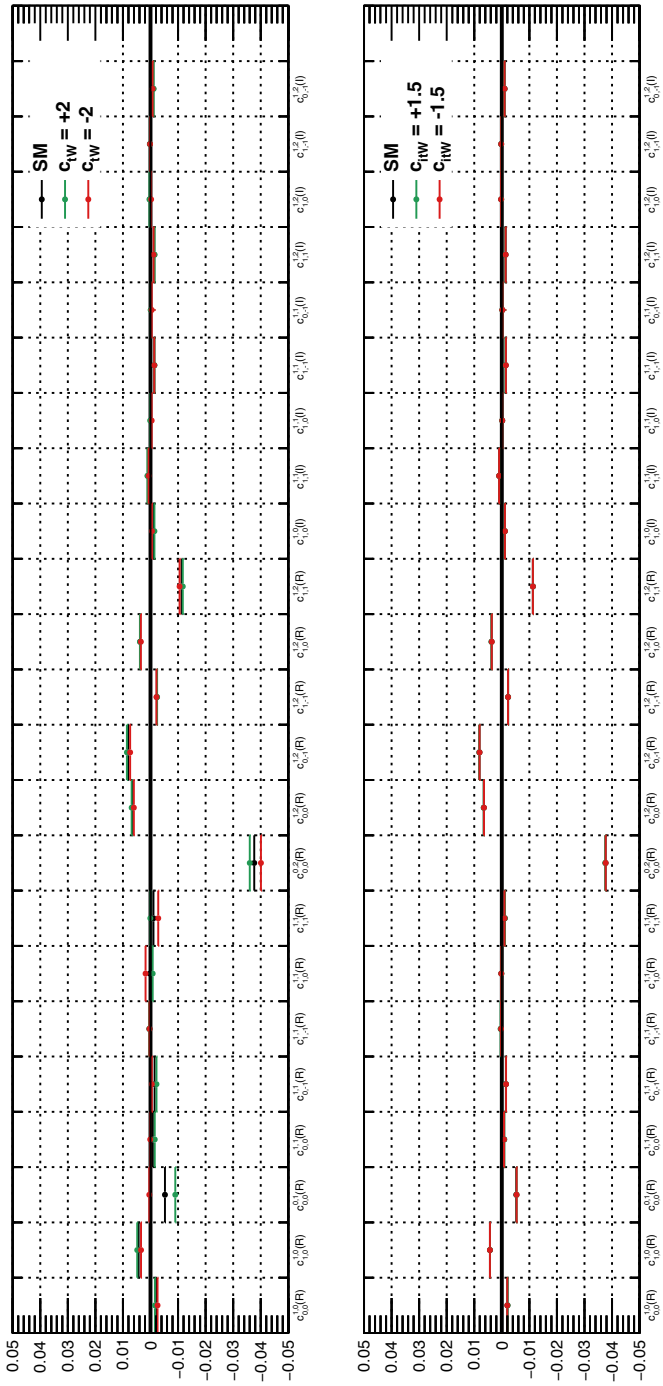

Figure 7.2: Dependency of the M-function coefficients on c_{tW} (top), c_{itW} (bottom) for the $t\bar{t}$ process.

Chapter 8

Conclusion

The large dataset of the LHC proton-proton collisions offers unique opportunities to search for any deviations of the Standard Model (SM) predictions. This thesis presents a search for deviations in electroweak interactions of single top quarks in the t-channel, which are interpreted in the scope of an effective field theory (EFT). In this EFT approach the SM is extended with additional dimension-6 operators with contributions tuned by corresponding Wilson coefficients.

The lowest order operators that modify the t-channel production process of top quarks are O_{tW} and $O_{qQ}^{3,1}$. The operator O_{tW} produces a right handed top quark with a real coefficient c_{tW} and imaginary coefficient c_{itW}. A non-zero value of the c_{itW} coefficient would flag a new CP-violating interaction term, which could explain the matter-antimatter asymmetry observed in the universe. The top quark spin in a t-channel interaction is highly polarised and thus sensitive to c_{itW}. A new contact interaction between four quarks is included via coefficient c_{qQ} and would change the top momentum spectra.

The measurement of these Wilson coefficients is the main topic of this thesis, which uses the data collected with the ATLAS detector in Run 2, corresponding to 140 fb^{-1}. Top quarks are produced abundantly, but the initial background is overwhelming. To limit background contributions, the analysis focuses on the leptonic decay channel and requires each reconstructed object to have a transverse energy typically greater than 30 GeV. Additional specific criteria use the topological signature of the t-channel process. Furthermore, a reconstruction of the top quark based on a kinematic likelihood method is used to significantly reduce the remaining background of non t-channel events and the number of mis-reconstructed t-channel events.

The asymmetries in the angular distributions of the top quark decay products, in combination with the transverse momentum of the top quark, are used to map all information into one variable, O(16). The extraction of EFT coefficients is based on a profile likelihood fit method. In this method, the Wilson coefficients are extracted by maximising a Poison likelihood function. Systematic uncertainties are incorporated in this method via nuisance parameters with Gaussian constraint terms. Uncertainties in the reconstruction of high energetic proton collisions by the ATLAS detector as well as uncertainties in the modelling of the events are considered. The EFT coef-

ficients c_{tW}, c_{itW} and c_{qQ} are measured simultaneously, resulting to:

$$c_{tW} = 0.11^{+0.06}_{-0.06}\ (\text{stat.})^{+0.22}_{-0.22}\ (\text{syst.}),$$
$$c_{itW} = 0.03^{+0.05}_{-0.05}\ (\text{stat.})^{+0.07}_{-0.07}\ (\text{syst.}),$$
$$c_{qQ} = 0.18^{+0.05}_{-0.05}\ (\text{stat.})^{+0.22}_{-0.22}\ (\text{syst.}).$$

The measured Wilson coefficients are in agreement with the SM. It is the first measurement where c_{tW}, c_{itW} and c_{qQ} are measured simultaneously. The measurement is dominated by uncertainties on the reconstruction of jets, as well as uncertainties from the modeling of top quark processes. The precision in which the coefficients are measured could be improved by new analysis techniques for estimating these dominant uncertainties.

Additional studies are performed on several assumptions in the EFT fit model used in the fitting procedure. The impact on including an EFT parameterisation of the $t\bar{t}$ process is found to be very small for this measurement. The limits obtained from a fit including only linear terms of the coefficients are also studied. They are very close to the results including a quadratic dependence, suggesting that for these operators the EFT expansion converges fairly quickly.

This result is the most stringent limit on c_{tW} and c_{itW} from high-energy experiments and significantly improves the previous t-channel single top production analysis performed by ATLAS [81].

Summary

Spinning tops, A search for new physics in t-channel single top quark production with the ATLAS detector at the LHC

Understanding the fundamental building blocks of the universe has been an everlasting fascination of mankind. Already in ancient times the idea existed that there is a limited number of elementary particles. Nowadays, particle physics is the field of study investigating these fundamental building blocks and how they interact with another. The model that describes the interactions of fundamental particles is the Standard Model (SM). The SM accommodates three generations of quarks and leptons, resulting in a total of 12 fermions that make up the visible matter in the universe. The forces between the particles are governed by the exchange of four fundamental bosons. The Higgs boson is the most recently observed particle. It was predicted by the Brout-Englert-Higgs mechanism endowing fundamental particles with their mass. The observation of the Higgs boson completed the SM.

In the SM, each of the elementary particles has a corresponding antiparticle with opposite (electric) charge. To a very large extent, particles and antiparticles behave fundamentally in the same way: in interactions an equal amount of particle and antiparticles (dis-)appear. A different behaviour of particles and antiparticles is known as Charge-Parity (CP) violation. There are very subtle deviations observed and mostly CP violation in b-quark interactions is still studied in dedicated experiments. However, these small deviations cannot explain the abundance of matter in the universe today. This motivates the analysis described in this thesis, the hunt for CP violation at the highest energy scale using the heaviest particle as a probe: the top quark.

This work searches for new physics in electroweak interactions of the top quark. In weak interactions a W-boson couples to a b-quark, producing a top quark. The process with the largest cross-section where top quarks are produced via a weak interaction is the t-channel production mechanism, which is studied in this thesis. A Feynman diagram of the t-channel interaction is shown in fig. 9.1. Top quarks are produced with their spin polarised in this channel due to the nature of weak interactions. The spin properties of the top quarks are a probe to search for new (CP-violating) interactions. They are transferred to the decay products of the top quark, allowing to study the spin of the top quark via the angular distributions of these decay products. The produced top quark decays almost instantly into a b-quark and a W-boson. This thesis focuses on the subsequent leptonic decays of the W-boson to an electron or muon with its corresponding antineutrino. The angular distribution of the charged lepton is used to search for new interactions.

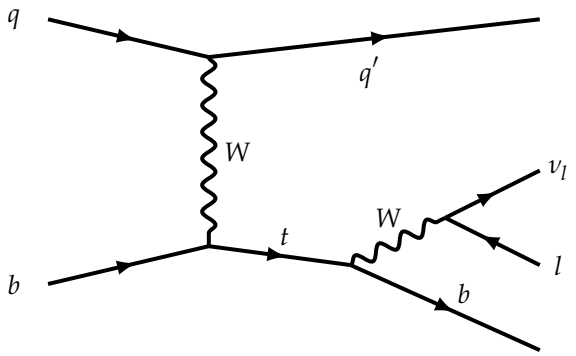

Figure 9.1: The Feynman diagram of t-channel single top production. The top quark decays into a b-quark and W-boson. In this example the W-boson decays leptonically.

Extensions to the Standard Model

The SM is a very successful theory, capable of describing a plethora of interactions that are confirmed by experimental observations. However, it can not be the "theory of everything" as it can not explain all observations in nature. It does not incorporate gravity, it can not explain the observation of dark-matter and as already mentioned before cannot explain the observed imbalance between matter and antimatter in the universe. This suggests that the SM is an approximation of a more fundamental theory of nature. Finding a theory that is able to explain all observations is the ultimate goal of fundamental particle physics.

New theories typically predict new particles that can be searched for in experiments. Such particles have not been discovered and are hiding at energies out of the range of current experiments. Therefore an indirect approach is adopted. The quantum nature of the universe allows for interfence between possible high mass force-particles and the already known SM particles, which leads to subtle deviations to processes at a lower energy scale in reach of current experiments. By precisely measuring the features of particle collisions in the current energy domain, new phenomena can be indirectly measured. To describe possible deviations, the SM is systematically expanded by higher order interaction terms. This approach is known as the Standard Model Effective Field Theory (SMEFT) approach. This framework allows to make quantitative predictions for observable interactions, without knowing the exact nature of the new physics.

This thesis measures the SMEFT operators affecting the t-channel production process of top quarks. One SMEFT interaction changing this process is the O_{tW} interaction. This new interaction produces, contrary to the left-handed SM interaction, a

right-handed top quark. The size of these effects are parameterised by a real (c_{tW}) and imaginary (c_{itW}) coefficient, which correspond to a new CP-converving and CP-violating interaction respectively. A non-zero value of c_{itW} could hint to a solution for the matter antimatter asymmetry. The previous measurement of the CP-violating coefficient was measured to $c_{itW} = -0.3 \pm 0.2$ showing a non-conclusive but interesting tension of almost 2-sigma with respect to the SM.

The second SMEFT interaction that alters the weak interaction of top quarks is incorporated via c_{qQ}. This term changes the momentum spectrum of the produced top quarks. Searching for new physics using SMEFT and extract the values of the EFT coefficients c_{tW}, c_{itW} and c_{qQ} is the main focus of this thesis.

Searching for new top interactions

To search for these new interactions, top quarks have to be produced in a controlled environment. The only machine capable of producing top quarks at the writing of this thesis is the Large Hadron Collider located at the European particle physics laboratory CERN. This thesis uses the data collected by the ATLAS experiment during the Run 2 period to study high energetic particle collisions involving the top quark.

Angular distributions between the top decay products are known to be sensitive for measuring the EFT coefficients c_{tW} and c_{itW}. In particular the three polarisation angles show a strong dependency on these two coefficients. These angles are defined in the top rest system, by constructing a three-dimensional system using the momentum of the associated jet, $\vec{p}_j$, and the incoming light quark, $\vec{p}_q$, as a reference:

$$\hat{z} = \frac{\vec{p}_j}{|\vec{p}_j|}, \qquad \hat{y} = \frac{\vec{p}_j \times \vec{p}_q}{|\vec{p}_j \times \vec{p}_q|}, \qquad \hat{x} = \hat{y} \times \hat{z}. \tag{9.1}$$

The angles between these three directions and the charged lepton are defined as the polarisation angles. The top transverse momentum on the other hand is sensitive to c_{qQ}. To frame all the information in a single (multidimensional) distribution with a reasonable number of bins, an observable, O(16), is constructed. This observable divides the p_{T} distribution of the top quark in two bins, $p_{\mathrm{T}}(\mathrm{top}) < 80\,\mathrm{GeV}$ and $p_{\mathrm{T}}(\mathrm{top}) > 80\,\mathrm{GeV}$ respectively. Together with asymmetries in the polarisation angles $\cos\theta_{\ell x}$, $\cos\theta_{\ell y}$ and $\cos\theta_{\ell z}$ the observable O(16) is defined as follows:

$$\begin{aligned} bin(O(16)) = &(\cos\theta_{\ell y} > 0) \\ &+ 2(\cos\theta_{\ell x} > 0) \\ &+ 4(\cos\theta_{\ell z} > 0) \\ &+ 8(p_{\mathrm{T}}(\mathrm{top}) > 80\,\mathrm{GeV}). \end{aligned} \tag{9.2}$$

This observable is used to measure the EFT coefficients in the signal region (SR) from data. The dependency to the different EFT coefficients is shown in fig. 9.2. The different shape of this distribution for the three different EFT coefficients allows to

measure them simultaneously in data.

In these collisions, however, both genuine t-channel single top interactions and processes resembling t-channel single top production interactions are produced. It is crucial to separate events with top quarks produced in t-channel interactions from the background processes. This is done by selecting events with exactly one electron or muon and two jets, where one jet is tagged as a b-jet. These events are further reconstructed, and dedicated event features are used to separate signal and background contributions. Furthermore, in this work for the first time, a kinematic fit has been implemented to further reduce contributions of poorly reconstructed events.

The values of the coefficients are determined using a binned profile likelihood fit of the O(16) observable to data collected by the ATLAS experiment. In this fit both the t-channel single top production process and events produced via the $t\bar{t}$ process are parameterised by EFT coefficients. This is a novelty to previous fits where the background was treated as SM. The measured values of the EFT coefficients are:

$$
\begin{aligned}
c_{tW} &= 0.11^{+0.06}_{-0.06}\ (\text{stat.})^{+0.22}_{-0.22}\ (\text{syst.}),\\
c_{itW} &= 0.03^{+0.05}_{-0.05}\ (\text{stat.})^{+0.07}_{-0.07}\ (\text{syst.}),\\
c_{qQ} &= 0.18^{+0.05}_{-0.05}\ (\text{stat.})^{+0.22}_{-0.22}\ (\text{syst.}).
\end{aligned}
$$

All three coefficients agree with the SM within their respective 68 % confidence level interval. The measurement is limited by systematic uncertainties from both the reconstruction of jets and uncertainties on the modelling of the top processes. The fitted distribution including all backgrounds is shown in fig. 9.3. A good agreement with the observed data is observed. It is the first time that c_{tW}, c_{itW} and c_{qQ} are measured simultaneously and this measurement gives the most stringent limits on c_{itW} from high energy particle collisions. This measurement supersedes the previous measurement and implies that there is no CP-violating interaction in single top quark production with the current sensitivity.

Future improvements

No clear signs of new particle interactions are observed by this analysis, however this does not mean that there are none. Improvements in the reconstruction of jets and the modelling of the top processes could increase the precision and reveal new interactions in this channel. The LHC currently only collected a fraction of the total luminosity. Future runs will increase the dataset by a factor 20 which allows to measure the top quark in more and more details. It allows for a precise study of the currently poorly populated "tails" of many distributions, which show a high potential to find new interactions. Exploring these phase-spaces, gaining more and more sensitivity to find new physics interactions, will be key to the future LHC physics program and solving the mysteries of our universe.

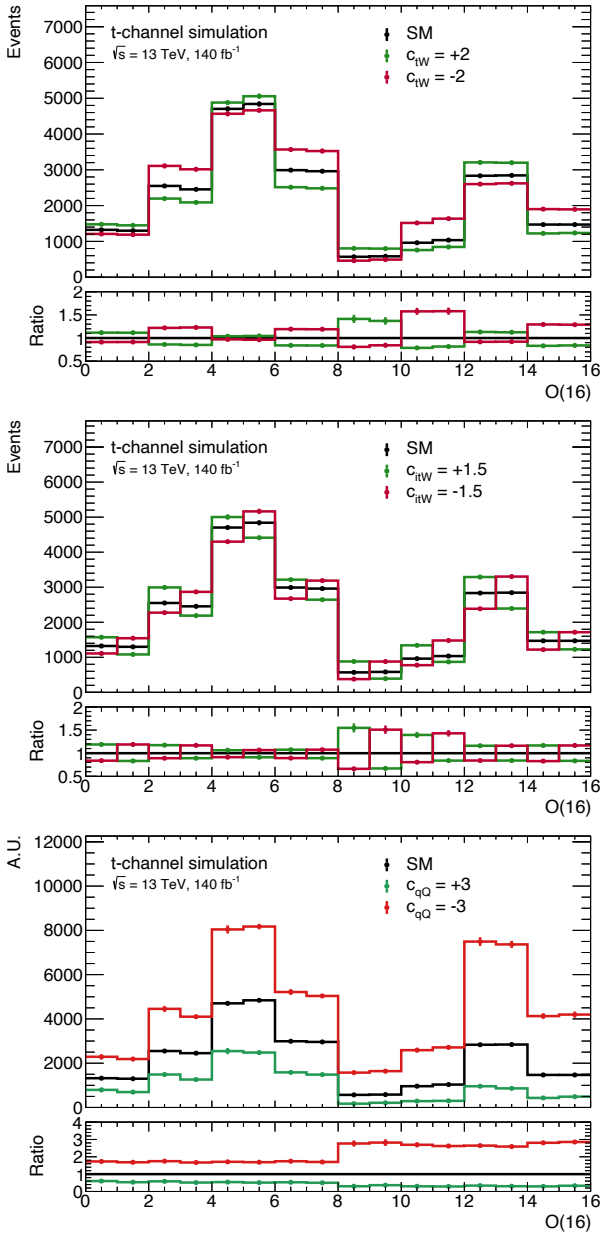

Figure 9.2: Dependence of the observable $O(16)$ as defined in eq. (5.5) on c_{tW} (top), c_{itW} (middle) and c_{qQ} (bottom). The lower panel shows the ratio with respect to the SM.

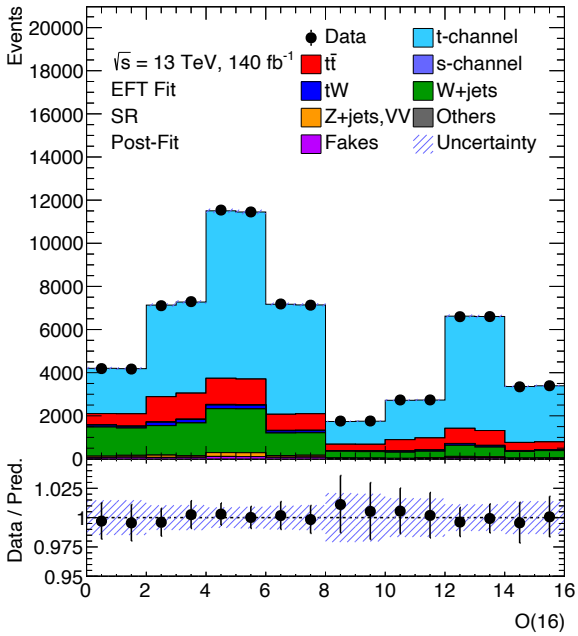

Figure 9.3: Postfit distribution of the O(16) observable. The observed distribution (dots) is compared with the expected distribution (histograms) where all parameters are set to their values after performing the fit. In the distribution the t-channel contribution is stacked upon the contribution from all considered background processes. The lower panel shows the ratio of data to the prediction in each bin. The shaded uncertainty band includes the uncertainty from systematic sources and from limited Monte Carlo statistics.

Samenvatting

Spinning tops, een zoektocht naar nieuwe fysica in de productie van top quarks in het t-kanaal met het ATLAS experiment bij de LHC

Het begrijpen van de meest fundamentele bouwstenen van de natuur is al sinds de oudheid een fascinatie van de mensheid. Al in de oudheid bestond er het idee dat er elementaire deeltjes zijn waar alle materie uit is opgebouwd. Elementaire deeltjes fysica is het tegenwoordige vakgebied dat onderzoek doet naar deze fundamentele bouwstenen en hun wisselwerkingen. Het model dat de wisselwerkingen tussen de fundamentele deeltjes beschrijft, is het Standard Model (SM). Het SM bestaat uit drie generaties van quarks en leptonen, resulterend in 12 fermions die verantwoordelijk zijn voor de zichtbare materie in ons universum. De krachten tussen deze elementaire deeltjes worden beschreven door uitwisselingen van vier fundamentele bosons. Het Higgs deeltje is het meest recent geobserveerde deeltje. Het was voorspeld in het Brout-Englert-Higgs mechanisme dat fundamentele deeltjes massa geeft. De observatie van het Higgs boson voltooit het SM.

In het SM heeft elk elementair deeltje een corresponderend antideeltje met tegenovergestelde (elektrische) lading. Tot op zekere hoogte gedragen deeltjes en antideeltjes zich hetzelfde: in wisselwerkingen ontstaan en verdwijnen er evenveel deeltjes als antideeltjes. Het verschijnsel waar deeltjes zich anders gedragen dan antideeltjes heet "Charge-Parity"(CP) schending. Zeer subtiele CP schendende processen zijn geobserveerd in de natuur en voornamelijk CP schendende b-quark wisselwerkingen worden bestudeerd in toegewijde experimenten. Maar, de hoeveelheid aan CP schendende wisselwerkingen kan de overvloed aan materie die is geobserveerd in het zichtbare universum niet verklaren. Dit motiveert de analyse beschreven in dit proefschrift, de zoektocht naar nieuwe CP schendende wisselwerkingen met als instrument het elementaire deeltje met de hoogste massa, de top quark.

Dit werk zoekt naar nieuwe fysica in elektrozwakke wisselwerkingen van top quarks. In deze zwakke wisselwerking koppelt een W-boson aan een b-quark waarbij een top quark ontstaat. Het proces met de hoogste cross-sectie waar top quarks worden geproduceerd via een elektrozwakke wisselwerking, is het t-kanaal, dat daarom gebruikt wordt in deze studie. Bij een top productie in het t-kanaal wordt een virtueel W boson uitgewisseld tussen de inkomende deeltjes. Een Feynman diagram van de top wisselwerking in het t-kanaal is weergegeven in figuur 10.4.

Vanwege de aard van zwakke interacties worden top quarks met een bepaalde voorkeursrichting van hun spin geproduceerd. Het geproduceerde top quark vervalt bijna instantaan in een b-quark en een W-boson. Hierdoor wordt de spin informatie doorgegeven aan de vervalsproducten en is dit een unieke probe om te zoeken naar nieuwe (CP schendende) wisselwerkingen. Dit proefschrift legt de focus op de leptonische vervalmodus, waar het W-boson vervalt in een elektron of een muon

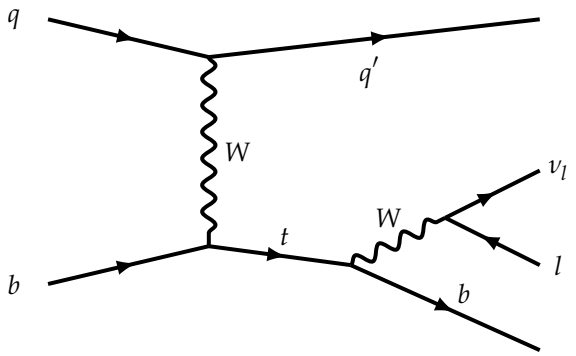

Figuur 10.4: Het Feynman diagram van een t-kanaal top wisselwerking. Het top quark vervalt in een *b*-quark en een *W*-boson. In dit voorbeeld vervalt het *W*-boson leptonisch.

met bijbehorend antineutrino. De hoekverdeling van de geladen leptonen worden gebruikt om te zoeken naar nieuwe wisselwerkingen.

Uitbreidingen van het Standaard Model

Het SM is een zeer succesvolle theorie dat talrijke wisselwerkingen kan beschrijven die zijn bevestigd door tal van experimentele observaties. Desalniettemin, is het niet de ”theorie van alles” omdat het niet alle observaties in de natuur kan verklaren. Het omvat geen zwaartekracht, het heeft geen verklaring voor de geobserveerde donkere materie en kan zoals al eerder genoemd niet de overvloed aan materie ten opzichte van antimaterie verklaren. Dit suggereert dat het SM een benadering is van een meer fundamentele theorie. Het vinden van deze theorie dat al deze observaties kan verklaren is het ultieme doel van elementaire deeltjes fysica.

Nieuwe theorieën kunnen nieuwe deeltjes voorspellen waarna gezocht kan worden in experimenten. Deze deeltjes zijn tot dusver niet geobserveerd en momenteel is de energie van deeltjesversnellers dus buiten het bereik om deze nieuwe deeltjes te vinden. Daarom is er in deze thesis gekozen voor een indirecte aanpak. De quantumwereld staat interferentie tussen mogelijke nieuwe deeltjes en de SM-deeltjes toe. Dit leidt tot subtiele, maar meetbare, afwijkingen van interacties die men kan meten met de huidige experimenten. Door zeer precies de botsingen tussen de elementaire deeltjes te onderzoeken is het dus mogelijk om nieuwe fysica indirect te vinden. Deze nieuwe fysica is beschreven door het SM systematisch uit te breiden met nieuwe, hogere orde, wisselwerkingstermen. Deze methode heet Standard Model Effective Field Theory (SMEFT). In dit framework kunnen kwantitatieve voorspellingen worden gedaan zonder dat men de aard van de onderliggende theorie weet.

De in dit proefschrift beschreven analyse richt zich op SMEFT operatoren die de productie van top quarks in het t-kanaal beïnvloeden. Eén van de SMEFT wisselwerkingen die dit proces veranderd is de O_{tW} operator. Deze nieuwe wisselwerking produceert, in tegenstelling tot het SM, rechts-handige top quarks. De sterkte van dit effect wordt geparameteriseerd door een reëele koppelingsparameter c_{tW} en een imaginaire coëfficiënt c_{itW}, corresponderend aan een CP behoudende en een CP schendende wisselwerking. Een waarde anders dan nul voor c_{itW} zou dus een verklaring kunnen geven voor de overvloed aan materie in ons universum. De voorafgaande meting van deze CP schendende coëfficiënt resulteerde in een waarde van $c_{itW} = -0.3 \pm 0.2$. Een afwijking van bijna 2-sigma met het SM.

De tweede SMEFT wisselwerking die de zwakke wisselwerkingen van top quarks beïnvloedt is de $O_{qQ}^{3,1}$ operator. Deze term verandert het impulsspectrum van de geproduceerde top quarks. De zoektocht naar nieuwe fysica en de meting van de drie EFT coëfficiënten c_{tW}, c_{itW} en c_{qQ} wordt beschreven in dit proefschrift.

De zoektocht naar nieuwe top wisselwerkingen

Om de nieuwe interacties te meten moeten top quarks worden geproduceerd in een gecontroleerde omgeving. Op het moment dat dit proefschrift is geschreven is de Large Hadron Collider (LHC), gelegen op het terrein van CERN, de enige machine die in staat is om top quarks te produceren. Dit werk onderzoekt deeltjesbotsingen waarbij top quarks ontstaan in de Run 2 dataset van het ATLAS experiment.

Hoekdistributies tussen de top vervalsproducten van de geproduceerde top quarks zijn observabelen die gevoelig zijn voor de effecten van de EFT coëfficiënten c_{tW} en c_{itW}. In het bijzonder de drie polarisatie hoeken. Deze hoeken zijn gedefinieerd in het rustsysteem van het top quark. Gebruikmakend van de inkomende lichte quark, $\vec{p}_q$, en de geproduceerde lichte jet, $\vec{p}_j$, kan men een drie-dimensionaal systeem construeren:

$$\hat{z} = \frac{\vec{p}_j}{|\vec{p}_j|}, \qquad \hat{y} = \frac{\vec{p}_j \times \vec{p}_q}{|\vec{p}_j \times \vec{p}_q|}, \qquad \hat{x} = \hat{y} \times \hat{z}. \tag{10.3}$$

De hoeken tussen deze drie richtingen en het geladen lepton zijn de polarisatie hoeken. De transversale impuls van het top quark is daarentegen gevoelig voor effecten van c_{qQ}. Om al deze informatie in een enkele (multidimensionale) distributie te vangen met een beperkt aantal bins is een nieuwe observabele, O(16), ontworpen. Deze observable splitst de transversale impuls van het top quark in twee bins met $p_{\mathrm{T}}(\mathrm{top}) < 80\,\mathrm{GeV}$ en $p_{\mathrm{T}}(\mathrm{top}) > 80\,\mathrm{GeV}$. Samen met asymmetrieën in de drie polarisatiehoeken $\cos\theta_{\ell x}$, $\cos\theta_{\ell y}$ en $\cos\theta_{\ell z}$ is de observabele O(16) gedefinieerd als:

$$
\begin{aligned}
bin(O(16)) = &(\cos\theta_{\ell y} > 0) \\
&+ 2(\cos\theta_{\ell x} > 0) \\
&+ 4(\cos\theta_{\ell z} > 0) \\
&+ 8(p_{\mathrm{T}}(\mathrm{top}) > 80\,\mathrm{GeV}).
\end{aligned}
\tag{10.4}
$$

Deze observabele wordt gebruikt om de EFT coëfficiënten in een signaalregio (SR) te meten in data. De afhankelijkheid van de verschillende EFT coëfficiënten wordt getoond in figuur 10.5. De verschillende effecten ten gevolge van de drie coëfficiënten zorgen ervoor dat deze alledrie tegelijkertijd gemeten kunnen worden in de dataset.

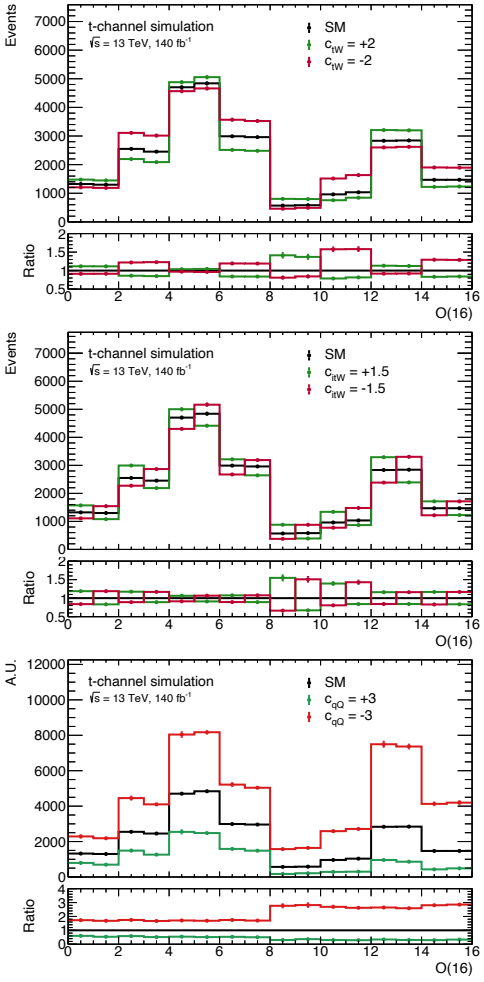

Figuur 10.5: Afhankelijkheid van de observabele O(16) gedefinieerd in vergelijking 10.4 ten opzichte van c_{tW} (boven), c_{itW} (midden) en c_{qQ} (onder). Het onderste paneel laat steeds de verhouding met de SM-verwachting zien.

De geanalyseerde dataset omvat echter zowel botsingen waarin top quarks daadwerkelijk zijn geproduceerd via een t-kanaal wisselwerking, als ook botsingen die lijken op een t-kanaal top wisselwerking. Het is uiterst belangrijk om top quark t-kanaal interacties te scheiden van deze achtergronden. Dit wordt gerealiseerd door botsingen te selecteren waarbij precies één elektron of één muon tegelijkertijd wordt gedetecteerd met twee jets. Hierbij is een van de twee jets gelabeld als een b-jet. Deze gebeurtenissen worden gereconstrueerd en kinematische eigenschappen van deze botsing worden gebruikt om het signaal verder te scheiden van de achtergronden. Verder wordt er in dit werk voor het eerst een zogenaamde "kinematische fit"gebruikt om botsingen die slecht zijn gereconstrueerd te verwerpen.

De waardes van de coëfficiënten worden gemeten via een profile likelihood fit aan de O(16) observabele in data van het ATLAS experiment. In deze fit wordt zowel de productie van top quarks via het t-kanaal als ook het effect op een van de achtergronden, het $t\bar{t}$ process, geparameteriseerd door de EFT coëfficiënten. Dit is nieuw ten opzichte van eerdere metingen waar de achtergrond wordt behandeld als zijnde SM. De gemeten waardes van de EFT coëfficiënten zijn:

$$
\begin{aligned}
c_{tW} &= 0.11^{+0.06}_{-0.06}\ (\text{stat.})^{+0.22}_{-0.22}\ (\text{syst.}),\\
c_{itW} &= 0.03^{+0.05}_{-0.05}\ (\text{stat.})^{+0.07}_{-0.07}\ (\text{syst.}),\\
c_{qQ} &= 0.18^{+0.05}_{-0.05}\ (\text{stat.})^{+0.22}_{-0.22}\ (\text{syst.}).
\end{aligned}
$$

Alledrie de coëfficiënten zijn in overeenstemming met de SM waarde van nul binnen het 68 % betrouwbaarheidsinterval. Deze meting is gelimiteerd door de systematische onzekerheden van de reconstructie van jets en het modelleren van de top processen. In figuur 10.6 wordt de distributie van O(16) getoond voor zowel data en de gefitte combinatie van signaal en de verschillende achtergronden. De data en de gefitte distributie zijn in goede overeenstemming. Dit is de eerste keer dat zowel c_{tW}, c_{itW} en c_{qQ} tegelijkertijd gemeten zijn, leidend tot de sterkste limieten op c_{itW} gemeten in hoog energetische deeltjesbotsingen. Dit resultaat vervangt de voorafgaande meting, en impliceert dat binnen de gevoeligheid er geen CP schendende wisselwerking in top quarks is.

Toekomstige verbeteringen

Er zijn geen nieuwe wisselwerkingen tussen deeltjes waargenomen in deze analyse. Dit betekent echter niet dat deze er niet zijn. Verbeteringen in de reconstructie van jets en het modelleren van de top processen kunnen de precisie verbeteren en nieuwe wisselwerkingen in dit kanaal blootleggen. De LHC heeft pas een fractie van de geplande botsingen gemeten. Toekomstige runs zullen de dataset met een factor 20 vergroten, waardoor het top quark met steeds meer precisie bestudeerd kan worden. Hierdoor kunnen zelfs de op het moment amper gevulde staarten van distributies bestudeerd worden. Deze staarten hebben een hoge gevoeligheid voor nieuwe wisselwerkingen. Onderzoek naar deze faseruimte zal één van de essentiële metingen

zijn in de toekomst van de LHC.

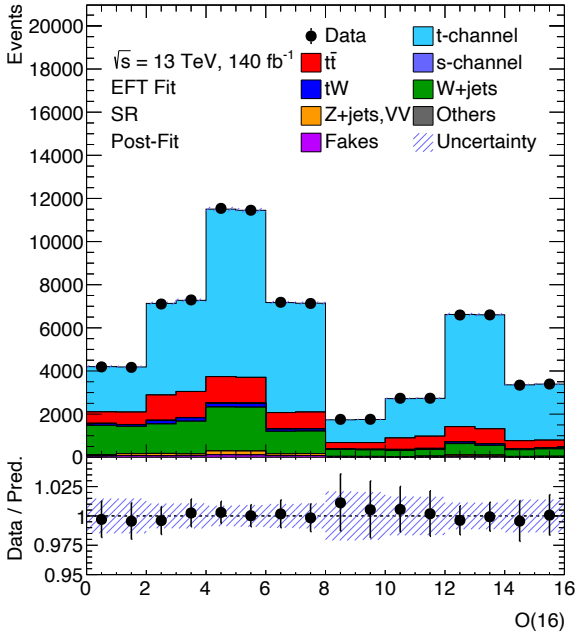

Figuur 10.6: Postfit distributie van observabele O(16). De geobserveerde distributie (punten) wordt vergeleken met de verwachte distributie (histogrammen) waar de waarde van alle parameters correspondeert met die na de fit. Het onderste paneel laat de ratio tussen data en de verwachte distributie zien. De gekleurde onzekerheidsband laat de systematische onzerkerheden zien.

Bibliography

[1] M. Thomson, "Modern particle physics". Cambridge University Press, New York, 2013.

[2] D. J. Griffiths, "Introduction to elementary particles; 2nd rev. version". Physics textbook. Wiley, New York, NY, 2008.

[3] F. Halzen and A. D. Martin, "QUARKS AND LEPTONS: AN INTRODUCTORY COURSE IN MODERN PARTICLE PHYSICS". 1984.

[4] M. E. Peskin and D. V. Schroeder, "An introduction to quantum field theory". Westview, Boulder, CO, 1995. Includes exercises.

[5] CMS Collaboration, "Observation of a new boson at a mass of 125 GeV with the CMS experiment at the LHC", *Phys. Lett.* **B716** (2012) 30–61, doi:10.1016/j.physletb.2012.08.021, arXiv:1207.7235.

[6] ATLAS Collaboration, "Observation of a new particle in the search for the Standard Model Higgs boson with the ATLAS detector at the LHC", *Phys. Lett. B* **716** (2012) 1–29, doi:10.1016/j.physletb.2012.08.020, arXiv:1207.7214.

[7] P. W. Higgs, "Broken Symmetries and the Masses of Gauge Bosons", *Phys. Rev. Lett.* **13** (Oct, 1964) 508–509, doi:10.1103/PhysRevLett.13.508.

[8] P. W. Higgs, "Spontaneous Symmetry Breakdown without Massless Bosons", *Phys. Rev.* **145** (1966) 1156–1163, doi:10.1103/PhysRev.145.1156.

[9] F. Englert and R. Brout, "Broken Symmetry and the Mass of Gauge Vector Mesons", *Phys. Rev. Lett.* **13** (Aug, 1964) 321–323, doi:10.1103/PhysRevLett.13.321.

[10] I. Neutelings. https://tikz.net/sm_particles/.

[11] S. L. Glashow, "Partial Symmetries of Weak Interactions", *Nucl. Phys.* **22** (1961) 579–588, doi:10.1016/0029-5582(61)90469-2.

[12] A. Salam, "Weak and Electromagnetic Interactions", *Conf. Proc.* **C680519** (1968) 367–377.

[13] S. Weinberg, "A Model of Leptons", *Phys. Rev. Lett.* **19** (1967) 1264–1266, doi:10.1103/PhysRevLett.19.1264.

[14] C. S. Wu et al., "Experimental Test of Parity Conservation in Beta Decay", *Phys. Rev.* **105** (Feb, 1957) 1413–1415, doi:10.1103/PhysRev.105.1413.

[15] N. Cabibbo, "Unitary Symmetry and Leptonic Decays", *Phys. Rev. Lett.* **10** (Jun, 1963) 531–533, doi:10.1103/PhysRevLett.10.531.

[16] M. Kobayashi and T. Maskawa, "CP Violation in the Renormalizable Theory of Weak Interaction", *Prog. Theor. Phys.* **49** (1973) 652–657, doi:10.1143/PTP.49.652.

[17] B. Pontecorvo, "Inverse beta processes and nonconservation of lepton charge", *Zh. Eksp. Teor. Fiz.* **34** (1957) 247.

[18] Z. Maki, M. Nakagawa, and S. Sakata, "Remarks on the unified model of elementary particles", *Prog. Theor. Phys.* **28** (1962) 870–880, doi:10.1143/PTP.28.870.

[19] S. Abachi et al., "Observation of the Top Quark", *Physical Review Letters* **74** (apr, 1995) 2632–2637, doi:10.1103/physrevlett.74.2632.

[20] CDF Collaboration, "Observation of top quark production in $\bar{p}p$ collisions", *Phys. Rev. Lett.* **74** (1995) 2626–2631, doi:10.1103/PhysRevLett.74.2626, arXiv:hep-ex/9503002.

[21] Particle Data Group Collaboration, "Review of Particle Physics", *PTEP* **2022** (2022) 083C01, doi:10.1093/ptep/ptac097.

[22] ATLAS Collaboration, "Top cross section summary plots - June 2023", technical report, CERN, Geneva, 2023. All figures including auxiliary figures are available at https://atlas.web.cern.ch/Atlas/GROUPS/PHYSICS/PUBNOTES/ATL-PHYS-PUB-2023-014.

[23] G. Mahlon and S. Parke, "Single top quark production at the LHC: Understanding spin", *Physics Letters B* **476** (mar, 2000) 323–330, doi:10.1016/s0370-2693(00)00149-0.

[24] A. Czarnecki, J. G. Körner, and J. H. Piclum, "Helicity fractions of W bosons from top quark decays at next-to-next-to-leading order in QCD", *Phys. Rev. D* **81** (Jun, 2010) 111503, doi:10.1103/PhysRevD.81.111503.

[25] G. Mahlon and S. Parke, "Improved spin basis for angular correlation studies in single top quark production at the Fermilab Tevatron", *Physical Review D* **55** (jun, 1997) 7249–7254, doi:10.1103/physrevd.55.7249.

[26] G. Mahlon, "Observing Spin Correlations in Single Top Production and Decay", 2000.

[27] J. A. Aguilar-Saavedra and S. Amor dos Santos, "New directions for top quark polarization in the t-channel process", *Phys. Rev. D* **89** (Jun, 2014) 114009, doi:10.1103/PhysRevD.89.114009.

[28] J. Aguilar-Saavedra and J. Bernab'eu, "W polarisation beyond helicity fractions in top quark decays", *Nuclear Physics B* **840** (05, 2010) 349–378, doi:10.1016/j.nuclphysb.2010.07.012.

[29] ATLAS Collaboration, "Measurement of the polarisation of W bosons produced in top-quark decays using dilepton events at s=13 TeV with the

ATLAS experiment", *Phys. Lett. B* **843** (2023) 137829, doi:10.1016/j.physletb.2023.137829, arXiv:2209.14903.

[30] A. D. Sakharov, "Violation of CP invariance, C asymmetry, and baryon asymmetry of the universe", *Soviet Physics Uspekhi* **34** (may, 1991) 392, doi:10.1070/PU1991v034n05ABEH002497.

[31] M. de Beurs, E. Laenen, M. Vreeswijk, and E. Vryonidou, "Effective operators in t-channel single top production and decay", *Eur. Phys. J. C* **78** (2018), no. 11, 919, doi:10.1140/epjc/s10052-018-6399-3, arXiv:1807.03576.

[32] J. C. Collins, D. E. Soper, and G. F. Sterman, "Factorization of Hard Processes in QCD", *Adv. Ser. Direct. High Energy Phys.* **5** (1989) 1–91, doi:10.1142/9789814503266_0001, arXiv:hep-ph/0409313.

[33] Y. L. Dokshitzer, "Calculation of the Structure Functions for Deep Inelastic Scattering and e+ e- Annihilation by Perturbation Theory in Quantum Chromodynamics.", *Sov. Phys. JETP* **46** (1977) 641–653.

[34] V. N. Gribov and L. N. Lipatov, "Deep inelastic e p scattering in perturbation theory", *Sov. J. Nucl. Phys.* **15** (1972) 438–450.

[35] G. Altarelli and G. Parisi, "Asymptotic freedom in parton language", *Nuclear Physics B* **126** (1977), no. 2, 298–318, doi:https://doi.org/10.1016/0550-3213(77)90384-4.

[36] NNPDF Collaboration, "An open-source machine learning framework for global analyses of parton distributions", *Eur. Phys. J. C* **81** (2021), no. 10, 958, doi:10.1140/epjc/s10052-021-09747-9, arXiv:2109.02671.

[37] NNPDF Collaboration, "Parton distributions for the LHC Run II", *JHEP* **04** (2015) 040, doi:10.1007/JHEP04(2015)040, arXiv:1410.8849.

[38] R. D. Ball et al., "Parton distributions with LHC data", *Nucl. Phys. B* **867** (2013) 244–289, doi:10.1016/j.nuclphysb.2012.10.003, arXiv:1207.1303.

[39] L. Harland-Lang, A. Martin, P. Motylinski, and R. Thorne, "Parton distributions in the LHC era: MMHT 2014 PDFs", *The European Physical Journal C* **75** (12, 2014) doi:10.1140/epjc/s10052-015-3397-6.

[40] G. 't Hooft and M. Veltman, "Regularization and renormalization of gauge fields", *Nuclear Physics B* **44** (1972), no. 1, 189–213, doi:https://doi.org/10.1016/0550-3213(72)90279-9.

[41] K. Khelifa-Kerfa, "QCD resummation for high-p_T jet shapes at hadron colliders", 2021.

[42] J. Alwall et al., "The automated computation of tree-level and next-to-leading order differential cross sections, and their matching to parton shower simulations", *JHEP* **07** (2014) 079, doi:10.1007/JHEP07(2014)079,

arXiv:1405.0301.

[43] R. Frederix et al., "The automation of next-to-leading order electroweak calculations", *JHEP* **07** (2018) 185, doi:10.1007/JHEP11(2021)085, arXiv:1804.10017. [Erratum: JHEP 11, 085 (2021)].

[44] P. Nason, "A New method for combining NLO QCD with shower Monte Carlo algorithms", *JHEP* **11** (2004) 040, doi:10.1088/1126-6708/2004/11/040, arXiv:hep-ph/0409146.

[45] S. Frixione, P. Nason, and C. Oleari, "Matching NLO QCD computations with Parton Shower simulations: the POWHEG method", *JHEP* **11** (2007) 070, doi:10.1088/1126-6708/2007/11/070, arXiv:0709.2092.

[46] S. Alioli, P. Nason, C. Oleari, and E. Re, "A general framework for implementing NLO calculations in shower Monte Carlo programs: the POWHEG BOX", *JHEP* **06** (2010) 043, doi:10.1007/JHEP06(2010)043, arXiv:1002.2581.

[47] Sherpa Collaboration, "Event Generation with Sherpa 2.2", *SciPost Phys.* **7** (2019), no. 3, 034, doi:10.21468/SciPostPhys.7.3.034, arXiv:1905.09127.

[48] S. Catani and M. H. Seymour, "A General algorithm for calculating jet cross-sections in NLO QCD", *Nucl. Phys. B* **485** (1997) 291–419, doi:10.1016/S0550-3213(96)00589-5, arXiv:hep-ph/9605323. [Erratum: Nucl.Phys.B 510, 503–504 (1998)].

[49] S. Catani, S. Dittmaier, M. H. Seymour, and Z. Trocsanyi, "The Dipole formalism for next-to-leading order QCD calculations with massive partons", *Nucl. Phys. B* **627** (2002) 189–265, doi:10.1016/S0550-3213(02)00098-6, arXiv:hep-ph/0201036.

[50] C. Bierlich et al., "A comprehensive guide to the physics and usage of PYTHIA 8.3", doi:10.21468/SciPostPhysCodeb.8, arXiv:2203.11601.

[51] "ATLAS Pythia 8 tunes to 7 TeV data", technical report, CERN, Geneva, 2014. All figures including auxiliary figures are available at https://atlas.web.cern.ch/Atlas/GROUPS/PHYSICS/PUBNOTES/ATL-PHYS-PUB-2014-021.

[52] M. Bahr et al., "Herwig++ Physics and Manual", *Eur. Phys. J. C* **58** (2008) 639–707, doi:10.1140/epjc/s10052-008-0798-9, arXiv:0803.0883.

[53] J. Bellm et al., "Herwig 7.0/Herwig++ 3.0 release note", *Eur. Phys. J. C* **76** (2016), no. 4, 196, doi:10.1140/epjc/s10052-016-4018-8, arXiv:1512.01178.

[54] P. Artoisenet, R. Frederix, O. Mattelaer, and R. Rietkerk, "Automatic

spin-entangled decays of heavy resonances in Monte Carlo simulations", *JHEP* **03** (2013) 015, doi:10.1007/JHEP03(2013)015, arXiv:1212.3460.

[55] D. J. Lange, "The EvtGen particle decay simulation package", *Nucl. Instrum. Meth. A* **462** (2001) 152–155, doi:10.1016/S0168-9002(01)00089-4.

[56] O. Bruning, H. Burkhardt, and S. Myers, "The Large Hadron Collider", *Prog. Part. Nucl. Phys.* **67** (2012) 705–734, doi:10.1016/j.ppnp.2012.03.001.

[57] G. Bachy et al., "The LEP collider: construction, project status and outlook", *Part. Accel.* **26** (1990) 19–32.

[58] ATLAS Collaboration, "The ATLAS Experiment at the CERN Large Hadron Collider", *JINST* **3** (2008) S08003, doi:10.1088/1748-0221/3/08/S08003.

[59] CMS Collaboration, "The CMS Experiment at the CERN LHC", *JINST* **3** (2008) S08004, doi:10.1088/1748-0221/3/08/S08004.

[60] ALICE Collaboration, "ALICE", *PoS* **EPS-HEP2009** (2009) 027, doi:10.22323/1.084.0027.

[61] LHCb Collaboration, V. Gibson, "The LHCb experiment", in *22nd Lake Louise Winter Institute: Fundamental Interactions*, pp. 60–79. 2007. doi:10.1142/9789812776105_0003.

[62] C. Lefèvre, "The CERN accelerator complex. Complexe des accélérateurs du CERN", (2008).

[63] ATLAS Collaboration, "ATLAS: Detector and physics performance technical design report. Volume 1",.

[64] ATLAS Collaboration, "ATLAS: Detector and physics performance technical design report. Volume 2",.

[65] J. Pequenao and P. Schaffner, "How ATLAS detects particles: diagram of particle paths in the detector", (2013).

[66] L. Gonella, "The ATLAS ITk detector system for the Phase-II LHC upgrade", *Nuclear Instruments and Methods in Physics Research Section A: Accelerators, Spectrometers, Detectors and Associated Equipment* **1045** (2023) 167597, doi:https://doi.org/10.1016/j.nima.2022.167597.

[67] S. Ryu and on behalf of the ATLAS TDAQ Collaboration, "FELIX: The new detector readout system for the ATLAS experiment", *Journal of Physics: Conference Series* **898** (oct, 2017) 032057.

[68] ATLAS Collaboration, "A High-Granularity Timing Detector (HGTD) in ATLAS : Performance at the HL-LHC", technical report, CERN, Geneva, 2018.

[69] ATLAS Collaboration, "The ATLAS Simulation Infrastructure", *Eur. Phys. J. C* **70** (2010) 823–874, doi:10.1140/epjc/s10052-010-1429-9,

arXiv:1005.4568.

[70] J. Allison et al., "Recent developments in Geant4", *Nuclear Instruments and Methods in Physics Research Section A: Accelerators, Spectrometers, Detectors and Associated Equipment* **835** (2016) 186–225.

[71] J. Allison et al., "Geant4 developments and applications", *IEEE Transactions on Nuclear Science* **53** (2006), no. 1, 270–278, doi:10.1109/TNS.2006.869826.

[72] S. Agostinelli et al., "Geant4—a simulation toolkit", *Nuclear Instruments and Methods in Physics Research Section A: Accelerators, Spectrometers, Detectors and Associated Equipment* **506** (2003), no. 3, 250–303.

[73] ATLAS Collaboration, "Electron and photon performance measurements with the ATLAS detector using the 2015–2017 LHC proton-proton collision data", *JINST* **14** (2019), no. 12, P12006, doi:10.1088/1748-0221/14/12/P12006, arXiv:1908.00005.

[74] ATLAS Collaboration, "Muon reconstruction and identification efficiency in ATLAS using the full Run 2 pp collision data set at $\sqrt{s} = 13$ TeV", *Eur. Phys. J. C* **81** (2021), no. 7, 578, doi:10.1140/epjc/s10052-021-09233-2, arXiv:2012.00578.

[75] ATLAS Collaboration, "Jet reconstruction and performance using particle flow with the ATLAS Detector", *Eur. Phys. J. C* **77** (2017), no. 7, 466, doi:10.1140/epjc/s10052-017-5031-2, arXiv:1703.10485.

[76] M. Cacciari, G. P. Salam, and G. Soyez, "The anti-k_t jet clustering algorithm", *JHEP* **04** (2008) 063, doi:10.1088/1126-6708/2008/04/063, arXiv:0802.1189.

[77] ATLAS Collaboration, "Jet energy scale and resolution measured in proton–proton collisions at $\sqrt{s} = 13$ TeV with the ATLAS detector", *Eur. Phys. J. C* **81** (2021), no. 8, 689, doi:10.1140/epjc/s10052-021-09402-3, arXiv:2007.02645.

[78] ATLAS Collaboration, "ATLAS flavour-tagging algorithms for the LHC Run 2 pp collision dataset", *Eur. Phys. J. C* **83** (2023), no. 7, 681, doi:10.1140/epjc/s10052-023-11699-1, arXiv:2211.16345.

[79] ATLAS Collaboration, "$E_{\mathrm{T}}^{\mathrm{miss}}$ performance in the ATLAS detector using 2015-2016 LHC pp collisions",.

[80] ATLAS Collaboration, "Performance of missing transverse momentum reconstruction with the ATLAS detector using proton-proton collisions at $\sqrt{s}$ = 13 TeV", *Eur. Phys. J. C* **78** (2018), no. 11, 903, doi:10.1140/epjc/s10052-018-6288-9, arXiv:1802.08168.

[81] ATLAS Collaboration, "Measurement of the polarisation of single top quarks and antiquarks produced in the t-channel at $\sqrt{s}$ = 13 TeV and bounds on the

tWb dipole operator from the ATLAS experiment", *JHEP* **11** (2022) 040, doi:10.1007/JHEP11(2022)040, arXiv:2202.11382.

[82] J. Erdmann et al., "A likelihood-based reconstruction algorithm for top-quark pairs and the KLFitter framework", *Nuclear Instruments and Methods in Physics Research Section A: Accelerators, Spectrometers, Detectors and Associated Equipment* **748** (Jun, 2014) 18â25, doi:10.1016/j.nima.2014.02.029.

[83] J. M. Campbell, R. Frederix, F. Maltoni, and F. Tramontano, "Next-to-Leading-Order Predictions for *t*-Channel Single-Top Production at Hadron Colliders", *Phys. Rev. Lett.* **102** (May, 2009) 182003, doi:10.1103/PhysRevLett.102.182003.

[84] M. Aliev et al., "HATHOR: HAdronic Top and Heavy quarks crOss section calculatoR", *Comput. Phys. Commun.* **182** (2011) 1034–1046, doi:10.1016/j.cpc.2010.12.040, arXiv:1007.1327.

[85] P. Kant et al., "HatHor for single top-quark production: Updated predictions and uncertainty estimates for single top-quark production in hadronic collisions", *Comput. Phys. Commun.* **191** (2015) 74–89, doi:10.1016/j.cpc.2015.02.001, arXiv:1406.4403.

[86] R. Frederix, E. Re, and P. Torrielli, "Single-top t-channel hadroproduction in the four-flavour scheme with POWHEG and aMC@NLO", *JHEP* **09** (2012) 130, doi:10.1007/JHEP09(2012)130, arXiv:1207.5391.

[87] S. Frixione, E. Laenen, P. Motylinski, and B. R. Webber, "Single-top production in MC@NLO", *JHEP* **03** (2006) 092, doi:10.1088/1126-6708/2006/03/092, arXiv:hep-ph/0512250.

[88] S. Frixione, E. Laenen, P. Motylinski, and B. R. Webber, "Angular correlations of lepton pairs from vector boson and top quark decays in Monte Carlo simulations", *JHEP* **04** (2007) 081, doi:10.1088/1126-6708/2007/04/081, arXiv:hep-ph/0702198.

[89] ATLAS Collaboration, "ATLAS event display of t-channel. Event number 279124678 in run 267073 recorded by ATLAS on 4 June 2015. ", (2015).

[90] M. Czakon et al., "Top-pair production at the LHC through NNLO QCD and NLO EW", *JHEP* **10** (2017) 186, doi:10.1007/JHEP10(2017)186, arXiv:1705.04105.

[91] S. Frixione et al., "Single-top hadroproduction in association with a W boson", *JHEP* **07** (2008) 029, doi:10.1088/1126-6708/2008/07/029, arXiv:0805.3067.

[92] ATLAS Collaboration, "Probing the quantum interference between singly and doubly resonant top-quark production in pp collisions at $\sqrt{s} = 13$ TeV with the ATLAS detector", *Phys. Rev. Lett.* **121** (2018), no. 15, 152002, doi:10.1103/PhysRevLett.121.152002, arXiv:1806.04667.

[93] S. Catani, F. Krauss, R. Kuhn, and B. R. Webber, "QCD matrix elements + parton showers", *JHEP* **11** (2001) 063, doi:10.1088/1126-6708/2001/11/063, arXiv:hep-ph/0109231.

[94] S. Hoeche, F. Krauss, S. Schumann, and F. Siegert, "QCD matrix elements and truncated showers", *JHEP* **05** (2009) 053, doi:10.1088/1126-6708/2009/05/053, arXiv:0903.1219.

[95] ATLAS Collaboration, "Estimation of non-prompt and fake lepton backgrounds in final states with top quarks produced in proton-proton collisions at \sqrts=8˜TeV with the ATLAS detector",.

[96] ATLAS Collaboration, "Performance of electron and photon triggers in ATLAS during LHC Run 2", *Eur. Phys. J. C* **80** (2020), no. 1, 47, doi:10.1140/epjc/s10052-019-7500-2, arXiv:1909.00761.

[97] ATLAS Collaboration, "Performance of the ATLAS muon triggers in Run 2", *JINST* **15** (2020), no. 09, P09015, doi:10.1088/1748-0221/15/09/p09015, arXiv:2004.13447.

[98] B. Grzadkowski, M. Iskrzyński, M. Misiak, and J. Rosiek, "Dimension-six terms in the Standard Model Lagrangian", *JHEP* **10** (2010) 085, doi:10.1007/JHEP10(2010)085, arXiv:1008.4884.

[99] ATLAS Collaboration, "Measurement of t-channel production of single top quarks and antiquarks in pp collisions at 13 TeV using the full ATLAS Run 2 data sample", arXiv:2403.02126.

[100] ATLAS Collaboration, "Luminosity determination in pp collisions at $\sqrt{s} = 13$ TeV using the ATLAS detector at the LHC", arXiv:2212.09379.

[101] W. Buttinger, "Using Event Weights to account for differences in Instantaneous Luminosity and Trigger Prescale in Monte Carlo and Data", technical report, CERN, Geneva, 2015.

[102] J. Butterworth et al., "PDF4LHC recommendations for LHC Run II", *J. Phys. G* **43** (2016) 023001, doi:10.1088/0954-3899/43/2/023001, arXiv:1510.03865.

[103] ATLAS Collaboration, "Studies on the improvement of the matching uncertainty definition in top-quark processes simulated with Powheg+Pythia 8", technical report, CERN, Geneva, 2023. All figures including auxiliary figures are available at https://atlas.web.cern.ch/Atlas/GROUPS/PHYSICS/PUBNOTES/ATL-PHYS-PUB-2023-029.

[104] A. Buckley and D. Bakshi Gupta, "Powheg-Pythia matching scheme effects in NLO simulation of dijet events", arXiv:1608.03577.

[105] R. J. Barlow and C. Beeston, "Fitting using finite Monte Carlo samples", *Comput. Phys. Commun.* **77** (1993) 219–228,

doi:10.1016/0010-4655(93)90005-W.

[106] ATLAS Collaboration, "Combined effective field theory interpretation of Higgs boson and weak boson production and decay with ATLAS data and electroweak precision observables",.

[107] CMS Collaboration, "Search for physics beyond the standard model in top quark production with additional leptons in the context of effective field theory", arXiv:2307.15761.

[108] SMEFiT Collaboration, "Combined SMEFT interpretation of Higgs, diboson, and top quark data from the LHC", *JHEP* **11** (2021) 089, doi:10.1007/JHEP11(2021)089, arXiv:2105.00006.

[109] Z. Kassabov et al., "The top quark legacy of the LHC Run II for PDF and SMEFT analyses", *JHEP* **05** (2023) 205, doi:10.1007/JHEP05(2023)205, arXiv:2303.06159.

[110] H. Brooks, C. T. Preuss, and P. Skands, "Sector Showers for Hadron Collisions", *JHEP* **07** (2020) 032, doi:10.1007/JHEP07(2020)032, arXiv:2003.00702.

[111] H. Brooks and P. Skands, "Coherent showers in decays of colored resonances", *Phys. Rev. D* **100** (2019), no. 7, 076006, doi:10.1103/PhysRevD.100.076006, arXiv:1907.08980.

[112] H. Brooks and C. T. Preuss, "Efficient multi-jet merging with the Vincia sector shower", *Comput. Phys. Commun.* **264** (2021) 107985, doi:10.1016/j.cpc.2021.107985, arXiv:2008.09468.

[113] S. Höche et al., "A Study of QCD Radiation in VBF Higgs Production with Vincia and Pythia", *SciPost Phys.* **12** (2022), no. 1, 010, doi:10.21468/SciPostPhys.12.1.010, arXiv:2106.10987.

[114] S. Höche and S. Prestel, "The midpoint between dipole and parton showers", *Eur. Phys. J. C* **75** (2015), no. 9, 461, doi:10.1140/epjc/s10052-015-3684-2, arXiv:1506.05057.

[115] J. Campbell, T. Neumann, and Z. Sullivan, "Single-top-quark production in the *t*-channel at NNLO", *JHEP* **02** (2021) 040, doi:10.1007/JHEP02(2021)040, arXiv:2012.01574.

[116] J. A. Aguilar-Saavedra, J. Boudreau, C. Escobar, and J. Mueller, "The fully differential top decay distribution", *Eur. Phys. J. C* **77** (2017), no. 3, 200, doi:10.1140/epjc/s10052-017-4761-5, arXiv:1702.03297.

[117] M. Jacob and G. C. Wick, "On the General Theory of Collisions for Particles with Spin", *Annals Phys.* **7** (1959) 404–428, doi:10.1006/aphy.2000.6022.

[118] ATLAS Collaboration, "Performance of the muon spectrometer alignment in 2017 and 2018 data", technical report, CERN, Geneva, 2021. All figures

including auxiliary figures are available at https://atlas.web.cern.ch/Atlas/GROUPS/PHYSICS/PUBNOTES/ATL-MUON-PUB-2021-002.

[119] ATLAS Collaboration, "ATLAS muon spectrometer: Technical Design Report". Technical design report. ATLAS. CERN, Geneva, 1997.

[120] M. Beker et al., "The Rasnik 3-point optical alignment system", *Journal of Instrumentation* **14** (2019), no. 8, doi:10.1088/1748-0221/14/08/P08010.

[121] H. van der Graaf et al., "The ultimate performance of the Rasnik 3-point alignment system", *Nuclear Instruments and Methods in Physics Research Section A: Accelerators, Spectrometers, Detectors and Associated Equipment* **1050** (2023) 168160, doi:https://doi.org/10.1016/j.nima.2023.168160.

[122] ATLAS Muon Collaboration, "ARAMyS: Alignment reconstruction software for the ATLAS muon spectrometer", *Nucl. Phys. B Proc. Suppl.* **172** (2007) 132–134, doi:10.1016/j.nuclphysbps.2007.07.012.

Chapter A

Alignment test of the ATLAS Muon Spectrometer.

Key to the precise measurement of the muons is the understanding of the positions and deformations of the several thousand chambers in the Muon Spectrometer (MS). Due to temperature variations and changes of the magnetic field the chambers and the support structures deform constantly. An optical alignment system is therefore installed in the MS to monitor the real time deformation of each individual chamber and monitor the relative position among the different chambers. The alignment during the Run 2 data-taking period is accurate to around 50 μm precision in a large part of the detector, with some regions having a precision close to 100 μm[118]. This means that the position of the chambers is known with the precision smaller than the diameter of a human hair over distances of several meters. A complete description of the alignment system of the ATLAS MS can be found in [119].

The alignment system works via projecting an encoded chessboard pattern via a lens on a sensor. Via monitoring the movement of the image the deformation or movement of chambers can be infered. This is done with the RASNIK system [120, 121]. By analysing the projected image one can measure deformations in the two orthogonal directions to the optical axis. It is also able to measure rotations of the image. Lastly via the changing size of the image one can deduce information in the direction along the optical axis.

Monitoring the chambers of the MS can firstly be done within one chamber to monitor the deformations of an individual chamber. The alignment system of Monitored Drift Tube (MDT) chambers is shown in fig. A.1. The setup has two RASNIK systems along the edge of the chamber and two cross RASNIK systems going diagonally across the chamber. This allows for measuring sags along the tubes and a twist of the chamber. Additionally, changes in the sideways direction can be measured. In small sectors a simpler system is adopted consisting of only 1 light ray.

The second way of using alignment systems is monitoring the movement of different chambers relative from each other. For that purpose, dedicated RASNIK systems monitor the position of chambers of the same type with respect to each other. Therefore, projective alignment systems are deployed, with the image mounted on the innermost chamber, the lens mounted on the middle chamber and the sensor mounted on the outermost chamber. These projective alignments units are illustrated in fig. A.2.

A misalignment of the chambers would result in a wrong measurement of the sagitta and thus a wrong momentum measurement. If the middle chamber is misaligned with respect to the inner and outer chamber a ”false” sagitta is measured. This ”false” sagitta is defined as:

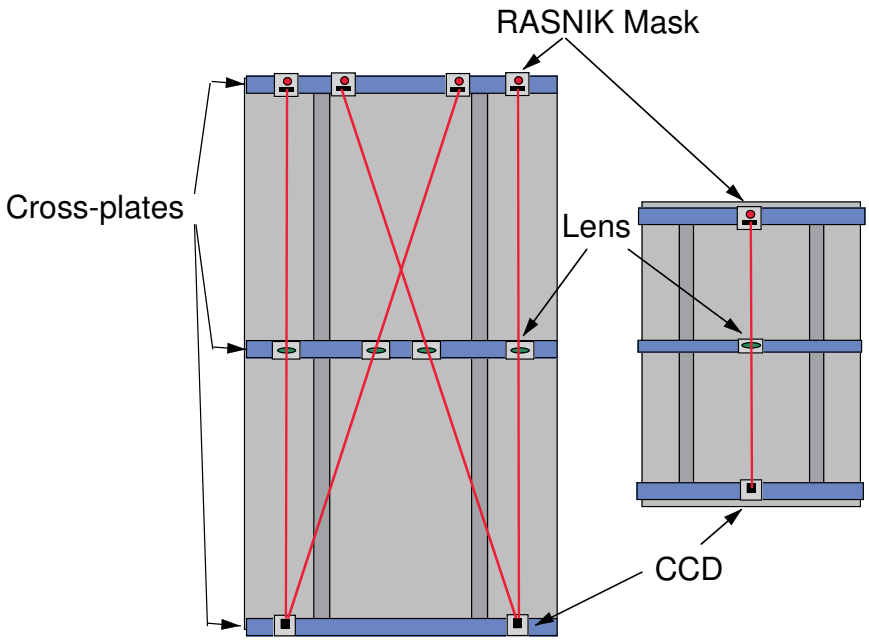

Figure A.1: Sketch of the in-plane alignment of the large MDT chamber(left) and a small chamber(right) in the ATLAS MS. Taken from [119].

$$s = \mathbf{IM} \cdot \frac{\mathbf{w} \times \mathbf{IO}}{\mid \mathbf{w} \times \mathbf{IO} \mid}, \tag{A.1}$$

where **IM**, is the vector between the inner chamber and the middle chamber, **IO** is the vector connecting the inner and outer chamber and **w** is the wire direction.

A.1 Initial alignment of the Muon Spectrometer endcap system in Run 3

To verify the optical alignment of the muon endcap system, data from muon tracks is used. This data is taken during special runs with the toroid field turned off to ensure that the trajectories of the muons are straight lines. The analysis of the 'toroid-off' runs taken in 2022 and 2023 and the calculation of these false sagittas in the endcap region of the MS is presented in the following.

To measure the sagitta, muon tracks are selected that have a hit in all three stations of the MS within the same sector in the ϕ direction. From the hits of these muons in a certain chamber in the MS a track is constructed. The muon track has to require some additional quality requirements. The track in the MS needs to be associated to a track in the inner detector. This allows for measuring the momentum of the

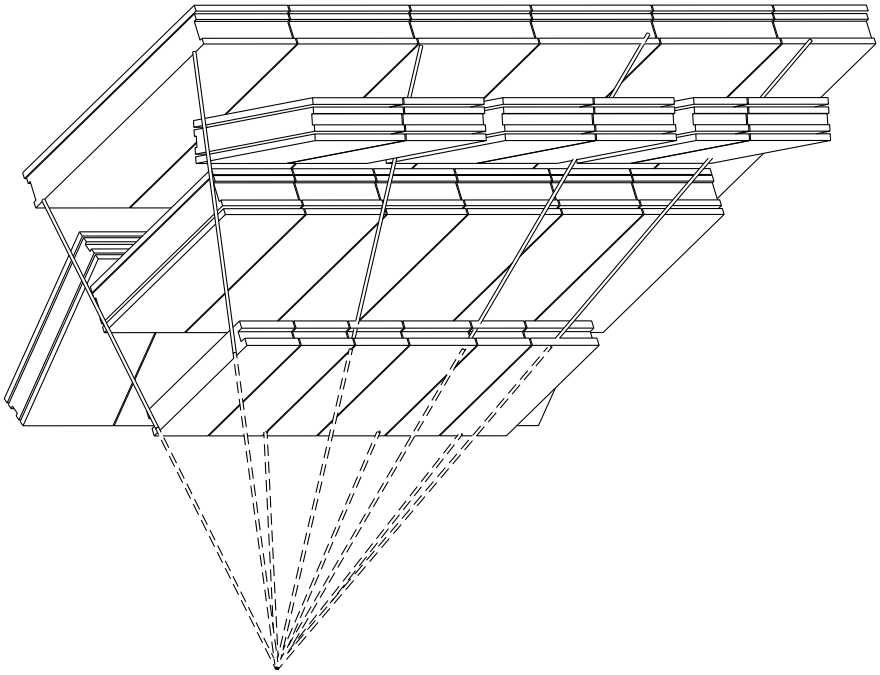

Figure A.2: Sketch of the chamber to chamber alignment of the ATLAS MS. Taken from [119].

muon from the curvature of the track in the magnetic field of the inner detector. The muon additionally has to leave at least 5 hits in the precision chamber of the middle wheel and 5 hits in the outer wheel. In fig. A.3 a two-dimensional histogram of the number of muon tracks in the New Small Wheel (NSW) is shown that pass the selection requirements for side A on the left and side C on the right. A good occupancy for all sectors can be observed. The positions of the tracks within the individual chambers (Inner, Middle or Outer chamber) of one sector are used to calculate the sagitta according to eq. (A.1). These positions have been corrected using the optical alignment system. A zero value of the sagitta would indicate that the alignment is working correctly.

The effect of multiple scattering complicates these alignment studies. If a muon traverses matter, it is deflected by interactions with the nuclei of the material. This is a stochastic process, however the average deflection of many muon tracks is zero. Therefore the sagitta is calculated over many muon tracks within a sector. A Cauchy distribution is fitted to the sagitta distribution within one sector. The center value of the fitted Cauchy function is taken as the false sagitta. For high momentum muons, the effect of multiple scattering is reduced as can be seen in fig. A.4. In this plot the

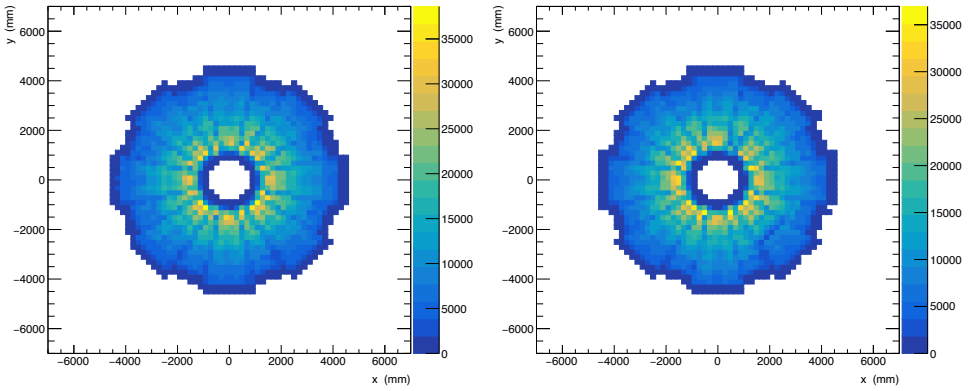

Figure A.3: A plot of the two-dimensional histogram of the number of muon tracks in the NSW that pass the selection requirements for side A on the left and side C on the right. The x-axis shows the x position of the track and the y-axis the y position of the track in mm, the colour encodes the number of tracks in each bin.

normalised sagitta distribution is shown for sector 1 on the A side for muons with momentum greater than 10 GeV in black, greater than 20 GeV in red and 30 GeV in green. This plot shows that the width of the distribution decreases for muons with larger momentum. To precisely estimate the mean of the sagitta distribution, a large amount of high momentum muons are needed to verify the alignment of the MS. In this analysis a momentum cut on the muon is put to 30 GeV. This momentum cut is chosen as it is a nice optimum between a reduced effect of multiple scattering while keeping sufficient number of muon tracks in each sector.

In fig. A.5 the distribution of the sagittas with the fitted Cauchy function is shown for sector 1 on side A in the left plot and for sector 2 on side A in the right plot. As can be seen the maximum of the peak is close to zero for both sectors, meaning that the alignment is working for these two sectors as expected.

A summary of the sagitta for all sectors is shown in fig. A.6. Sectors on side A are plotted in blue, while sectors on side C are shown in blue. The uncertainty on the points is from the uncertainty on the position of the maximum of the Cauchy distribution. The yellow band shows the accuracy of the muon alignment during Run 2 which was within $\pm 100\,\mu$m. The desired accuracy of the Muon Spectrometer is $\pm 40\,\mu$m, which is required for a momentum resolution of 10 % of muons with a momentum of 1 TeV. The precision of the alignment is within $200\,\mu$m for all sectors on both sides. Most regions have a precision well within $100\,\mu$m. The sagittas are on most chambers slightly positive. Wheter this is a systematic trend is difficult to say. The shift possibly originates from an overal shift in the z-coordinate of one of the chambers or a rotation of one of the wheels.

Further studies have to be performed to understand the deviations observed in the alignment. These include studies of the individual chambers of the NSW, where

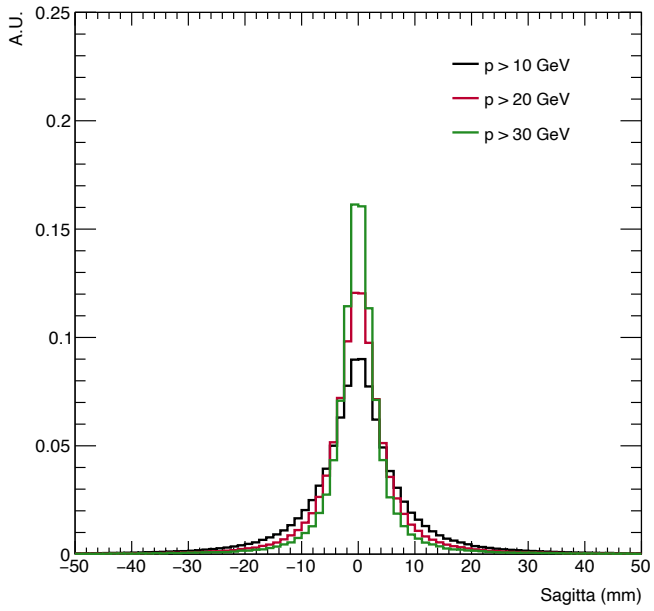

Figure A.4: Normalised sagitta distribution of sector one of side A for data collected during the toroid-off run in 2023. The plot shows the sagitta distribution for muons with momentum greater than 10 GeV in black, greater than 20 GeV in red and 30 GeV in green.

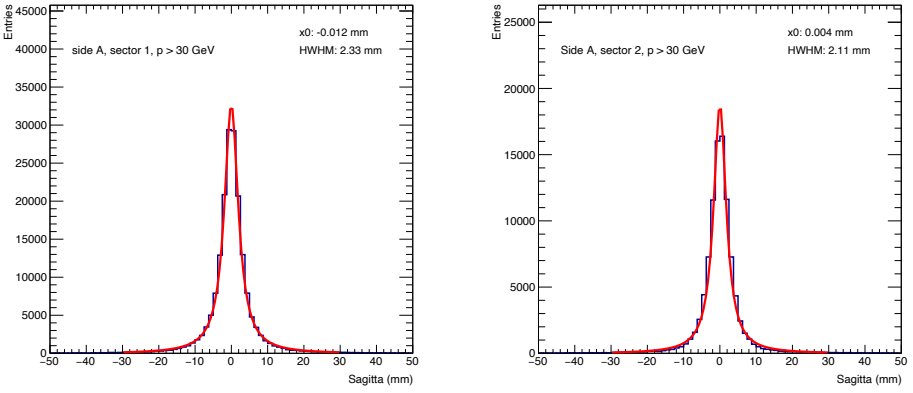

Figure A.5: Sagitta distribution of sector one (left) and two (right) of side A for data collected during the toroid-off run in 2023. The red line is the fitted Cauchy distribution, the values for the location of the maximum and the half width at half maximum are shown in the top right of the plot.

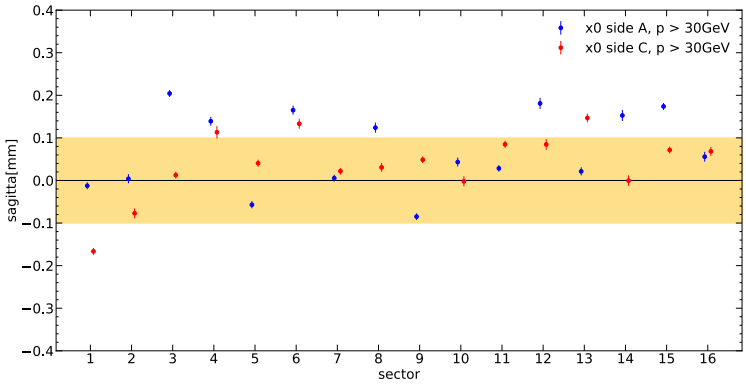

Figure A.6: Distribution of the sagittas measured for each sector for side A in blue and side C in red. The yellow band indicates values of $\pm$ 100 μm.

the alignment of each MM or sTGC chamber can be studied individually. This can provide understanding of the structure of the NSW and eventual misalignment of the individual chambers. Additionally one can measure the false sagitta as a function of either η of the muon or depending on the position along the wire. This could give important insights on the rotation of the chamber. This initial study however proves that no large biases are introduced due to the alignment of the chambers. Once all the details of the toroid-off run are understood corrections to the alignment can be determined, resulting in a better understanding of the positioning of the chambers during run conditions and a better momentum estimation of muons.

A.2 Verification of the alignment system in the sBIS chambers

After the Run 3 running period, which is expected to end in 2025, the LHC will be upgraded to run with even higher collision rates for the HL-LHC period starting in 2029. The ATLAS detector will be upgraded in this time. The small inner chambers of the MS in the barrel region for η regions 1 to 6, BIS 1 to 6, will be replaced. The new chambers will have six layers of small Monitored Drift Tube chambers (sMDT) with a diameter of 15 mm[1]. This gives place to install an additional RPC chamber in the innermost layer of the MS to improve the trigger by adding a hit in the innermost layer. To accommodate this space the in-plane alignment system has to be more compact. At Nikhef a prototype alignment frame was constructed and tests are performed on how this prototype is able to reconstruct deformations. This chapter will describe these tests. First an introduction on how the chamber is parameterised is given. After that, different tests for deforming the alignment chamber are discussed and the results are presented.

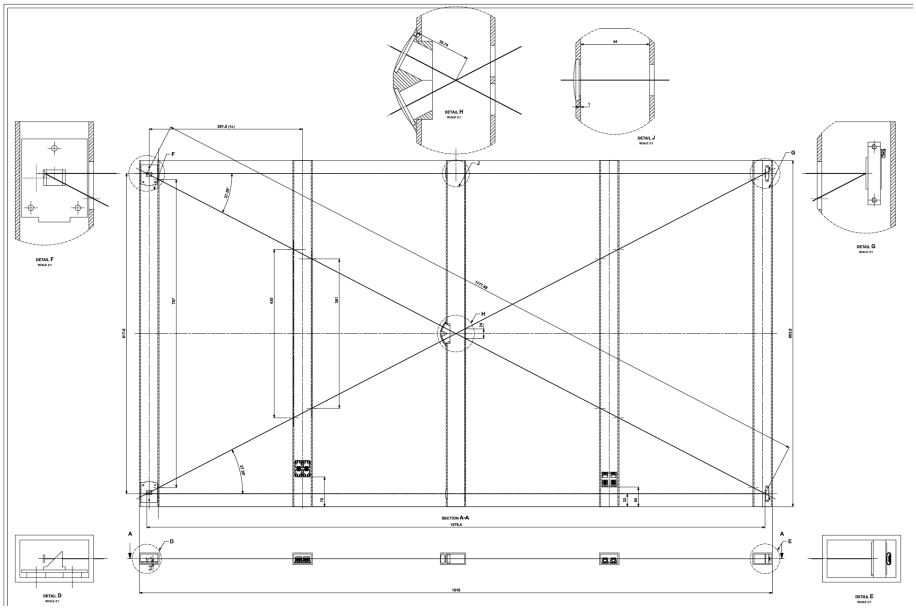

Figure A.7: A sketch of the allignment system used for the sBIS chambers. on the left are the two RASNIK sensors, in the middle the four lenses and on the right the two masks

A sketch of the alignment system of the sBIS chambers is shown in fig. A.7. On this frames the sMDT tubes will be mounted. In total the frame exists of 2 RASNIK masks which are projected via 4 lenses on two sensors. This creates in total 4 light-paths,

[1] compared to the 30 mm tubes of the MDT chambers

two along the edges of the chamber and two going from one side of the chamber to the other side. The coordinate system used to define the frame is the following:

- The x axis is along the tubes. Hence, both masks have the same x coordinate. The zero-point is in the middle of the chamber. The direction is from the masks towards the sensors. The coordinate is denoted as x_c, to avoid confusion with the RASNIK coordinates.
- the y axis, with coordinate y_c, points out of the structure. All RASNIK elements have without deformation a value of zero for this coordinate.
- the z axis, z_c is perpendicular to the axis x_c and y_c in such a way that it creates a right-handed coordinate system. The mask, lens and sensor for one edge system thus have the same z coordinate.

A very noteworthy feature is that the sensor is now laying in vertical position but is rotated to reduce the space taken by the sensor. A prism reflects the light onto the rotated sensor. Due to the prism the sensor is in the x_c, z_c plane. It is also turned with 90 degrees. This all has as result that a change in y_c of the mask position results in a change of X_R of the RASNIK output. A change of z_c of the mask position results in a change of X_R of the RASNIK output. If the masks moves in x_c direction the scale output of the RASNIK system will change. A movement in $+x_c$ of the mask will increase the scale of the picture. The naming of the RASNIK components is the following:

- the components where z_c is close to 0 are labeled with a 1.
- the compenents where z_c is close to its maximum value are labeled 2.
- The RASNIK system is label as MSKX_SENX. where X is the corresponding mask or sensor.

The first test performed is to create a deformation of the mask position in z_c. For this study the frame at $x_c = 0$ is moved. Since the effect is the same for all four systems the difference of the RASNIK y-values should all change simultaneous and with the same value. Due to different orientations a minus sign is expected between the systems. During this test the frame is deformed two times by slightly pushing the edge. This is monitored by the RASNIK sensors and shown in fig. A.8. The result is as expected, all four systems change with the same value in Y_R. The output of X_R for all four systems is not changed significantly as it is expected.

Deformations in y_c are tested by moving the mask positions vertically. During this test the other components are all kept in place. This is achieved by putting heavy weights on the frame at the lens and the sensor positions for both edge systems. The movement in z_c are kept as small as possible for all the components. For the lenses and the sensors this is achieved relatively easily due to the heavy weights. However when moving the mask in y_c it is difficult to not unintentionally move the frame in z_c. Therefore a special setup was produced which is displayed in fig. A.9. A displacer which enables to move the frame in y_c is used. This is monitored by a dial gauge, which measures the y_c deviation at the position of the mask. By comparing the deviations measured by the in-plane alignment system and the dial gauge the

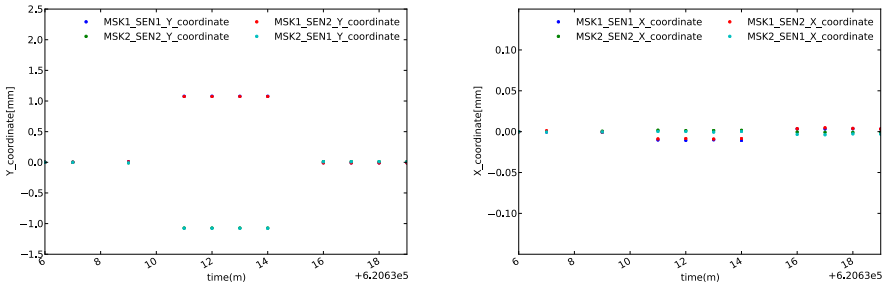

Figure A.8: Output of the RASNIK system after deforming the frame in the z_c position. On the top for the Y_R coordinate of RASNIK and on the bottom for the X_R coordinate of RASNIK.

performance of the in-plane alignment system can be tested. Such a system, with dial gauge and displacer, is placed at both masks. The dial gauges have a precision of 10 μ m.

A movement of the mask by y_c corresponds directly to a movement in RASNIK coordinates X_R. For the test, the mask on both sides are moved with 0,100,200 and 300 µm. This results in 12 measurements with different combinations of the deviations. For each RASNIK system the deviation as a function of the corresponding dial gauge displacement is plotted in fig. A.10. The different sign of the slopes is due to the rotation of the mask. The results from the RASNIK in-plane alignment system correspond within 10 µm precision of the dial gauges. This is within the required precision of 15 µm, needed for the reconstruction of the muons.

ARAMyS

The previous measurements already demonstrates that the in-plane alignment reconstruction work. In ATLAS the muon alignment reconstruction is done with the ARAMyS package [122]. As proof of concept the deformations in y_c are reconstructed with the ARAMyS package in this section. The data shown in the previously studies is used as input for the ARAMyS fit.

In ARAMyS vertical deformations of the frame are described using the following three parameters:

- A sag along edge 1.
- A sag along edge 2.
- A torsion.

In ARAMyS these parameters are simultaneously fitted to obtain the best agreement with the measured deformations from the four RASNIK in-plane systems.

A sag is the downward curve of the frame at its center position. It is parameterised

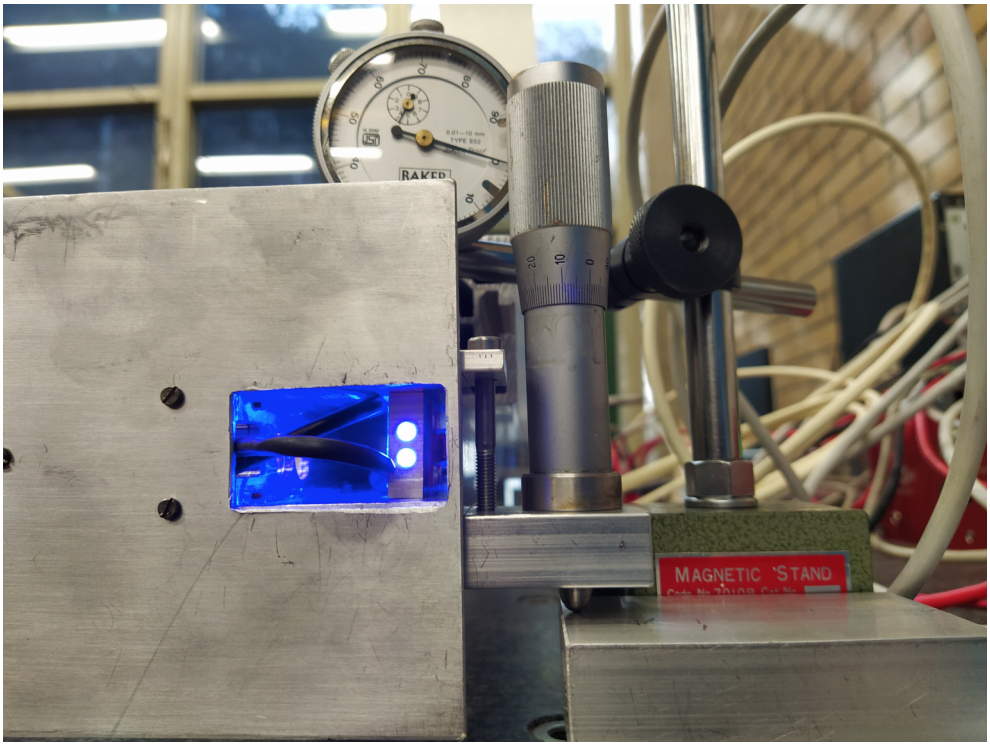

Figure A.9: The setup for deviating the frame in y_c. On the left is the spacer with one of the enlightened masks. In the center is the device which creates the deviation. Behind is the dial gauge for monitoring the deviation. At the other mask side the same setup is placed.

as a quadratic function with its extremum at $x_c = 0$. A sag along the edge systems has the following function:

$$x_c(z_c) = a \cdot ((\frac{x_c}{0.5 \cdot x_{total}})^2 - 1), \tag{A.2}$$

where x_{total} is the length of the spacer frame. The frame has a length of $x_{total} = 1616\,\text{mm}$.

fig. A.11 shows the reconstructed sags as a function of the displacement of the corresponding mask measured by the dial gauge. They agree very well with the expected results from the dial gauges. Since the mask moves upward, which is qualitatively the same as the lens and the sensor moving downwards, the sag equals half the displacement of the mask.

The torsion of the frame is defined as the x-rotational position between the mask side and the sensor side. Due to only small torsion, it is parameterised as follows:

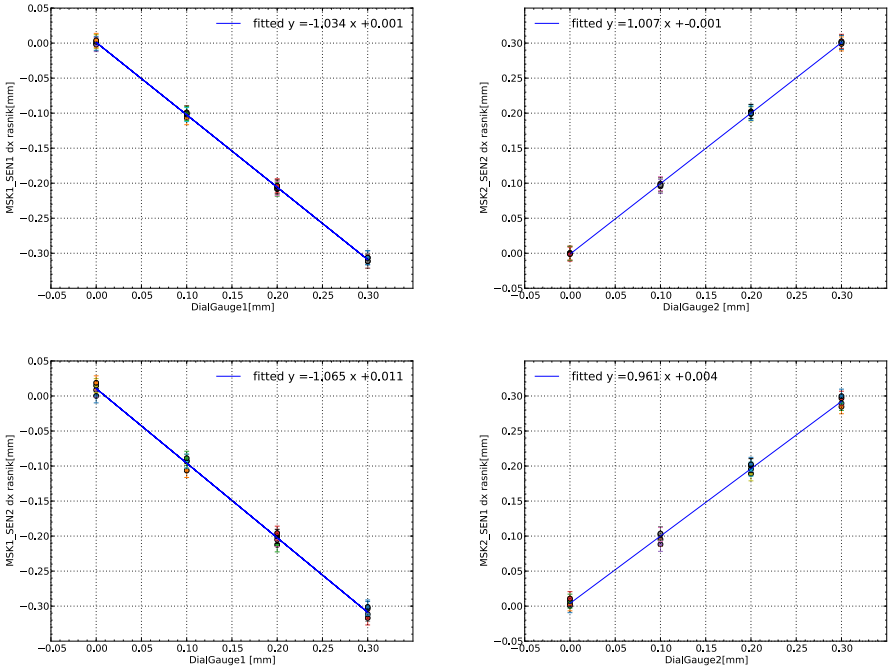

Figure A.10: The measured deviations from each RASNIK system as function of the corresponding dial gauge. On the top left are the deviations plotted for edge system 1, located at $z_c = 0$, and on the top right for the other edge system. The bottom left is the RASNIK cross system which shares the mask with edge system 1. On the bottom right is the remaining cross system, which shares its mask with edge system 2.

$$\phi = \frac{\Delta y_c^{mask-side} - \Delta y_c^{sensor-side}}{d} \tag{A.3}$$

where d=817 mm corresponding to the distance between the two masks and Δy_c is the vertical tilt of the chamber at either the mask side or sensor side between the two outer edges. The torsion can be measured by taking the difference of the two RASNIK cross systems.

The measured torsion agrees very well with the expected slope of $\frac{1}{d} = 1.222$ as can be seen from fig. A.12. This concludes that the in-plane alignment system is able to monitor deformations of the chamber.

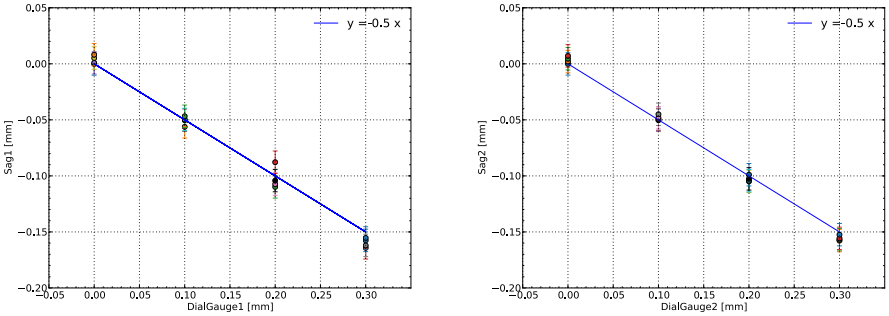

Figure A.11: This figure shows the reconstructed sagitta by ARAMyS as a function of the measured dial gauge displacement for edge 1 on the left and edge 2 on the right.

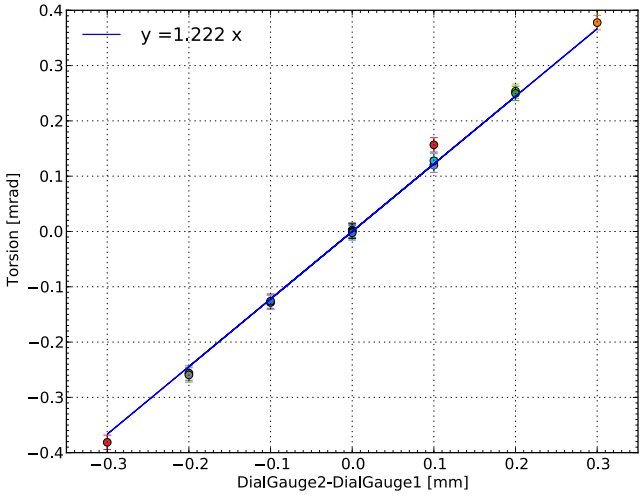

Figure A.12: This figure shows the torsion reconstructed by ARAMyS as a function of the difference between the displacement of the dial gauges.

Chapter B

Transferfunctions.

This appendix summarises the transferfuctions used in this analysis for each object.

B.1 b-jets

The parameterisation of the transferfunction parameters for b-jets are:

$$\mu_1 = a_1 + \frac{b_1}{E_{\text{Truth}}}, \tag{B.1}$$

$$\sigma_1 = a_2 + \frac{b_2}{\sqrt{E_{\text{Truth}}}}, \tag{B.2}$$

$$p_3 = a_3 + \frac{b_3}{E_{\text{Truth}}}, \tag{B.3}$$

$$\mu_2 = a_4 + \frac{b_4}{\sqrt{E_{\text{Truth}}}}, \tag{B.4}$$

$$\sigma_2 = a_5 + b_5 E_{\text{Truth}}. \tag{B.5}$$

The values of the parameters are summarised in table B.1.

Table B.1.: Parameters of the transferfunctions for b-jets in different regions of η.

	$\lvert\eta\rvert < 0.8$	$< \lvert\eta\rvert < 1.37$	$< \lvert\eta\rvert < 1.52$	$< \lvert\eta\rvert < 2.5$
a_1	-0.012	0.00	0.03	0.00
b_1	2.31	2.63	-0.29	2.43
a_2	0.054	0.08	0.08	0.06
b_2	0.52	0.49	0.68	0.73
a_3	0.00	0.00	0.00	0.00
b_3	37.96	59.77	76.41	132.99
a_4	0.56	0.58	0.65	0.50
b_4	-3.92	-5.00	-6.68	-5.90
a_5	0.22	0.23	0.23	0.22
b_5	0.00	0.00	0.00	0.00

B.2 Light-jets

Light-jets follow the same parameterisation as b-jets. The values for light-jets are summarised in table B.2

Table B.2.: Parameters of the transferfunctions for light-jets in different regions of η.

	$\lvert\eta\rvert < 0.8$	$< \lvert\eta\rvert < 1.37$	$< \lvert\eta\rvert < 1.52$	$< \lvert\eta\rvert < 2.5$	$< \lvert\eta\rvert < 4.5$
a_1	0.03	0.04	0.06	0.03	0.00
b_1	-3.63	-7.98	-13.94	-14.53	-29.66
a_2	0.037	0.05	0.052	0.05	0.10
b_2	0.86	0.99	1.34	1.40	1.08
a_3	0.00	0.00	0.00	0.00	0.05
b_3	3.80	7.01	4.55	14.58	34.33
a_4	0.18	0.24	-0.42	0.18	0.09
b_4	-3.54	-5.08	-0.81	-6.57	-10.34
a_5	0.33	0.35	0.41	0.34	0.33
b_5	0.00	0.00	0.00	0.00	0.00

B.3 Electrons

The parameterisation of the transferfunction parameters for electrons are:

$$\mu_1 = a_1 + b_1 E_{\text{Truth}}, \tag{B.6}$$

$$\sigma_1 = a_2 + \frac{b_2}{\sqrt{E_{\text{Truth}}}}, \tag{B.7}$$

$$p_3 = a_3 + b_3 E_{\text{Truth}}, \tag{B.8}$$

$$\mu_2 = a_4 + \frac{b_4}{\sqrt{E_{\text{Truth}}}}, \tag{B.9}$$

$$\sigma_2 = a_5 + b_5 E_{\text{Truth}}. \tag{B.10}$$

Their values are summarised is table B.3.

Table B.3.: Parameters of the transferfunctions for electrons in different regions of η.

	$\lvert\eta\rvert < 0.8$	$< \lvert\eta\rvert < 1.37$	$< \lvert\eta\rvert < 2.5$
a_1	0.001	0.000	0.002
b_1	0.000	0.000	0.000
a_2	0.003	0.007	0.000
b_2	0.126	0.171	0.351
a_3	0.083	0.107	0.099
b_3	-0.001	0.000	0.000
a_4	0.038	0.081	0.041
b_4	-0.171	-0.510	-0.289
a_5	0.048	0.063	0.078
b_5	0.000	0.000	0.000

B.4 Muons

The parameterisation of the muon transferfuction do not depend on the truth energy of the muon but the transverse momentum of the muon. They are parameterised as:

$$\mu_1 = a_1 + b_1 p_{\mathrm{T,Truth}}, \tag{B.11}$$

$$\sigma_1 = a_2 + b_2 p_{\mathrm{T,Truth}}, \tag{B.12}$$

$$p_3 = a_3 + b_3 p_{\mathrm{T,Truth}}, \tag{B.13}$$

$$\mu_2 = a_4 + b_4 p_{\mathrm{T,Truth}}, \tag{B.14}$$

$$\sigma_2 = a_5 + b_5 p_{\mathrm{T,Truth}}. \tag{B.15}$$

Their values are summarised in table B.4.

Table B.4.: Parameters of the transferfunctions for muons in different regions of η.

	$\lvert\eta\rvert < 1.11$	$< \lvert\eta\rvert < 1.25$	$< \lvert\eta\rvert < 2.5$
a_1	0.001	0.002	-0.001
b_1	0.000	0.000	0.000
a_2	0.015	0.020	0.024
b_2	0.000	0.000	0.000
a_3	0.009	0.000	0.000
b_3	0.000	0.001	0.001
a_4	0.038	0.040	0.019
b_4	0.000	0.000	0.000
a_5	0.053	0.061	0.062
b_5	0.000	0.000	0.000

B.5 $E_{\mathrm{T}}^{\mathrm{miss}}$

The parameterisation of the transferfunction parameters for $E_{\mathrm{T}}^{\mathrm{miss}}$ is:

$$\mu_1 = a_1 + \frac{b_1}{E_{\mathrm{Truth}}}, \tag{B.16}$$

$$\sigma_1 = a_2 + \frac{b_2}{\sqrt{E_{\mathrm{Truth}}}}, \tag{B.17}$$

$$p_3 = a_3 + \frac{b_3}{E_{\mathrm{Truth}}}, \tag{B.18}$$

$$\mu_2 = a_4 + \frac{b_4}{\sqrt{E_{\mathrm{Truth}}}}, \tag{B.19}$$

$$\sigma_2 = a_5 + b_5 E_{\mathrm{Truth}}. \tag{B.20}$$

As $E_{\mathrm{T}}^{\mathrm{miss}}$ is per definition in the azimuthal direction no bin in η is considered. The values are summarised in table B.5.

Table B.5.: Parameters of the transferfunctions for $E_{\mathrm{T}}^{\mathrm{miss}}$.

	inclusive
a_1	-9.4
b_1	1600
a_2	24.2
b_2	-170
a_3	0.3
b_3	12.4
a_4	-44
b_4	570
a_5	11
b_5	0.04

Chapter C

Event distributions in the control regions.

This Appendix shows pre-fit event distributions of the final state particles in the $t\bar{t}$ and W+jets control regions.

C.1 Distributions in the $t\bar{t}$ region

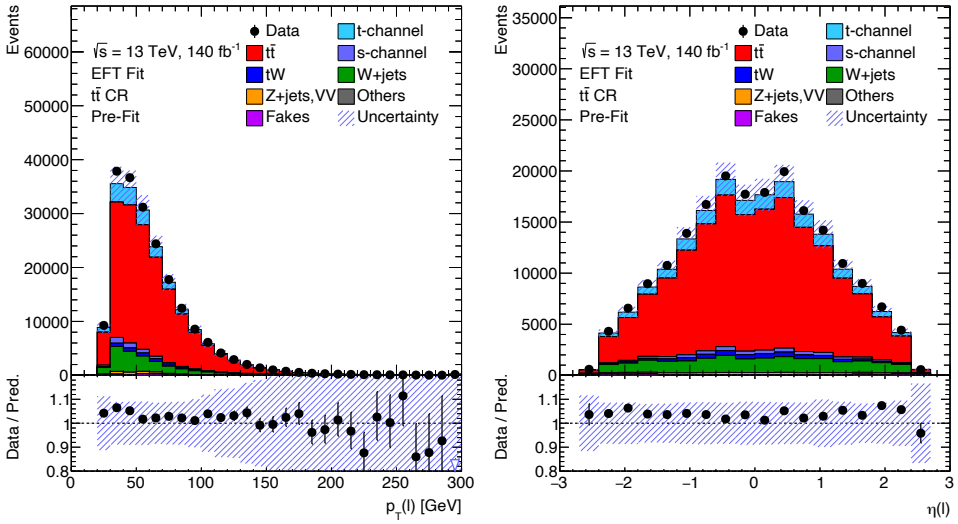

Figure C.1: Distribution of the lepton p_{T} (left) and pseudorapidity (right) for events in the $t\bar{t}$ control region. The contributions for the different processes are stacked upon each other. The black dots represent the data. The shaded band shows the uncertainties from systematic sources as well as limited size of the MC statistics.

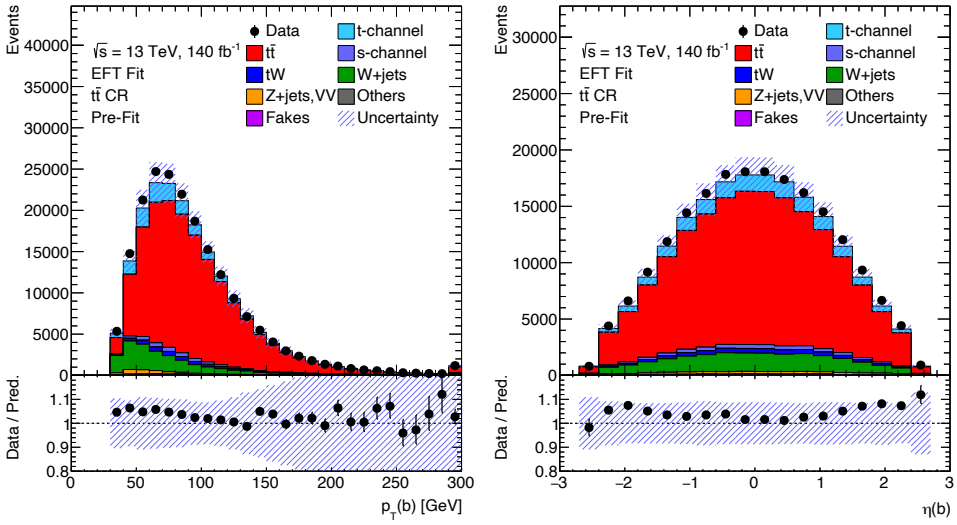

Figure C.2: Distribution of the b-jet p_{T} (left) and pseudorapidity (right) for events in the $t\bar{t}$ control region. The contributions for the different processes are stacked upon each other. The black dots represent the data. The shaded band shows the uncertainties from systematic sources as well as limited size of the MC statistics.

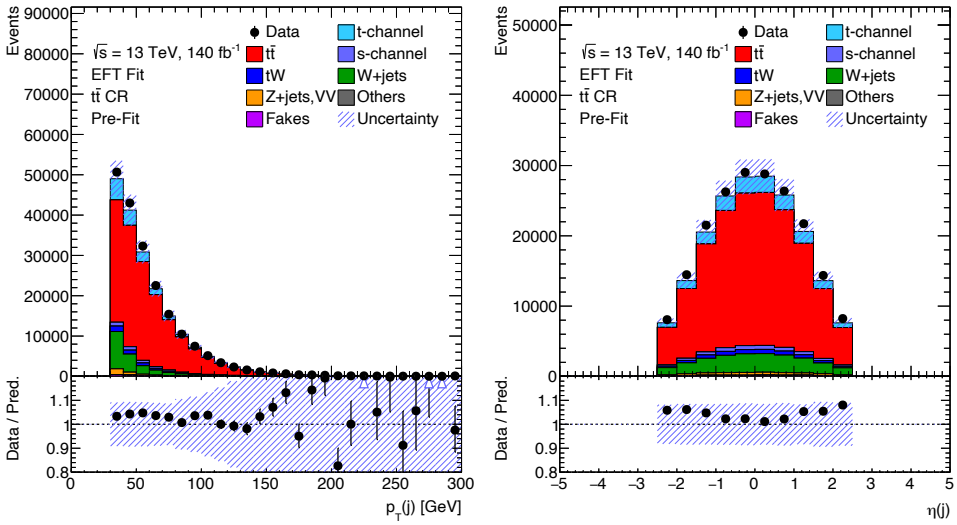

Figure C.3: Distribution of the light-jet p_{T} (left) and pseudorapidity (right) for events in the $t\bar{t}$ control region. The contributions for the different processes are stacked upon each other. The black dots represent the data. The shaded band shows the uncertainties from systematic sources as well as limited size of the MC statistics.

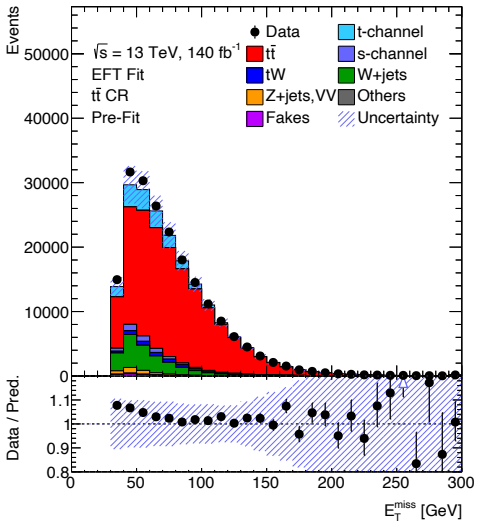

Figure C.4: Distribution of missing transverse energy for events in the $t\bar{t}$ control region. The contributions for the different processes are stacked upon each other. The black dots represent the data. The shaded band shows the uncertainties from systematic sources as well as limited size of the MC statistics.

C.2 Distributions in the W+jets region

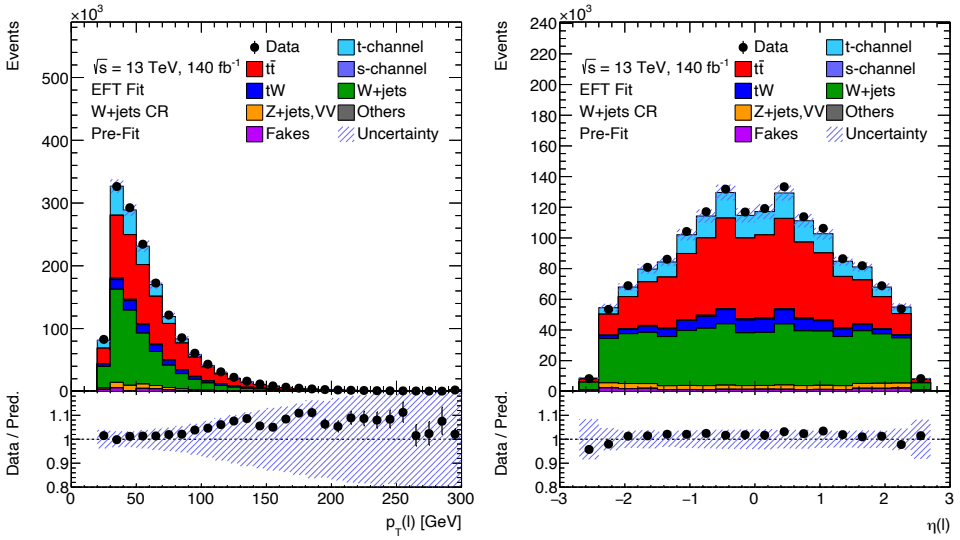

Figure C.5: Distribution of the lepton p_{T} (left) and pseudorapidity (right) for events in the W+jets control region. The contributions for the different processes are stacked upon each other. The black dots represent the data. The shaded band shows the uncertainties from systematic sources as well as limited size of the MC statistics.

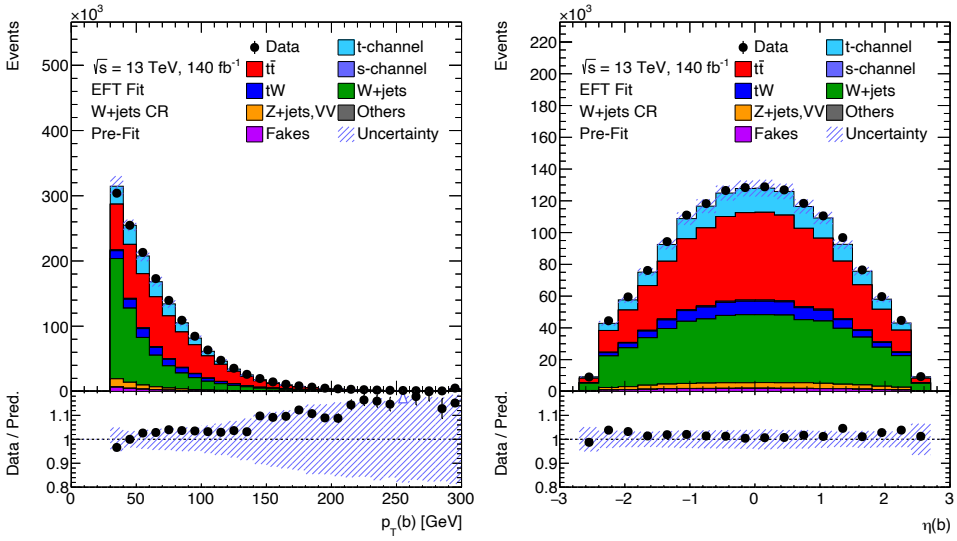

Figure C.6: Distribution of the b-jet p_{T} (left) and pseudorapidity (right) for events in the W+jets control region. The contributions for the different processes are stacked upon each other. The black dots represent the data. The shaded band shows the uncertainties from systematic sources as well as limited size of the MC statistics.

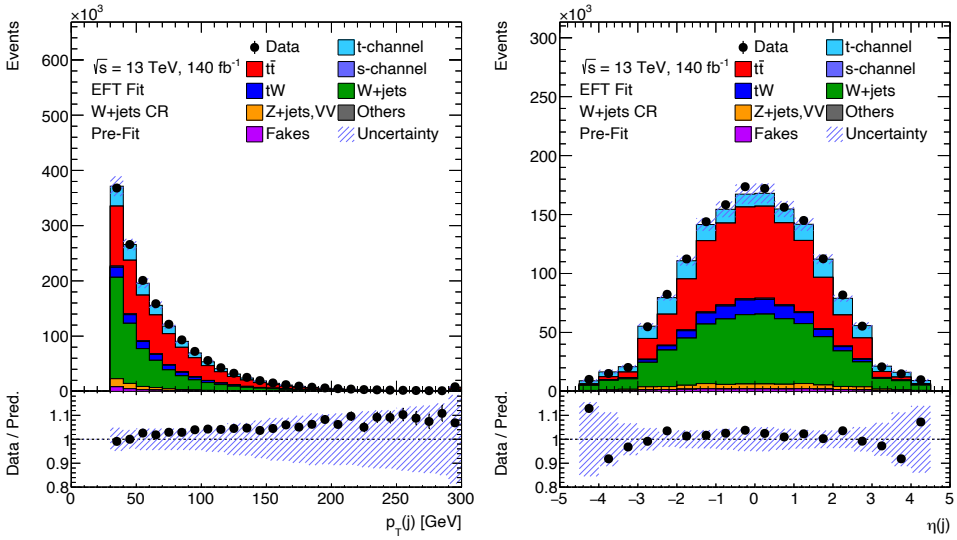

Figure C.7: Distribution of the light-jet p_{T} (left) and pseudorapidity (right) for events in the W+jets control region. The contributions for the different processes are stacked upon each other. The black dots represent the data. The shaded band shows the uncertainties from systematic sources as well as limited size of the MC statistics.

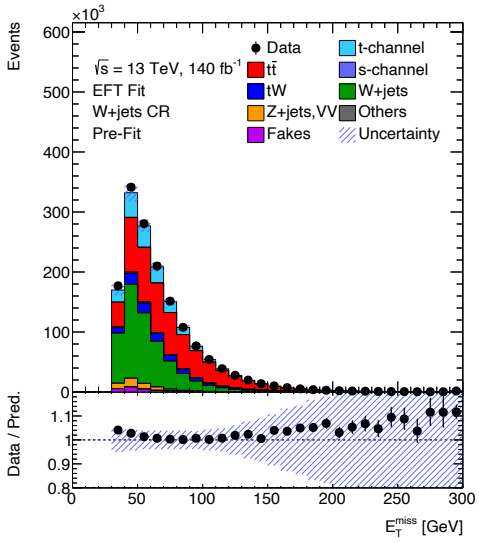

Figure C.8: Distribution of missing transverse energy for events in the W+jets control region. The contributions for the different processes are stacked upon each other. The black dots represent the data. The shaded band shows the uncertainties from systematic sources as well as limited size of the MC statistics.

Acknowledgements

I am deeply grateful that I was able to do my research at the University of Amsterdam and Nikhef in the field of particle physics. I truly enjoyed the years working on my PhD thesis. I cherish all the connections and friendships I made on the way and I sincerely thank everyone who has been part of this journey. In these last pages I want to thank everyone who has been part of it.

Ik wil Marcel Vreeswijk bedanken die me de kans bood om dit onderzoek te kunnen doen in de Nikhef ATLAS groep. Dankjewel voor al de tijd die je voor mij vrij hebt gemaakt. Ik kon altijd op je deur kloppen voor jou advies en ik ben dankbaar voor alle discussies die we hebben gehad. Ze hebben me gemaakt tot de natuurkundige die ik nu ben. Dankjewel voor het lezen en corrigeren van mijn thesis en de ontzettend snelle feedback die ik altijd van jouw kreeg. Marcel, ik kon me geen betere begeleider voorstellen. Ook wil ik Eric laenen bedanken als copromoter. Ik heb veel geleerd van jou theoretische kennis. Ik wil je ook bedanken voor al je feedback op, met name het theoretische deel, van mijn thesis.

Next I want to thank Clara Nellist, Pamela Ferrari, Joe Boudreau, Wouter Verkerke, Paul de Jong and Jordy de Vries for being part of my thesis committee and taking the time to thoroughly read my manuscript. Marcel Merk wil iech bedanken vuur het volge van mienge doctor als C3 lid. Danke vuur al dieng tsied!

Being part of the ATLAS collaboration enabled me to do my research in one of the most collaborative working environments I could imagine. All the people I worked with in these years I want to thank for all the amazing times and discussion we had from which I learned so much. I want to explicitly mention a few below.

Foremost I want to thank everyone in my analysis group from Pittsburgh and Valencia: Jim, Joe, Chi-Wing, Raees, Huacheng, Mariam, Carlos, Maria Jose, Galo. Not only did I learn a lot from all of you, I am also grateful to have been working in this collaborative environment. All the discussions we had about EFTs, top physics, systematics, event selection and all different kind of topics shaped my PhD. I will never forget the hackathon we had in Valencia and the amazing moments we shared during that time. I hope we will keep collaborating in the future. Ook wil ik Marc de Beurs bedanken, mijn voorganger op Nikhef waarvan ik veel geleerd heb in het begin van mijn PhD.

Next I want to thank everyone whom I worked with on the muon Alignment studies. Dankjewel Tristan voor mijn begeleiding in dit deel van mijn PhD, dankzij jou heb ik niet alleen het qualification project op Nikhef over de in-plane alignment kunnen doen, maar ook een eerste analyse van de run 3 alignment van de ATLAS Muon Spectrometer. Dankjewel aan Harry van der Graaf als technische begeleider voor het in-plane alignment project. Jouw passie voor RASNIK en je praktische manier van werken hebben mij veel geleerd. Also a special thanks to Robert and Karol for

the technical help involving the RASNIK setup. I also want to thank everyone I worked with on the run 3 alignment studies from CERN and Tufts University. A special word of thanks to Bailey with whom I did the hands on work of this very first analysis. I want to thank Hugo, Nicoletta, Patrick, Johannes and Chistoph for the supervision during this project. Without your expertise on the muon alignment system and the reconstruction of muons within ATLAS this project would not be possible.

Most of my time during my PhD was spend at Nikhef and I am very grateful for that. Even though my time at Nikhef was interupted by the pandemic and ongoing constructions, I always felt at home. I enjoyed all the discussions we had and the time we spend during coffee breaks, lunches, table tennis rounds, vrijmibos and all the dinners we had together. Thank you everyone who made Nikhef my home. A special thank you for the ATLAS group at Nikhef: Alex, Anamika, Andrea A., Andrea V., Ali, Alice, Alessio, Ann-Kathrin, Ash, Birgit, Broos, Brian, Bryan, Clara, Carlo G., Carlo P., Carsten, Dorian, Denys, Diana, Duncan, Dylan, Edwin, Emma, Eveline, Federica, Flavia, Florian, Frank, Geoffrey, Hannah, Hella, Ivo, Jasper, JJ., Jos, Jochem, Kees, Lisanne, Lydia, Liza, Luca, Mengqing, Marc, Marcel, Marion, Marko, Marten, Matous, Matteo, Michiel, Nicolo, Oliver, Osama, Pamela, Peter K., Peter M., Peter V., Pepijn, Petja, Pim, Polina, Pranati, Robin K., Robin H., Sacha, Saskia, Sil, Stephen, Stefano, Tal, Terry, Tommaso, Tim, Tristan, Uraz, Walter, Wouter M., Wouter V., Zef, and Zhuoran. I hope we can stay in touch, be it via an email (or a few thousand).

I'd like to thank Hannah, Brian, Carlo, Marcel, Joe and Maria-Jose for helping me in applying for my current job as a Postdoc at the University of Liverpool. I am very happy at this new place, continue doing what I love to do. I am very excited for my future in the di-Higgs analysis.

Een speciaal woord van dank aan Bryan Kortman waarmee ik ongeveer tegelijkertijd mijn PhD avontuur begon. Ik heb veel geleerd van al de discussies over EFTs, statistiek en particle physics. Dankjewel vooral ook voor al de track mania en spellenavonden tijdens de corona lockdown met jou en Edda. De vriendschap zal ik voor altijd koesteren. Thank you Florian, for the amazing times we shared both in Amsterdam and in Geneva. I truly enjoyed all the time we went swimming in the lake of Geneva, having dinner together and the two times we sat on a boat all day descending the Rhone river. I am happy I could teach you a bit of tennis and I appreciate your effort into trying to teach me how to ski, it was terrifying but great fun.

Thank you Andrea, Antonio and Chiara with whom I shared a home during my stay at CERN. I enjoyed the time we spend together, our family trips to the market in Ferney-Voltaire and the occasional kitchen talks. Andrea, thank you for sharing your delicious pasta carbonara and I hope I have enriched your world with my version of one of my favourite dishes, butter chicken. Brenda, you will always be my queen.

Zhuoran, I can't express how grateful I am having you in my life. Thank you for always supporting me on all the stressful days and sometimes nights. I thank you

for all the time we spend together, I could not have done this PhD without you.

Dan wil ik ook mijn vrienden in Limburg bedanken. We zien elkaar steeds minder, maar telkens als we weer bij elkaar zijn voelt het als vanouds. Ik hoop op nog vele avonden in cafes, op de tennisbaan of thuis bij iemand op de bank. Tot slot wil ik mijn familie bedanken. Een speciaal dankwoord ook aan tant Josine voor die keren dat ik bij jou kon overnachten in Eindhoven om de reis naar Amsterdam iets korter te maken of als de trein tussen Amsterdam en Limburg vertraagd was. Monique, Harry, pap en mam, ik ben ontzettend dankbaar voor jullie steun de afgelopen jaren. Ik voel me altijd welkom om terug te gaan naar mijn oude huis in Bocholtz. Toby, voor alle lieve knuffels die je mij altijd geeft sinds dat je een jaar geleden bij pap en mam bent ingetrokken. En als laatste Roel, je zal altijd mijn kleine broertje blijven en vooral mijn beste vriend. Dankjewel dat je er altijd voor mij bent.

To everyone who has been part of this amazing journey, thank you.